MASTER

Analytical and numerical framework for extensive electromagnetic analysis of tubular permanent magnet actuators

Gysen, B.L.J.

Award date:
2007

U/e technische universiteit eindhoven

/ faculteit elektrotechniek

TU/e technische universiteit eindhoven

Capaciteitsgroep Elektrische Energietechniek
Electromechanics & Power Electronics

Master of Science Thesis

Analytical and Numerical Framework for Extensive Electromagnetic Analysis of Tubular Permanent Magnet Actuators

B.L.J. Gysen
EPE.2007.A.15

Coaches:

dr. E.A. Lomonova
dr.ir. J.J.H. Paulides

August 23, 2007

Analytical and Numerical Framework for Extensive Electromagnetic Analysis of Tubular Permanent Magnet Actuators

Author: B.L.J. Gysen
Coaches: Dr. E.A. Lomonova
Dr. J.J.H. Paulides

23 August, 2007

Abstract

This thesis describes various extensive analytical and numerical modelling techniques, which can be used for determination of the magnetic field inside the air gap of a tubular permanent magnet (PM) actuator. From this magnetic field solution, the force profile and electro-motive force (EMF) waveforms can be predicted. These models offer the benefit of a fast computation time and therefore, they can be used as a coarse model in an optimisation algorithm.

Firstly, the semi-analytical framework is derived, based on Fourier theory, where the axial periodicity of the actuator is utilised. Therefore, the end effects, due to the finite length of the stator, cannot be included in this model. The slotted stator gives rise to a very complicated boundary value problem, and in order to solve this problem, a current sheet model is used, hence the slotting effect and its related cogging force are excluded. The Maxwell equations in terms of the magnetic vector potential are solved in the air gap of the tubular PM actuator. From these magnetic field equations, the force waveform is derived by means of the Maxwell Stress Tensor. This semi-analytical framework is extended for skewed topologies, which offer the benefit of reducing the apparent force ripples, albeit at a decrease of the mean force. Validation is performed with Finite Element Analysis (FEA).

Secondly, in order to model the apparent cogging force due to the stator slots, a Schwarz-Christoffel (SC) conformal mapping is applied. The SC conformal mapping technique offers the benefit of mapping a complicated boundary value problem to a very simple one, where the magnetic field solutions are given in the literature. Therefore, it is possible to calculate the magnetic field inside the air gap numerically for the given slotted structure. From this magnetic field solution it is possible to determine the cogging force due to the slotted stator, and the thrust force resulting from the stator currents. In all cases acceptable agreement has been found between the semi-analytical and numerical solutions and the FEA.

Publications

The various outcomes of this thesis have led to the following publications:

- B.L.J. Gysen, E.A. Lomonova, J.J.H. Paulides, A.J.A. Vandenput, "Analytical and numerical techniques for solving Poisson and Laplace equations in a tubular permanent magnet actuator, Part I. The Semi-Analytical Framework", *IEEE Transactions on Magnetics.*
- B.L.J. Gysen, E.A. Lomonova, J.J.H. Paulides, A.J.A. Vandenput, "Analytical and numerical techniques for solving Poisson and Laplace equations in a tubular permanent magnet actuator, Part II. Schwarz-Christoffel mapping", *IEEE Transactions on Magnetics.*

During the master phase, a traineeship at the University of Sheffield has led to another publication:

- B.L.J. Gysen, S. Gibson, R. Clark, G. Jewell, "High temperature permanent magnet actuator for fail-safe applications", *International Conference on Linear Drives and Actuators*, Lille, France, 2007.

Future PhD work

This work is a preparation for future PhD work in the IOP-EMVT II proposal Gauss-mount: a strut based on magnetism and control. The tubular permanent magnet actuator should replace conventional passive suspension systems which are based on a spring and a damper. A soft passive suspension can absorb the road vibrations giving high passenger comfort, however this results in a low manoeuvrability during cornering. Therefore, a passive suspension is always a trade-off between high passenger comfort and high manoeuvrability. An active suspension is capable of adjusting the spring and damper parameters, hence no compromise has to be made and relative high manoeuvrability and passenger comfort are achieved. Due to the tubular structure and its high force density, the tubular permanent magnet actuator is a possible candidate for replacing the conventional strut. In order to design such an actuator for low mass, low volume, high force and low force ripple, extensive modelling is needed to be able to predict the electromagnetic behaviour based on geometry and material parameters.

TABLE OF CONTENTS

Used symbols and abbreviations

Symbols

Quantity	Unit	Description
$\mathbf{A}$	Wb/m	Magnetic Vector Potential
A	m^2	Area
a	-	Coefficient
$\mathbf{B}$	T	Magnetic flux density
B_{rem}	T	Remanence magnetic flux density of the magnets
$\mathcal{B}_{\mathcal{J}}$	-	Ordinary Bessel function of the first kind
$\mathcal{B}_{\mathcal{Y}}$	-	Ordinary Bessel function of the second kind
$\mathcal{B}_{\mathcal{I}}$	-	Modified Bessel function of the first kind
$\mathcal{B}_{\mathcal{K}}$	-	Modified Bessel function of the second kind
b	-	Coefficient
C	-	Coefficient
c	-	Coefficient
$\mathbf{D}$	C/m^2	Electric flux density
d_x	m	Width of the Z-domain
d_y	m	Height of the Z-domain
$\mathbf{E}$	V/m=N/C	Electric field intensity
$\mathbf{e}$	-	Unit vector
e	V	Electro-motive force (EMF)
$\mathcal{F}$	A-turns	Magneto-motive force (MMF)
$\mathbf{F}$, F	N	Force
$\mathbf{f}$	N/m^3	Force density vector
f	Hz	Frequency
$f(z)$	-	SC-mapping function
g	m	Airgap length
$g(r)$	-	Tranformation function
g'	m	Equivalent airgap length
$\mathbf{H}$	A/m	Magnetic field intensity
H_c	A/m	Coercitive field intensity of the magnets
h	m	Height
I	A	Electric current
$\mathbf{J}$	A/m^2	Current density vector
J_s	A/m	Surface current density
j	-	Imaginary unity, $i = \sqrt{-1}$
$\mathcal{K}$	-	Function consisting of a Bessel integral
K_i	-	Fourier coefficient of the current excitation
K_w	-	Winding distribution
k	-	Integer coefficient
L	H	Inductance
L	m	Length
l	-	Lowerbound of an integral

Quantity	Unit	Description
$\mathbf{M}$	A/m	Magnetisation vector
M_{ij}	H	Mutual inductance between phases i and j
m_n	1/m	Spatial frequency of order n
N	-	Number of turns per slot
N_p	-	Number of pole pairs
N_s	-	Number of slots
N_{ph}	-	Number of phases
N_{sp}	-	Number of slots per phase
n	-	Harmonic number
$\mathbf{P}$	C/m^2	Polarisation vector
$\mathcal{P}$	Tm^2/A	Permeance
P	-	Polygon
p	-	Number of periods
Q	-	Coefficient
r	m	Radial position
$\mathcal{R}$	$A/(Tm^2)$	Reluctance
R	m	Radius
$\mathcal{S}$	m	Skewing transformation
S	m^2	Surface
$\mathbb{T}$	T^2	Maxwell Stress Tensor
T_{cn}, T_{sn}	-	Coefficient
u	m	Position in the u-direction
V	m^3	Volume
v	m/s	Velocity in axial direction
v	m	Position in the v-direction
w_i	m	Point in the W-domain
x	m	Position in the x-direction
y	m	Position in the y-direction
z	m	Axial position of the stator coordinate system
z'	m	Axial position in the translator coordinate system
z_i	m	Point in the Z-domain
α	rad	Angle
α_p	-	Magnet-to-pole pitch ratio
β	rad	Angle
Δ_s	m	Skewing amplitude
Δ_z	m	Relative position between the stator and translator
ϵ	F/m	Permittivity
ϵ_0	F/m	Permittivity of vacuum ($8.854{\cdot}10^{-12}$)
μ	Tm/A	Permeability
μ_0	Tm/A	Permeability of vacuum ($4\pi \cdot 10^{-7}$)
μ_r	-	Relative Permeability
Ψ	Wb	Flux linkage
ϕ	Wb	Flux

Subscripts

Subscript	Description
I	In region I
II	In region II
III	In region III
A	Phase A
ag	The center of the air gap
ax, z	Axial direction
B	Phase B
C	Phase C
n	Harmonic number
r	Radial direction
s	Surface
sk	Skewed
$unsk$	Unskewed
θ	Angular direction
$W - dom$	In the W-domain
$Z - dom$	In the Z-domain
$\perp$	Orthogonal direction

Acronyms

Acronym	Description
EMF	Electro-motive force
FE	Finite Element
FEA	Finite Element Analysis
FEM	Finite Element Method
MEC	Magnetic Equivalent Circuit
MMF	Magneto-motive force
RMS	Root Mean Square
SC	Schwarz-Christoffel
THD	Total Harmonic Distortion

Acknowledgements

This thesis concludes the final project for obtaining my Master of Science degree in Electrical Engineering. This work is established at the University of Technology Eindhoven in the Electromechanics and Power Electronics group of the faculty Electrical Engineering. First of all I want to thank Dr.M.Sc. Elena Lomonova for the direct coaching of my project and for the feedback on my work. Further I want to thank Dr. Johan Paulides for all the background information on tubular PM actuators and their applications.

Special thanks to Dr. A. van Deursen for the background on conformal mapping and practical implemention issues. Also special thanks to Prof.Dr.ir. Jan de Graaf for his mathematical explanation on the transformation of coordinate systems. Futhermore, thanks to ir. Jeroen Janssen for his previous work regarding the tubular permanent magnet actuator and finite element modelling, and to ir. Helm Jansen for the answers to general questions regarding electromagnetics and finite element modelling. Finally, I would like to thank everyone who was involved in my final project.

1. INTRODUCTION

The actuator under consideration is a tubular permanent magnet (PM) actuator. A tubular actuator can be regarded as a linear machine which is curled around the axis of movement. A linear machine in his turn can be derived from a rotary machine by cutting the rotor and unfolding it to a linear machine, as shown in Fig. 1.1. Commercially available motors are shown in Fig. 1.2.

These actuators have the advantage of a high force density in axial direction, which make them suitable for many industrial applications. Traditionally, these tasks where performed by hydraulic or pneumatic actuators, but the replacement of a tubular permanent magnet actuator can increase the reliablity, flexibility, ease of control and reduce weigth and volume. Many industrial applications arise which have benefit in replacing the current linear actuators by tubular PM actuators. The hydraulic and pneumatic actuators are very inefficient due to the required continously pressurised system. Also the response is very slow due to pressure losses and flexible hoses and the large mass due to the high number of parts make these systems very inefficient. A conventional linear PM actuator suffers from side effects, due to the finite depth, and end effects due to the finite length of the machine. In a tubular PM actuator however, these side effects are eliminated due to the tubular structure. Also the large attraction force which is existing in a linear PM actuator does not exist in a tubular PM actuator due to the axisymmetry.

In order to be able to design such an actuator with a given set of geometry and performance specifications, an extensive model is needed with a high accuracy and small computation time. Since both requirements are often in contradiction, various models are used in combination with an optimisation routine, e.g. the Space Mapping technique [12]. It is often a combination of a fast but less accurate model, the 'coarse model', together with a slow but relative accurate model, the 'fine' model, which, in general, is a finite element (FE) model. This thesis describes different analytical and numerical models which can be used as a coarse model for optimisation. In most cases the analytical model is preferred since it gives insight into the dependency of the various geometrical parameters and material properties on the performance of the actuator.

Many numerical and analytical methods are existing for analysis, design and optimisation of electrical machines, each with their own strength and pitfalls. Four models, which appear in the literature, are

- The Magnetic Equivalent Circuit (MEC),
- The (semi-) analytical framework,
- The Schwarz-Christoffel (SC) conformal mapping technique,
- The Finite Element Method (FEM).

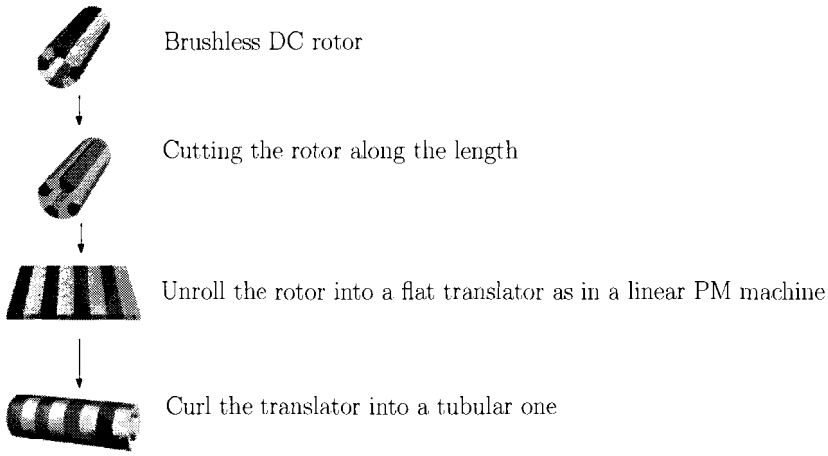

Fig. 1.1: From a rotary machine to a tubular one.

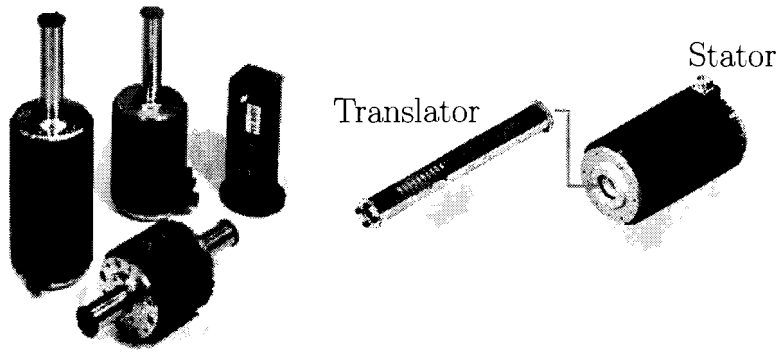

Fig. 1.2: Commercially available tubular motors.

The magnetic equivalent circuit (MEC) is widely used because of its simplicity and relative small computation time, see for example [5, 17, 18]. These equivalent circuits have the analogy of an electric circuit and are a simplification of the governing Maxwell equations

$$\nabla \times \mathbf{E} = -\frac{\partial \mathbf{B}}{\partial t} \quad \Leftrightarrow \quad u_k + e_k = R_k i_k, \tag{1.1}$$

$$\nabla \times \mathbf{H} = \mathbf{J} \quad \Leftrightarrow \quad F_k = \mathcal{R}_k(\Phi_k)\Phi_k. \tag{1.2}$$

In general, the simplification (1.1) in electrical networks is valid since the currents, i_k, are concentrated in wires and the voltages, u_k, e_k, are clearly defined. However, in a magnetic circuit the simplification (1.2) is not always valid since the flux, Φ_k, does not have predetermined paths due to the slot/tooth structure of the stator and/or translator. The MEC method therefore, needs preliminary knowledge about the flux paths for calculation of the different reluctances, $\mathcal{R}_k$, and the field distribution is only calculated at a few discrete points of the structure which makes the force calculation very inaccurate. Further, the reluctances are dependent on the amount of flux, due to the nonlinear ferromagnetic material, which makes the calculation an iterative process.

The most elegant method for determination of the electromagnetic fields is the analytical solution which provides the dependency of the geometry and the material properties on

the performance. Another advantage is the small computation time, which makes it suitable for a coarse model. The disadvantage of this method is that it only applies to the linear case (no saturation) and a lot of assumptions and simplifications on the geometry have to be made.

Schwarz-Christoffel conformal mapping is a technique which originates from the Riemann mapping theorem (1851) and it is becoming usefull nowadays due to the computational capabilities of microprocessors. It states that any simply connected region in the complex plane can be conformally mapped onto any other, provided that neither is the entire plane. This method can only handle geometries with a limited number of points but it is able to calculate the field solution numerically at every point within a closed polygon. This method cannot take saturation into account which limits its ability to the linear case. However the computational time is relatively shorter then the finite element method (FEM). This method is already applied for the various electrical machines with successive results, [13, 14, 15, 16, 19].

The Finite Element Method (FEM) can be regarded as the most accurate one, because it takes saturation into account and almost no simplification of the actual geometry is needed. However, it is still not possible to model hysteresis losses since only the initial BH-curve of the material is taken into account. The relatively long computation time makes it unusefull for design and optimisation and in most cases it will only be used as a fine model for verification.

This thesis describes the analytical framework and the SC conformal mapping technique for determination of the magnetic field inside the air gap of the tubular PM actuator. In Chapter 2, a description of the tubular PM actuator is given together with the FE model used for verification, furthermore the geometrical parameters and material properties are given which are used throughout this text. The semi-analytical framework for magneto-static analysis is given in Chapter 3, where the magnetic field due to the magnets and the stator currents will be derived seperately. The total field solution is calculated by superposition and used for electro-motive force (EMF), force and inductance calculation. The extension for skewed topologies will be derived in Chapter 4 based upon the semi-analytical framework of Chapter 3. Various skewing topologies will be considered and the influence on the EMF and force wavefroms will be shown. The cogging force related to the slotting effect will be calculated with the SC-mapping technique in Chapter 5. Finally conclusions will be drawn regarding the various derived models.

2. DESCRIPTION OF THE TUBULAR PERMANENT MAGNET ACTUATOR

In this section, the tubular PM actuator in Fig. 2.1 is described together with its function, the FE model and the relevant dimensions and the material properties. The actuator consists of two main parts, the magnets together with the inner tube is called the translator and the slots with the three phase winding is called the stator. In order to perform continouos linear motion, either the stator or the translator should be extended. This is preferably the translator otherwise, extra coils should be energised which do not contribute to the thrust force. In this thesis, only the interior magnet topology is considered, however the analysis can easily be applied to exterior magnet configurations using the same strategy. The stator slots and the translator iron are made of ferromagnetic material. Furthermore, N_p is the number of pole-pairs within the length of the stator, five in this case. The total number of slots is 15 and therefore, a slot/pole/phase number, N_{spp} of $1/2$ is considered. The stator consists of a three phase concentrated winding scheme, $N_{ph} = 3$ and the number of turns per coil is denoted as N. Note that numerous slot/pole/phase combinations and winding topologies are possible during analysis.

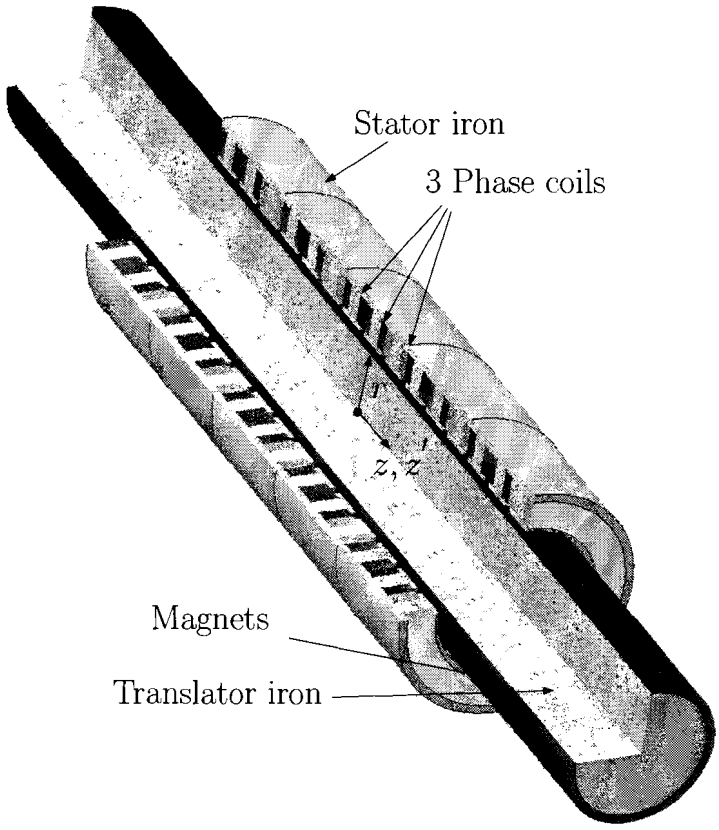

Fig. 2.1: The tubular permanent magnet actuator.

2.1 Coordinate systems

The stator is taken as a global reference frame, which means that the stator is fixed and the translator is moving. The actuator has total symmetry around the z-axis thus, it is convenient to use a cylindrical coordinate system, since the problem reduces to a two-dimensional one. Because the translator is moving independently, two coordinate systems have to be taken into account. The coordinate system of the stator has coordinates (r, z), where the origin for the radial direction is obviously in the center of the machine and the origin in axial direction is in the middle of the axial length of the stator, see Fig. 2.1. The coordinate system of the translator moves with respect to the stator in a coordinate system denoted as (r, z') where the origin for the radial direction is the same, since no excentricity is considered, and the origin in axial direction is in the middle of the axial length of the translator, see also Fig. 2.1. Only movement in axial direction is possible and therefore, the two coordinate systems differ only in axial direction, where the difference is defined as $\Delta_z = (z - z_0) - (z' - z'_0)$. For simplicity, take the offsets equal to zero, $z_0 = z'_0 = 0$, which gives $\Delta_z = z - z'$. The velocity of the translator is defined as $v(t) = \frac{d\Delta_z}{dt}$ and the force is calculated with respect to the translator.

2.2 Force components

The force of the actuator results from the magnetic field due to the magnets which interacts with the currents in the stator coils, the so called 'Lorentz force'. Also other force components result from the total field interferring with the slotted ferromagnetic structure of the stator. The latter is most of the times referred as the cogging force. This cogging force consists of two seperable parts, the first is by interaction of the magnetic field at the stator teeth tips, called the slotting effect, and the related cogging force is the slot cogging. The second is due to the interaction of the magnetic field at the ends of the stator, called the end effect, and the related cogging force is referred as the end cogging. During magnetostatic analysis, one can describe the magnetic field in terms of Fourier components for every spatial frequency existing in the periodical structure. The mean force results from interaction between spatial frequencies of the magnetic field of the magnets with the same frequencies of the stator currents, where the magnitude of the latter is determined by the amplitude of the current. If an ideal Halbach magnetised topology is considered, the magnetic field of the magnets has only a fundamental harmonic. Therefore, it is beneficial to use AC excitation with the same fundamental spatial frequency which results in a constant mean force, disregarding end and slotting effects. If however a radial magnetised topology with full pitch magnets is considered, then it is more beneficial to use DC excitation since also higher spatial frequencies contribute to the mean force. In order to obtain maximum mean force, the magnetic field of the magnets and the current excitation have to be in phase for every position, this is established with commutation, where the amplitude of the stator currents is dependent on the relative position between stator and translator, Δ_z. Next to the mean force, different spatial frequencies cause force ripples. For example the fifth harmonic of the magnetic field due to the magnets together with an AC excitation will result in a force ripple of the sixth harmonic. All combinations exist but keep in mind that a three phase system is considered and therefore a lot of higher harmonics cancel eachother. With AC excitation, this topology will have the mean force, and multiples of the least common multiple of the number of slots and the number of

poles within 360 electrical degrees. The topology considered in this thesis has 3 slots and 2 poles within 360 el.deg. and therefore, the force has ripples which are multiples of the sixth harmonic (6,12,18,...). If for example a slot/pole combination of 3/4 is considered, then the force will only have ripples of the twelfth harmonic and its multiples. If the same dimensions are considered, these ripples will be lower since the magnets must be smaller and therefore, the harmonics of the magnetic field of the magnets are lower, and as a result, also the mean force will be lower. Thus for example, a slot/pole combination of 3/4 will have a lower mean force then a slot/pole combination of 3/2, but also the force ripple will be lower.

The translator moves in axial direction with a total force, see Fig. 2.2, that consists of four components:

- Mean force due to the magnetic field due to the magnets and the current excitation of the same spatial frequencies,
- Force ripple due to the DC concentrated winding distribution and higher harmonics of the magnetic field due to the magnets, see Fig. 2.3,

and the total cogging force, see Fig. 2.4, which consists of

- Cogging force due to the finite length of stator and translator, see Fig. 2.5,
- Cogging force due to the slotted structure, see Fig. 2.6.

An undesirable effect of a slotted tubular PM actuator is the apparent cogging force due to the slotted structure and end effects. A way of eliminating the apparent force ripple, is by means of skewing of the stator or translator (or both), [10]. In Chapter 4, the analytical description of the skewed topology, disregarding end and slotting effects, is given. Nevertheless, minimisation of the force ripple due to the winding distribution and higher harmonics of the magnetic field due to the magnets, and minimisation of the total harmonic distortion (THD) on the electro-motive force (EMF) is established.

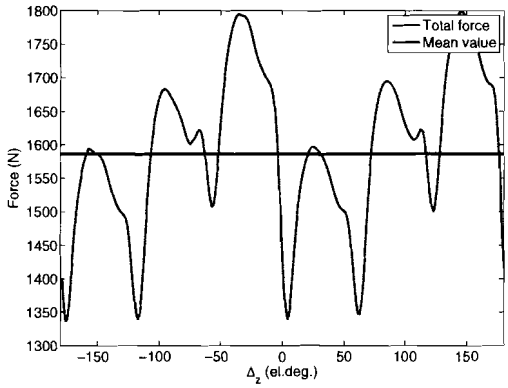

Fig. 2.2: The total force profile of the TPMA.

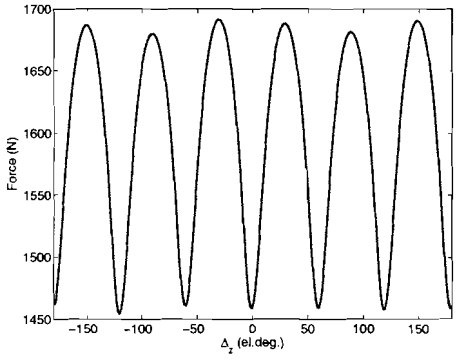

Fig. 2.3: The force due to the stator currents.

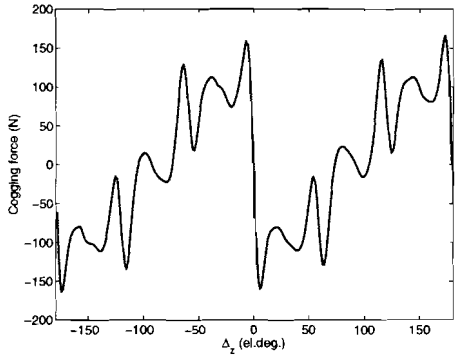

Fig. 2.4: The total cogging force.

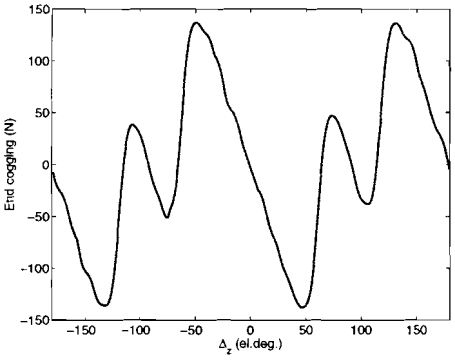

Fig. 2.5: The end cogging.

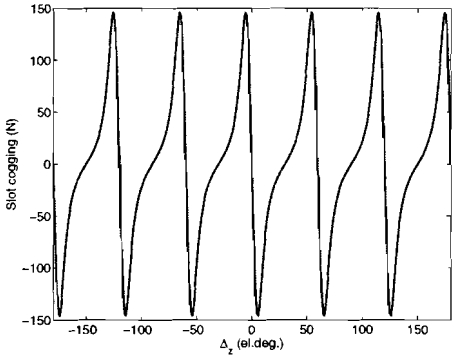

Fig. 2.6: The slot cogging.

2.3 Finite element modelling

The finite element model (FEM) is created with the software package FLUX 2D of Cedrat®, [20]. The axisymmetry is used and therefore, a two-dimensional model is made of the full actuator, see Fig. 2.8, where a zero flux boundary condition is applied to the axis of symmetry. The iron is modelled by the non-linear BH-curve, given in the next section. During analysis the magnetic field solutions of the analytical and numerical models are verified with the magnetic field solution of the FEM. However, in the analytical and numerical models only one pole-pair of the total actuator is considered, excluding end effects, and in order to compare this solution with the FEM, the magnetic field in the air gap at the center pole-pair of the FEM is compared with the solution of the analytical and numerical models. The reason for this is that in the center pole-pair of the machine, end effects have minimal influence on the magnetic field distribution in the air gap. Another option is to model only one pole-pair with periodical boundary conditions in the FEM, but the current version of the software does not allow for this type of modelling, but it will be shown that the use of only the center pole-pair gives acceptable agreement. When

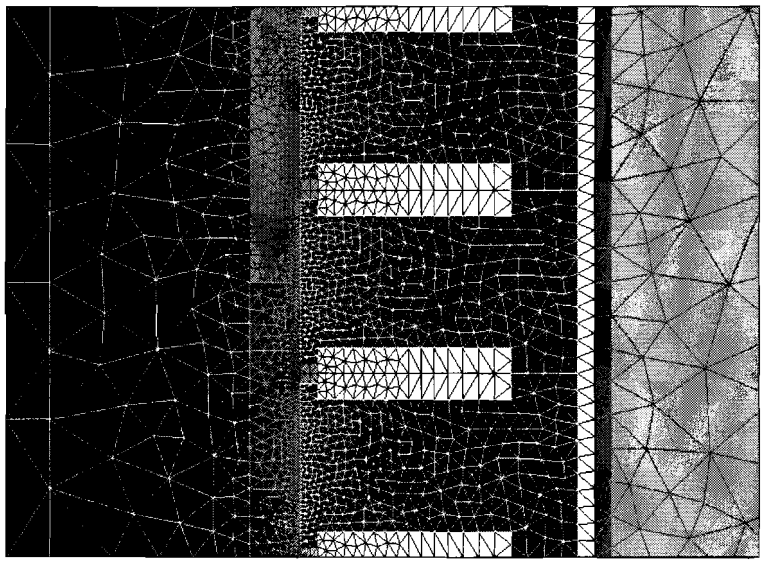

Fig. 2.7: The mesh of one pole-pair of the FE model of the tubular PM actuator.

the force is calculated with the FEM, all the previous mentioned force components are included, however the analytical and numerical models do not include all these components. In order to make a fair comparison of the accuracy of the solutions, the force calculated by the FEM is splitted into the various components. First a total force calculation is performed, which gives F_{tot}. Afterwards a simulation for zero current is performed, which gives the total cogging force including slotting and end effects, F_{cog}. Then the stator of the actuator is modelled as a full iron block and another simulation is performed resulting in the cogging force component due to the end effects, F_{end}. The cogging force due to the slotting effect is then obtained as $F_{slot} = F_{cog} - F_{end}$, and the netto force component without the cogging force is resulting from $F_{net} = F_{tot} - F_{cog}$. This superposition principle may only be applied if the actuator is not saturated and care must be taken using this approach. The mesh of the FEM is shown in Fig. 2.7 for one pole-pair.

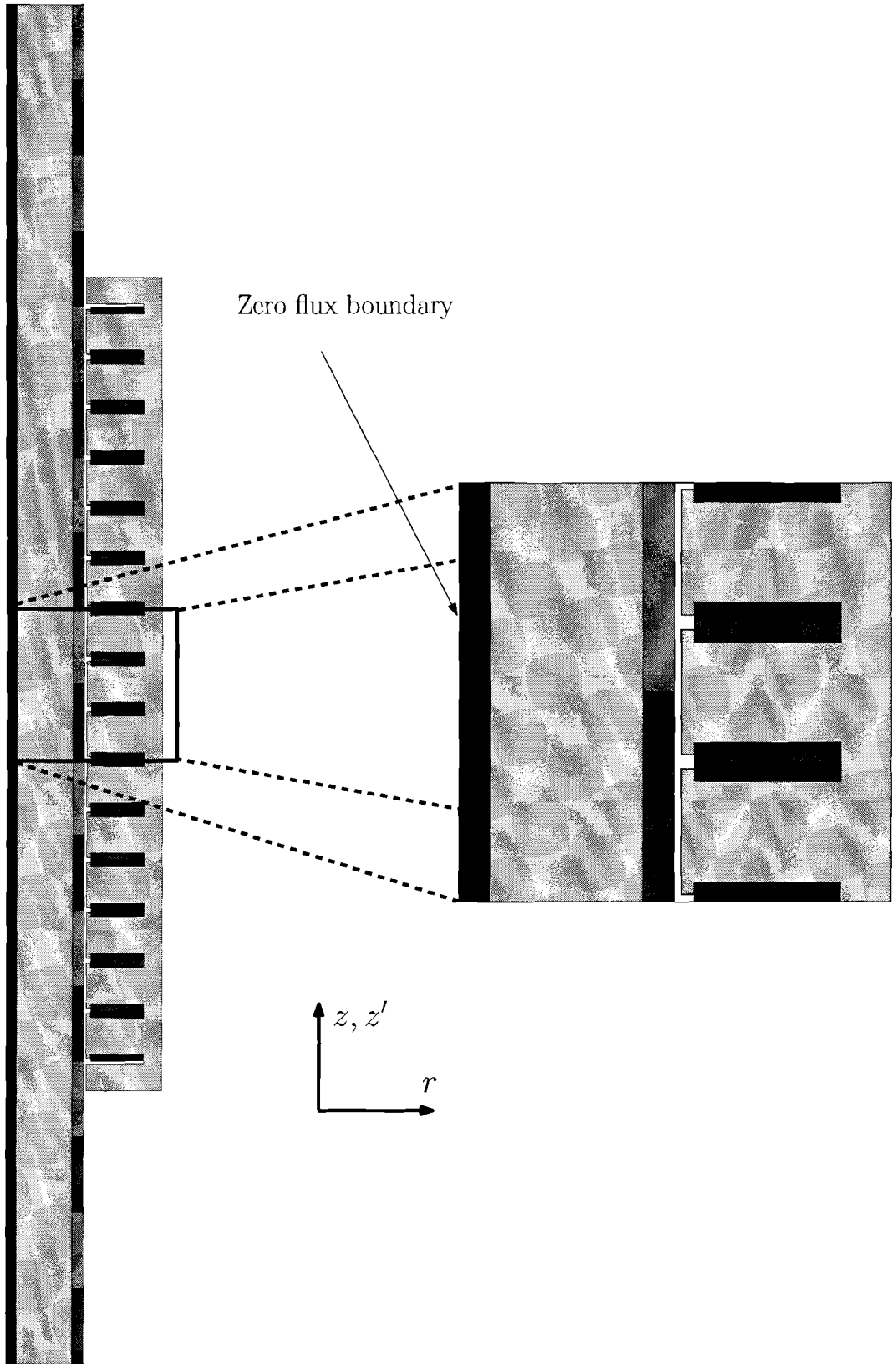

Fig. 2.8: Cross section of the total tubular PM actuator and a closer look to one pole-pair.

2.4 Dimensions and material properties

The ferromagnetic material of the stator slots and inner tube of the translator is chosen to be steel 1010 with a saturation flux density of 1.9 T and an initial relative permeability of 2063. The BH-curve is shown in Fig. 2.9. The magnet material is chosen to be

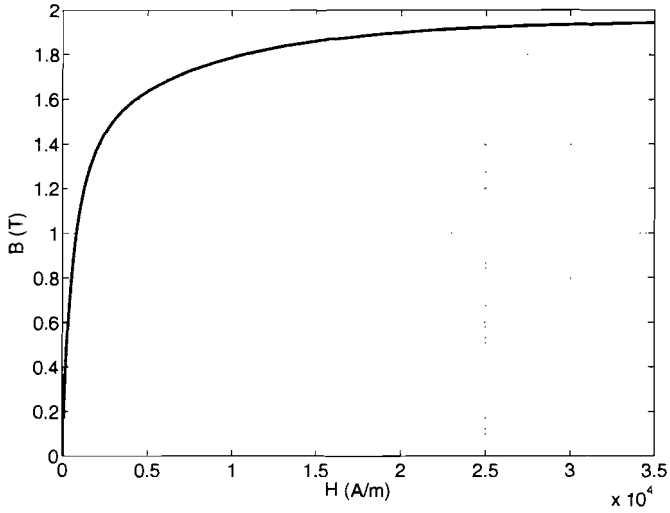

Fig. 2.9: The BH-curve of steel 1010.

neodymium iron boron, NdFeB30, with a remanent magnetic flux density, B_{rem}, of 1.23 T, a relative recoil permeability, μ_r, of 1.05 and a coercitive force, H_c, of 932 kA/m. The linear demagnetisation curve is shown in Fig. 2.10. The non-magnetic material of the

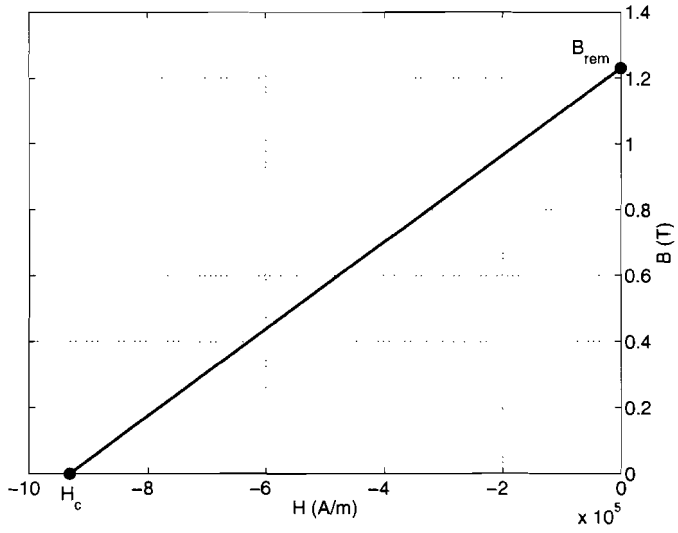

Fig. 2.10: The demagnetisation curve of NdFeB30.

inner tube can be air or aluminium, which has a relative permeablity of 1. The stator coils are made of copper where the relative permeability is equal to 1. In Fig. 2.11, one pole-pair of the tubular permanent magnet actuator is shown together with the various dimension parameters given in Table 2.1

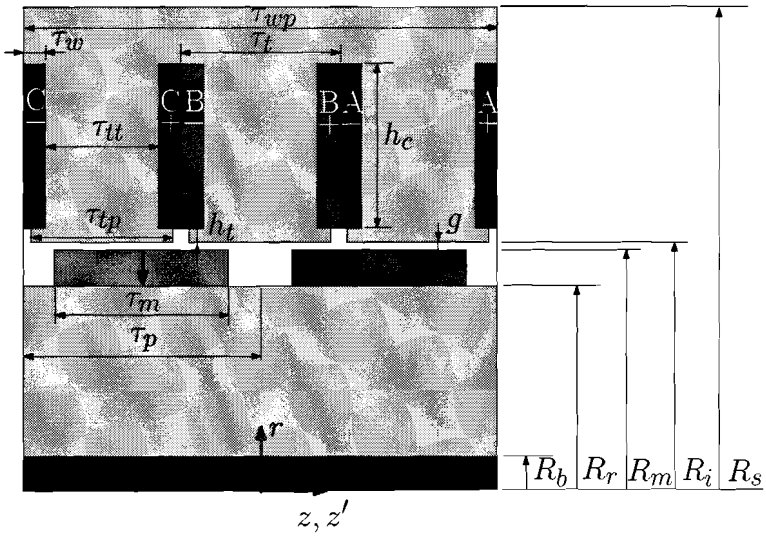

Fig. 2.11: One pole pair of the actuator with the relevant dimensions.

Tab. 2.1: The relevant dimensions of the tubular actuator with their nominal values.

Dimension	Nominal value [mm]	Description
h_{bi}	7.8 mm	Height of the back iron
h_c	22.5 mm	Height of the coils
h_m	5 mm	Height of the magnets
h_t	2 mm	Height of the teeth tips
g	1 mm	Airgap length
N	1	Number of windings
N_p	5	Number of pole-pairs facing the air gap
N_{ph}	3	Number of phases
N_s	15	Number of slots
N_{sp}	5	Number of slots per phase N_s/N_{ph}
R_{ag}	33.8 mm	Mean radius of the air gap
R_b	5 mm	Radius of the aluminium bar
R_i	34.3 mm	Inner radius of the stator
R_m	33.3 mm	Outer radius of the magnets
R_r	28.3 mm	Radius of the iron part of the rotor
R_s	66.6 mm	Outer radius of the stator
τ_m	32.3 mm	Magnet pitch
τ_p	32.3 mm	Pole pitch
τ_t	21.46 mm	Slot pitch
τ_{tt}	15.53 mm	Tooth width
τ_{tp}	19.1 mm	Width of the teeth tips
τ_w	3 mm	Width of the windings
τ_{wp}	64.6 mm	Winding pitch
τ_{ws}	1.12 mm	Width of the current sheets

3. MAGNETOSTATIC ANALYSIS OF THE UNSKEWED ACTUATOR

In this section the semi-analytical framework for the unskewed tubular PM actuator will be derived. The framework is mainly based on [8, 21, 22, 23, 24], but the description is more detailed and adapted to the tubular actuator described in the introduction. Everything is based on the periodicity of one pole-pair in axial direction and therefore, no end effects are included. Due to this periodicity, it is possible to use the Fourier theory in order to describe the magnetisation vector and the winding distribution in the tubular actuator. Using this theory, any random magnetisation topology or winding distribution can be regarded. In this Chapter, the radial magnetisation and the halbach magnetisation are considered, together with a three phase concentrated winding topology. One pole-pair of the tubular actuator is divided into radial regions with periodical boundary conditions on each side, as shown in Fig. 3.1. The magnetic field descriptions will then be considered for each region

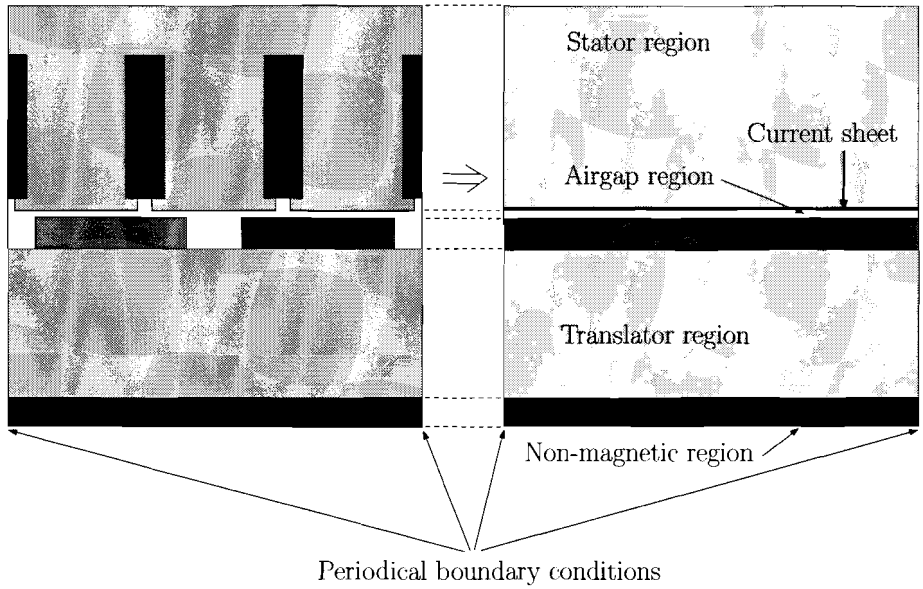

Fig. 3.1: Division in segments of one pole-pair of the tubular PM actuator.

seperately. This way of modelling has the advantage of having only boundaries in radial direction, which reduces the complexity significantly, since the complexity of the semi-analytical description increases with the number of boundary conditions that is considered. Because the stator is slotted, there are indeed axial boundary conditions inside the region of the stator. But for simplicity the stator is modelled as a full iron cilinder (no axial boundary conditions) with a current sheet distribution at the stator bore, R_i. Another assumption is that only linear steel with infinite relative permeability is considered, this assumption holds when the actuator will not be 'overloaded', so saturation will not occur and the initial relative permeability of the steel is high (in the order of 1000). Because

the FE modelling is performed with nonlinear steel, a verification off this assumption can be made. The reason why for this assumption is that the number of radial regions that have to be considered decreases, as will be discussed. All the assumptions are summarised below:

- Actuator consists of radial regions, tubes,
- Each region has axial periodical boundary conditions, end effects are excluded,
- Assuming linear steel with infinite permeability,
- Stator is modelled as a full iron tube, with a current sheet distribution at R_i, slotting effect is excluded.

Since the periodical boundary conditions at $z, z' = -\tau_p$ and $z, z' = \tau_p$ are applied, the magnetic field solution will consist of a Fourier description with spatial frequencies, denoted as m_n, of $\frac{n\pi}{\tau_p}$ for integer n. This holds for the magnetic field of the magnets and the stator currents. If for example a slot/pole combination of 3/4 is considered, then the spatial frequencies of the magnetic field are doubled, whereas the spatial frequencies of the magnetic field of the stator coils are kept the same.

Now, the field equations in terms of the magnetic vector potential for magnetostatic field analysis will be derived. Below, the general Maxwell equations are given in differential form, [6]

$$\nabla \times \mathbf{H} = \mathbf{J} + \frac{\partial \mathbf{D}}{\partial t}, \tag{3.1}$$

$$\nabla . \mathbf{B} = 0, \tag{3.2}$$

$$\nabla \times \mathbf{E} = -\frac{\partial \mathbf{B}}{\partial t}, \tag{3.3}$$

$$\nabla . \mathbf{D} = \rho, \tag{3.4}$$

where $\mathbf{E}$ is the electric field intensity, $\mathbf{D}$ the electric flux density, $\mathbf{H}$ the magnetic field intensity, $\mathbf{B}$ the magnetic flux density, $\mathbf{P}$ the polarisation vector, $\mathbf{M}$ the magnetisation vector, $\mathbf{J}$ the current density vector and ρ the free charge density. The consitutive relations are given by

$$\mathbf{B} = \mu_0(\mathbf{H} + \mathbf{M}), \tag{3.5}$$

$$\mathbf{D} = \epsilon_0 \mathbf{E} + \mathbf{P}, \tag{3.6}$$

and since only stationary, linear, homogeneous and isotropic media are considered, the consitutive relations reduce to

$$\mathbf{B} = \mu \mathbf{H}, \tag{3.7}$$

$$\mathbf{D} = \epsilon \mathbf{E}, \tag{3.8}$$

where μ and ϵ are the permeability and permittivity of the media, respectively. First, only the magnetostatic case is considered, this means that there is no time variation. Mathematically, this means that $\frac{\partial \mathbf{D}}{\partial t} = 0$ and $\frac{\partial \mathbf{B}}{\partial t} = 0$, and the Maxwell equations reduce

to

$$\nabla \times \mathbf{H} = \mathbf{J}, \tag{3.9}$$
$$\nabla.\mathbf{B} = 0, \tag{3.10}$$
$$\nabla \times \mathbf{E} = 0, \tag{3.11}$$
$$\nabla.\mathbf{D} = \rho. \tag{3.12}$$

The problem reduces from one set of four coupled differential equations to two sets of two coupled differential equations. Since the fields in the air gap of the actuator are mainly magnetostatic fields, only the first set of coupled differential equations is considered.

If the divergence of a given vector field is zero, which is the case for the magnetic flux density vector, $\mathbf{B}$, then this vector field can be written as the curl of another vector field, say $\mathbf{A}$

$$\nabla.\mathbf{B} = 0 \Rightarrow \mathbf{B} = \nabla \times \mathbf{A}, \tag{3.13}$$

where $\mathbf{A}$ is defined as the magnetic vector potential. A vector field is uniquely defined by its divergence and curl, therefore, in order to uniquely define the magnetic vector potential, its divergence needs to be defined and for simplicity it is set to zero

$$\nabla.\mathbf{A} = 0 \text{ (Coulomb gauge)}. \tag{3.14}$$

Using equation (3.14) and $\mathbf{B} = \nabla \times \mathbf{A}$ into the first magnetostatic Maxwell equation gives

$$\begin{aligned}
\nabla \times \mathbf{H} &= \mathbf{J}, \\
&\Downarrow \quad \mathbf{B} = \mu_0(\mathbf{H} + \mathbf{M}) \\
\nabla \times \mathbf{B} &= \mu_0(\mathbf{J} + \nabla \times \mathbf{M}), \\
&\Downarrow \quad \mathbf{B} = \nabla \times \mathbf{A} \\
\nabla \times \nabla \times \mathbf{A} &= \mu_0(\mathbf{J} + \nabla \times \mathbf{M}), \\
&\Downarrow \\
\nabla^2\mathbf{A} - \nabla(\nabla.\mathbf{A}) &= -\mu_0(\mathbf{J} + \nabla \times \mathbf{M}), \\
&\Downarrow \quad \text{(Coulomb gauge)} \\
\nabla^2\mathbf{A} &= -\mu_0(\mathbf{J} + \nabla \times \mathbf{M}),
\end{aligned} \tag{3.15}$$

and the total problem is reduced to one differential equation together with its boundary conditions. This type of differential equation, is known as 'Poissons equation', if however, a source free region is considered, where $\mathbf{J}$ and $\mathbf{M}$ are equal to zero, then Poissons equation reduces to a 'Laplace's equation' given by

$$\nabla^2\mathbf{A} = \mathbf{0}. \tag{3.16}$$

Due to the axisymmetry, there is no magnetic flux density in the angular direction, $B_\theta = 0$ and the radial and axial component are independent of θ

$$\mathbf{B} = B_r(r, z)\mathbf{e}_r + B_z(r, z)\mathbf{e}_z \tag{3.17}$$

Due to the relation $\mathbf{B} = \nabla \times \mathbf{A}$, the magnetic vector potential has only a component in the angular direction which is independent of θ. Thus the magnetic vector potential can be described as

$$\mathbf{A} = A_\theta(r, z)\mathbf{e}_\theta \tag{3.18}$$

Now, the left hand side of equation (3.15) or (3.16) can be written as

$$\nabla^2 \mathbf{A} = \left(\frac{\partial^2 A_\theta}{\partial r^2} + \frac{1}{r}\frac{\partial A_\theta}{\partial r} - \frac{2}{r^2} A_\theta + \frac{\partial^2 A_\theta}{\partial z^2} \right) \mathbf{e}_\theta. \tag{3.19}$$

This differential equation will be solved for the regions of interest and the magnetic flux density is derived from the magnetic vector potential. There are two field sources in the actuator, the magnets and the coils. First, the flux density due to the magnets will be derived for both radial and halbach magnetised slotted topologies. From that point on, only a radial magnetised topology is considered. Next, the electro-motive force (EMF) is calculated. Afterwards, the magnetic field of the stator currents is calculated for a given winding distribution. Superposition is applied in order to calculate the total field in the air gap and the magnets. The thrust force will be calculated based upon previous magnetic field calculations by means of the Maxwell stress tensor. Finally, the self and mutual inductances will be calculated.

3.1 Magnetic field of the magnets

In Fig. 3.2, the radial regions of the actuator are shown for calculation of the magnetic field distribution of the magnets. The non-magnetic region can be disregarded, because the field sources, the magnets, are positioned between two regions with infinite permeability, therefore, the non-magnetic region is isolated from any magnetic behaviour. With this assumption, only the airgap and the magnet region have to be considered, where the magnets can be either radial or halbach magnetised. The magnetic field equations in terms of the magnetic vector potential for region I and II are given by

$$\nabla^2 \mathbf{A}_{\mathrm{I}} = \mathbf{0}, \tag{3.20}$$

$$\nabla^2 \mathbf{A}_{\mathrm{II}} = -\mu_0 \nabla \times \mathbf{M}. \tag{3.21}$$

In the next sections, these field equations are solved for the radial and halbach magnetised topology.

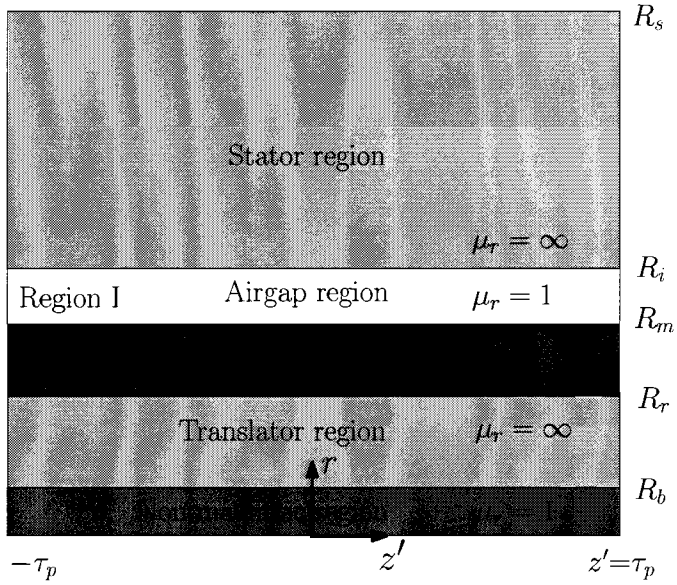

Fig. 3.2: Radial regions of one pole-pair of the TPMA for calculation of the magnetic field of the magnets.

3.1.1 Radial magnetised topology

In this section the radial magnetised topology is considered, the magnets are alternatively magnetised in positive and negative radial direction. Therefore, the discription of the magnetisation vector, $\mathbf{M}$, is done by means of the Fourier series of a square wave

$$\mathbf{M} = M_r \mathbf{e}_r = \sum_{n=1}^{\infty} M_n \sin(m_n z') \mathbf{e}_r,$$

$$M_n = \frac{2B_{rem}}{\mu_0} \frac{1-\cos(n\pi)}{n\pi} \cos\left(\frac{n\pi(1-\alpha_p)}{2}\right), \tag{3.22}$$

where $m_n = \frac{n\pi}{\tau_p}$ are the spatial frequencies, τ_p is the pole pitch, α_p is the magnet to pole pitch ratio $\frac{\tau_m}{\tau_p}$ and $\mathbf{e}_r$ is the unit vector in radial direction. In the FE model, only full pitch magnets are considered, and therefore evaluation of the magnetic field is performed with α_p equal to unity. Note that M_r is zero for even n. This gives for the right hand side of equation (3.21)

$$\begin{aligned} -\mu_0 \nabla \times \mathbf{M} &= -\mu_0 \frac{\delta M_r}{\delta z'} \mathbf{e}_\theta \\ &= -\sum_{n=1}^{\infty} \frac{2B_{rem}}{\tau_p}\big(1-\cos(n\pi)\big)\cos\left(\frac{n\pi(1-\alpha_p)}{2}\right)\cos(m_n z')\mathbf{e}_\theta \\ &= -\mu_0 \sum_{n=1}^{\infty} m_n M_n \cos(m_n z')\mathbf{e}_\theta. \end{aligned} \tag{3.23}$$

The flux density as function of the vector potential is given by $\mathbf{B} = \nabla \times \mathbf{A}$ and can be written as

$$\mathbf{B} = B_r(r,z')\mathbf{e}_r + B_{z'}(r,z')\mathbf{e}_{z'} \tag{3.24}$$

$$B_r = -\frac{\delta A_\theta}{\delta z'}, \tag{3.25}$$

$$B_{z'} = \frac{\delta}{r\delta r}(rA_\theta), \tag{3.26}$$

where $\mathbf{e}_{z'}$ is the unit vector in the axial direction. The Poisson (3.20) and Laplace (3.21) equations can be written as

$$\begin{aligned} \nabla^2 \mathbf{A}_{\mathrm{I}_\theta} &= \left(\frac{\partial^2 A_{\mathrm{I}_\theta}}{\partial r^2} + \frac{1}{r}\frac{\partial A_{\mathrm{I}_\theta}}{\partial r} - \frac{2}{r^2}A_{\mathrm{I}_\theta} + \frac{\partial^2 A_{\mathrm{I}_\theta}}{\partial z^2}\right)\mathbf{e}_\theta \\ &= \left(-\frac{\delta}{\delta z'}B_{\mathrm{I}_r} + \frac{\delta}{\delta r}B_{\mathrm{I}_{z'}}\right)\mathbf{e}_\theta = \mathbf{0}, \end{aligned} \tag{3.27}$$

$$\begin{aligned} \nabla^2 \mathbf{A}_{\mathrm{II}_\theta} &= \left(\frac{\partial^2 A_{\mathrm{II}_\theta}}{\partial r^2} + \frac{1}{r}\frac{\partial A_{\mathrm{II}_\theta}}{\partial r} - \frac{2}{r^2}A_{\mathrm{II}_\theta} + \frac{\partial^2 A_{\mathrm{II}_\theta}}{\partial z^2}\right)\mathbf{e}_\theta \\ &= \left(-\frac{\delta}{\delta z'}B_{\mathrm{II}_r} + \frac{\delta}{\delta r}B_{\mathrm{II}_{z'}}\right)\mathbf{e}_\theta = -\mu_0 \sum_{n=1}^{\infty} m_n M_n \cos(m_n z')\mathbf{e}_\theta. \end{aligned} \tag{3.28}$$

These differential equations are solved by the method of seperation of variables, where the summation can be disregarded since the differential equations should hold for every n. The solution is a Bessel distribution in radial direction and a sinusoidal distribution in axial direction, given by

$$A_{\mathrm{I}_\theta} = -\sum_{n=1}^{\infty} \frac{1}{m_n}\Big(a_{1n}\mathcal{B}_{\mathcal{I}1}(m_n r) + b_{1n}\mathcal{B}_{\mathcal{K}1}(m_n r)\Big)\cos(m_n z'), \tag{3.29}$$

$$\begin{aligned} A_{\mathrm{II}_\theta} = -\sum_{n=1}^{\infty} \frac{1}{m_n}\Big\{&\Big(\mathcal{K}_{an}(m_n r) + a_{2n}\Big)\mathcal{B}_{\mathcal{I}1}(m_n r) \\ &- \Big(\mathcal{K}_{bn}(m_n r) - b_{2n}\Big)\mathcal{B}_{\mathcal{K}1}(m_n r)\Big\}\cos(m_n z'). \end{aligned} \tag{3.30}$$

where a_{1n}, a_{2n}, b_{1n} and b_{2n}, are constants resulting from the boundary conditions, $\mathcal{B}_{\mathcal{I}o}$ and $\mathcal{B}_{\mathcal{K}o}$ are modified Bessel functions of the first and second kind respectively with order o (see Appendix A.1) and $\mathcal{K}_{an}(m_n r)$, $\mathcal{K}_{bn}(m_n r)$ are functions which result from substitution of (3.30) into (3.15). This gives the following solutions for B_{I_r}, $B_{\mathrm{I}_{z'}}$, B_{II_r} and $B_{\mathrm{II}_{z'}}$

$$B_{\mathrm{I}_r}(r,z') = -\sum_{n=1}^{\infty}\Big(a_{1n}\mathcal{B}_{\mathcal{I}1}(m_n r) + b_{1n}\mathcal{B}_{\mathcal{K}1}(m_n r)\Big)\sin(m_n z'), \tag{3.31}$$

$$B_{\mathrm{I}_{z'}}(r,z') = -\sum_{n=1}^{\infty}\Big(a_{1n}\mathcal{B}_{\mathcal{I}0}(m_n r) - b_{1n}\mathcal{B}_{\mathcal{K}0}(m_n r)\Big)\cos(m_n z'), \tag{3.32}$$

$$\begin{aligned} B_{\mathrm{II}_r}(r,z') = -\sum_{n=1}^{\infty}\Big\{&\Big(\mathcal{K}_{an}(m_n r) + a_{2n}\Big)\mathcal{B}_{\mathcal{I}1}(m_n r) \\ &- \Big(\mathcal{K}_{bn}(m_n r) - b_{2n}\Big)\mathcal{B}_{\mathcal{K}1}(m_n r)\Big\}\sin(m_n z'), \end{aligned} \tag{3.33}$$

$$\begin{aligned} B_{\mathrm{II}_{z'}}(r,z') = -\sum_{n=1}^{\infty}\Big\{&\Big(\mathcal{K}_{an}(m_n r) + a_{2n}\Big)\mathcal{B}_{\mathcal{I}0}(m_n r) \\ &+ \Big(\mathcal{K}_{bn}(m_n r) - b_{2n}\Big)\mathcal{B}_{\mathcal{K}0}(m_n r)\Big\}\cos(m_n z'), \end{aligned} \tag{3.34}$$

Derivation of the functions $\mathcal{K}_{an}(m_n r)$ and $\mathcal{K}_{bn}(m_n r)$ is done by substitution of (3.30) into (3.15), using (6.10) and (6.11), which gives

$$\begin{aligned} m_n\Big\{&\Big(\mathcal{K}_{an}(m_n r) + a_{2n}\Big)\mathcal{B}_{\mathcal{I}1}(m_n r) - \Big(+\mathcal{K}_{bn}(m_n r) - b_{2n}\Big)\mathcal{B}_{\mathcal{K}1}(m_n r)\Big\}\cos(m_n z') \\ &-\Big\{m_n\Big(\mathcal{K}_{an} + a_{2n}\Big)\mathcal{B}_{\mathcal{I}1}(m_n r) + m_n\Big(-\mathcal{K}_{bn}(m_n r) + b_{2n}\Big)\mathcal{B}_{\mathcal{K}1}(m_n r) \\ &+\frac{\delta\mathcal{K}_{an}(m_n r)}{\delta r}\mathcal{B}_{\mathcal{I}0}(m_n r) + \frac{\delta\mathcal{K}_{bn}(m_n r)}{\delta r}\mathcal{B}_{\mathcal{K}0}(m_n r)\Big\}\cos(m_n z') = -\mu_0 m_n M_n\cos(m_n z'), \end{aligned} \tag{3.35}$$

which simplifies to

$$\frac{\delta\mathcal{K}_{an}(m_n r)}{\delta r}\mathcal{B}_{\mathcal{I}0}(m_n r) + \frac{\delta\mathcal{K}_{bn}(m_n r)}{\delta r}\mathcal{B}_{\mathcal{K}0}(m_n r) = \mu_0 m_n M_n. \tag{3.36}$$

Now define

$$\mathcal{K}_{an}(m_n r) = \mu_0 M_n\int_{l_1}^{m_n r}\frac{\mathcal{B}_{\mathcal{K}1}(x)dx}{\mathcal{B}_{\mathcal{I}1}(x)\mathcal{B}_{\mathcal{K}0}(x) + \mathcal{B}_{\mathcal{K}1}(x)\mathcal{B}_{\mathcal{I}0}(x)}, \tag{3.37}$$

$$\mathcal{K}_{bn}(m_n r) = \mu_0 M_n\int_{l_2}^{m_n r}\frac{\mathcal{B}_{\mathcal{I}1}(x)dx}{\mathcal{B}_{\mathcal{I}1}(x)\mathcal{B}_{\mathcal{K}0}(x) + \mathcal{B}_{\mathcal{K}1}(x)\mathcal{B}_{\mathcal{I}0}(x)}, \tag{3.38}$$

for some lowerbounds l_1 and l_2 which will be defined later. Consider the following, for

random functions F and G

$$G(m_n r) = \int_{l_1}^{m_n r} F(x)dx = \int_0^{m_n r} F(x)dx - \int_0^{l_1} F(x)dx, \tag{3.39}$$

$$\Downarrow$$

$$\frac{\partial G(m_n r)}{\partial r} = \frac{\partial}{\partial r}\left(\int_0^{m_n r} F(x)dx - \int_0^{l_1} F(x)dx\right) = m_n F(m_n r). \tag{3.40}$$

If we substitute (3.37) and (3.38) into (3.36) and use property (3.40) we get

$$m_n\mu_0 M_n \frac{\mathcal{B}_{\mathcal{K}1}(m_n r)}{\mathcal{B}_{\mathcal{I}1}(m_n r)\mathcal{B}_{\mathcal{K}0}(m_n r) + \mathcal{B}_{\mathcal{K}1}(m_n r)\mathcal{B}_{\mathcal{I}0}(m_n r)}\mathcal{B}_{\mathcal{I}0}(m_n r)$$
$$+ m_n\mu_0 M_n \frac{\mathcal{B}_{\mathcal{I}1}(m_n r)}{\mathcal{B}_{\mathcal{I}1}(m_n r)\mathcal{B}_{\mathcal{K}0}(m_n r) + \mathcal{B}_{\mathcal{K}1}(m_n r)\mathcal{B}_{\mathcal{I}0}(m_n r)}\mathcal{B}_{\mathcal{K}0}(m_n r) = \mu_0 m_n M_n, \tag{3.41}$$

which is true, thus the proposed definitions of $\mathcal{K}_{an}(m_n r)$ and $\mathcal{K}_{bn}(m_n r)$ are correct. Note that the lowerbounds l_1 and l_2 used in $\mathcal{K}_{an}(m_n r)$ and $\mathcal{K}_{bn}(m_n r)$ can have any random constant value.

Now the constants a_{1n}, a_{2n}, b_{1n} and b_{2n} have to be derived with the given boundary conditions. Because there are four unknowns, four independent boundary conditions are needed. These boundary conditions are given by

$$B_{\mathrm{I}_{z'}}|_{r=R_i} = 0, \tag{3.42}$$
$$B_{\mathrm{II}_{z'}}|_{r=R_r} = 0, \tag{3.43}$$
$$B_{\mathrm{I}_r}|_{r=R_m} = B_{\mathrm{II}_r}|_{r=R_m}, \tag{3.44}$$
$$H_{\mathrm{I}_{z'}}|_{r=R_m} = H_{\mathrm{II}_{z'}}|_{r=R_m}. \tag{3.45}$$

The boundary conditions must hold for every harmonic and for all z', therefore the summation can be eliminated but keep in mind that the equations must hold for every n.

- The first boundary condition (3.42) gives

$$B_{\mathrm{I}_{z'}}(R_i, z') = -\Big(a_{1n}\mathcal{B}_{\mathcal{I}0}(m_n R_i) - b_{1n}\mathcal{B}_{\mathcal{K}0}(m_n R_i)\Big)\cos(m_n z') = 0,$$
$$\Downarrow$$
$$a_{1n}\mathcal{B}_{\mathcal{I}0}(m_n R_i) = b_{1n}\mathcal{B}_{\mathcal{K}0}(m_n R_i),$$

which for $\mathcal{B}_{\mathcal{I}0}(m_n R_i) = c_{1n}$ and $\mathcal{B}_{\mathcal{K}0}(m_n R_i) = c_{2n}$ reduces to:

$$a_{1n}c_{1n} = b_{1n}c_{2n},$$
$$\Downarrow$$
$$b_{1n} = \frac{c_{1n}}{c_{2n}}a_{1n}. \tag{3.46}$$

- The second boundary condition (3.43) gives

$$B_{\mathrm{II}_{z'}}(R_r, z') = -\Big\{\Big(\mathcal{K}_{an}(m_n R_r) + a_{2n}\Big)\mathcal{B}_{\mathcal{I}0}(m_n R_r) + \Big(\mathcal{K}_{bn}(m_n R_r) - b_{2n}\Big)\mathcal{B}_{\mathcal{K}0}(m_n R_r)\Big\}\cos(m_n z') = 0,$$

$$\Downarrow$$

$$\Big(\mathcal{K}_{an}(m_n R_r) + a_{2n}\Big)\mathcal{B}_{\mathcal{I}0}(m_n R_r) = -\Big(\mathcal{K}_{bn}(m_n R_r) - b_{2n}\Big)\mathcal{B}_{\mathcal{K}0}(m_n R_r),$$

which for $\mathcal{B}_{\mathcal{I}0}(m_n R_r) = c_{3n}$ and $\mathcal{B}_{\mathcal{K}0}(m_n R_r) = c_{4n}$ reduces to:

$$\Big(\mathcal{K}_{an}(m_n R_r) + a_{2n}\Big)c_{3n} = -\Big(\mathcal{K}_{bn}(m_n R_r) - b_{2n}\Big)c_{4n}. \tag{3.47}$$

Because the lowerbounds l_1 and l_2 can be chosen randomly, this expression can be simplified by taking $l_1 = l_2 = m_n R_r$ which results in $\mathcal{K}_{an}(m_n R_r) = 0$ and $\mathcal{K}_{bn}(m_n R_r) = 0$ and simplifies (3.47) to

$$b_{2n} = \frac{c_{3n}}{c_{4n}} a_{2n}. \tag{3.48}$$

- The third boundary condition (3.44) gives

$$B_{\mathrm{I}_r}(R_m, z') = B_{\mathrm{II}_r}(R_m, z'),$$

$$\Downarrow$$

$$-\Big(a_{1n}\mathcal{B}_{\mathcal{I}1}(m_n R_m) + b_{1n}\mathcal{B}_{\mathcal{K}1}(m_n R_m)\Big)\sin(m_n z')$$

$$= -\Big\{\Big(\mathcal{K}_{an}(m_n R_m) + a_{2n}\Big)\mathcal{B}_{\mathcal{I}1}(m_n R_m) - \Big(\mathcal{K}_{bn}(m_n R_m) - b_{2n}\Big)\mathcal{B}_{\mathcal{K}1}(m_n R_m)\Big\}\sin(m_n z'),$$

which for $\mathcal{B}_{\mathcal{I}1}(m_n R_m) = c_{7n}$ and $\mathcal{B}_{\mathcal{K}1}(m_n R_m) = c_{8n}$ together with (3.46) and (3.48) reduces to:

$$a_{1n}c_{7n} + b_{1n}c_{8n} = \Big(\mathcal{K}_{an}(m_n R_m) + a_{2n}\Big)c_{7n} + \Big(-\mathcal{K}_{bn}(m_n R_m) + b_{2n}\Big)c_{8n},$$

$$\Downarrow$$

$$\Big(\frac{c_{7n}}{c_{8n}} + \frac{c_{1n}}{c_{2n}}\Big)a_{1n} - \Big(\frac{c_{7n}}{c_{8n}} + \frac{c_{3n}}{c_{4n}}\Big)a_{2n} = \mathcal{K}_{an}(m_n R_m)\frac{c_{7n}}{c_{8n}} - \mathcal{K}_{bn}(m_n R_m). \tag{3.49}$$

• The fourth boundary condition (2.25) gives

$$\begin{aligned} H_{\mathrm{I}_{z'}}(R_m, z') &= H_{\mathrm{II}_{z'}}(R_m, z') \\ &\Downarrow \\ \frac{1}{\mu_0} B_{\mathrm{I}_{z'}}(R_m, z') &= \frac{1}{\mu_0 \mu_r} B_{\mathrm{II}_{z'}}(R_m, z') - \frac{1}{\mu_r} M_{z'}(R_m, z') \\ &\Downarrow \\ \mu_r B_{\mathrm{I}_{z'}}(R_m, z') &= B_{\mathrm{II}_{z'}}(R_m, z') \\ &\Downarrow \end{aligned}$$

$$\begin{aligned} &- \mu_r \Big(a_{1n} \mathcal{B}_{\mathcal{I}0}(m_n R_m) - b_{1n} \mathcal{B}_{\mathcal{K}0}(m_n R_m) \Big) \cos(m_n z') \\ &= - \Big\{ \Big(\mathcal{K}_{an}(m_n R_m) + a_{2n} \Big) \mathcal{B}_{\mathcal{I}0}(m_n R_m) + \Big(\mathcal{K}_{bn}(m_n R_m) - b_{2n} \Big) \mathcal{B}_{\mathcal{K}0}(m_n R_m) \Big\} \cos(m_n z') \end{aligned}$$

which for $\mathcal{B}_{\mathcal{I}0}(m_n R_m) = c_{5n}$ and $\mathcal{B}_{\mathcal{K}0}(m_n R_m) = c_{6n}$ together with (3.46) and (3.48) reduces to

$$\mu_r (a_{1n} c_{5n} - b_{1n} c_{6n}) = \Big(\mathcal{K}_{an}(m_n R_m) + a_{2n} \Big) c_{5n} + \Big(\mathcal{K}_{bn}(m_n R_m) - b_{2n} \Big) c_{6n}$$

$$\Downarrow$$

$$\mu_r \left(\frac{c_{5n}}{c_{6n}} - \frac{c_{1n}}{c_{2n}} \right) a_{1n} - \left(\frac{c_{5n}}{c_{6n}} - \frac{c_{3n}}{c_{4n}} \right) a_{2n} = \mathcal{K}_{an}(m_n R_m) \frac{c_{5n}}{c_{6n}} + \mathcal{K}_{bn}(m_n R_m). \quad (3.50)$$

In summary:

$$\begin{aligned} c_{1n} &= \mathcal{B}_{\mathcal{I}0}(m_n R_i), & c_{2n} &= \mathcal{B}_{\mathcal{K}0}(m_n R_i), \\ c_{3n} &= \mathcal{B}_{\mathcal{I}0}(m_n R_r), & c_{4n} &= \mathcal{B}_{\mathcal{K}0}(m_n R_r), \\ c_{5n} &= \mathcal{B}_{\mathcal{I}0}(m_n R_m), & c_{6n} &= \mathcal{B}_{\mathcal{K}0}(m_n R_m), \\ c_{7n} &= \mathcal{B}_{\mathcal{I}1}(m_n R_m), & c_{8n} &= \mathcal{B}_{\mathcal{K}1}(m_n R_m), \end{aligned} \quad (3.51)$$

$$\mathcal{K}_{an}(m_n r) = \mu_0 M_n \int_{m_n R_r}^{m_n r} \frac{\mathcal{B}_{\mathcal{K}1}(x) dx}{\mathcal{B}_{\mathcal{I}1}(x) \mathcal{B}_{\mathcal{K}0}(x) + \mathcal{B}_{\mathcal{K}1}(x) \mathcal{B}_{\mathcal{I}0}(x)}, \quad (3.52)$$

$$\mathcal{K}_{bn}(m_n r) = \mu_0 M_n \int_{m_n R_r}^{m_n r} \frac{\mathcal{B}_{\mathcal{I}1}(x) dx}{\mathcal{B}_{\mathcal{I}1}(x) \mathcal{B}_{\mathcal{K}0}(x) + \mathcal{B}_{\mathcal{K}1}(x) \mathcal{B}_{\mathcal{I}0}(x)}, \quad (3.53)$$

and a_{1n}, a_{2n}, b_{1n} and b_{2n} can be solved from the set of four linear equations, (3.46), (3.48),

(3.49) and (3.50)

$$a_{1n} = \frac{\left(\frac{c_{5n}}{c_{6n}} + \frac{c_{7n}}{c_{8n}}\right)\left(\frac{c_{3n}}{c_{4n}}\mathcal{K}_{an}(m_n R_m) + \mathcal{K}_{bn}(m_n R_m)\right)}{\left(\frac{c_{3n}}{c_{4n}} - \frac{c_{5n}}{c_{6n}}\right)\left(\frac{c_{1n}}{c_{2n}} + \frac{c_{7n}}{c_{8n}}\right) + \mu_r\left(\frac{c_{3n}}{c_{4n}} + \frac{c_{7n}}{c_{8n}}\right)\left(\frac{c_{5n}}{c_{6n}} - \frac{c_{1n}}{c_{2n}}\right)}, \tag{3.54}$$

$$a_{2n} = \frac{\left(\frac{c_{5n}}{c_{6n}}\mathcal{K}_{an}(m_n R_m) + \mathcal{K}_{bn}(m_n R_m)\right) - \mu_r\left(\frac{c_{5n}}{c_{6n}} - \frac{c_{1n}}{c_{2n}}\right)a_{1n}}{\left(\frac{c_{3n}}{c_{4n}} - \frac{c_{5n}}{c_{6n}}\right)}, \tag{3.55}$$

$$b_{1n} = \frac{c_{1n}}{c_{2n}}a_{1n}, \tag{3.56}$$

$$b_{2n} = \frac{c_{3n}}{c_{4n}}a_{2n}. \tag{3.57}$$

These equations are implemented in MATLAB® and the magnetic fields are calculated for n upto 50. The integrals of (3.52) and (3.53) are calculated numerically. The magnet-to-pole pitch ratio α_p is equal to 1. A Finite Element (FE) calculation is performed to verify the semi-analytical model. In Fig. 3.3 the flux density in the center of the air gap, $R_{ag} = \frac{R_i + R_m}{2}$, is plotted for $\Delta_z = 0$, resulting from the semi-analytical model and the FE calculation.

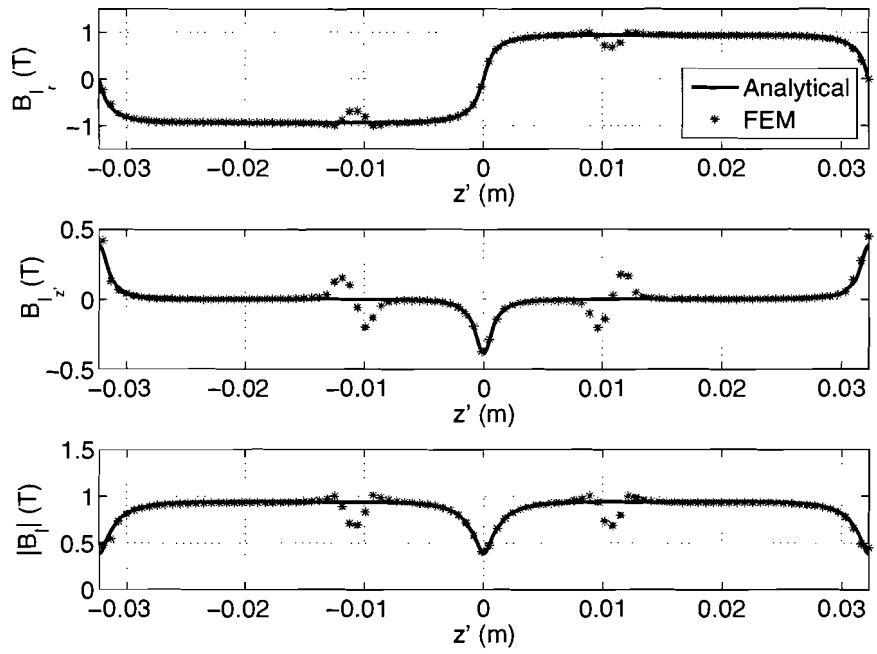

Fig. 3.3: Magnetic flux density of the magnets in the air gap for the radial magnetised topology for $\Delta_z = 0$.

Good agreement has been found between the semi-analytical solution and the FE solution. The only difference is the slotting effect which introduces small fluctuations at the positions where the coils are situated. This error is introduced due the abstraction from

a slotted stator to a full iron tube. In Fig. 3.4, the amplitude of the radial and axial component of the magnetic field of the magnets is plotted for every harmonic number, n. It can be observed that the amplitude of the harmonics of the 23^{th} order and higher have an amplitude of less then 1% of the amplitude of the first harmonic of the radial magnetic field.

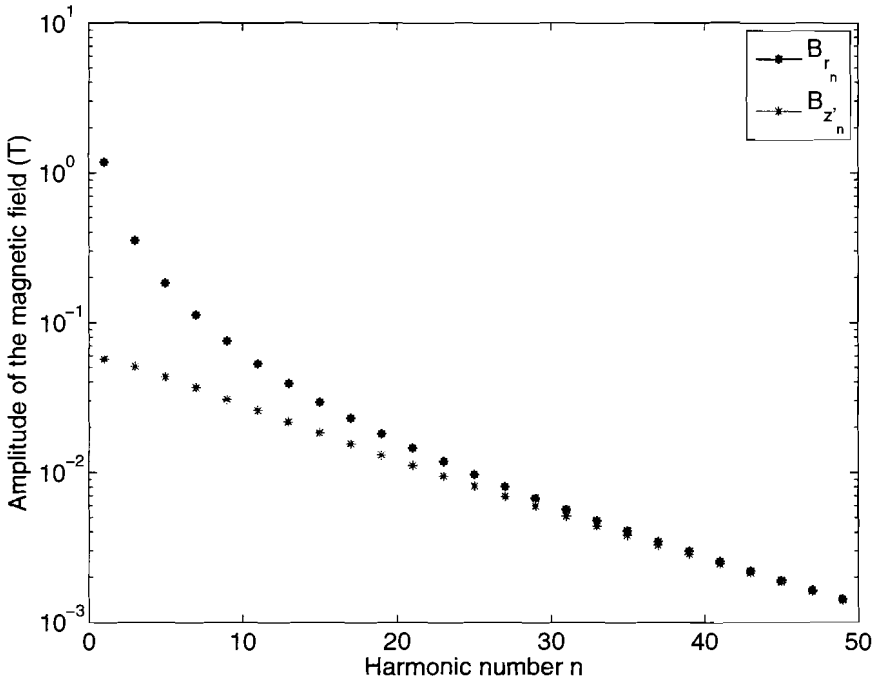

Fig. 3.4: Amplitude of the different harmonics of the magnetic field of the magnets.

3.1.2 Halbach magnetised topology

Now the halbach magnetised topology is considered. The same procedure is followed as done for the radial magnetised topology. The magnetisation has now a radial and axial component which are ideally sinusoidal distributed, $\mathbf{M} = M_r\mathbf{e}_r + M_{z'}\mathbf{e}_{z'}$ with

$$M_r = M_0 \sin(m_1 z'), \tag{3.58}$$
$$M_{z'} = M_0 \cos(m_1 z'), \tag{3.59}$$

where in this case $m_1 = \frac{\pi}{\tau_p}$ is the only spatial frequency and $M_0 = \frac{B_{rem}}{\mu_0}$.

So this gives for the right hand side of equation (3.21)

$$-\mu_0 \nabla \times \mathbf{M} = -\mu_0 \left(\frac{\delta M_r}{\delta z'} - \frac{\delta M_{z'}}{\delta r} \right) \mathbf{e}_\theta = -\mu_0 \left(\frac{\delta \big(M_0 \sin(m_1 z') \big)}{\delta z'} \right) \mathbf{e}_\theta = -m_1 B_{rem} \cos(m_1 z') \mathbf{e}_\theta. \tag{3.60}$$

Therefore, the Poisson and Laplace equations (3.21) and (3.20) can be written as

$$\begin{aligned} \nabla^2 \mathbf{A}_{\mathrm{I}_\theta} &= \left(\frac{\partial^2 A_{\mathrm{I}_\theta}}{\partial r^2} + \frac{1}{r}\frac{\partial A_{\mathrm{I}_\theta}}{\partial r} - \frac{2}{r^2} A_{\mathrm{I}_\theta} + \frac{\partial^2 A_{\mathrm{I}_\theta}}{\partial z^2} \right) \mathbf{e}_\theta \\ &= \left(-\frac{\delta}{\delta z'} B_{\mathrm{I}_r} + \frac{\delta}{\delta r} B_{\mathrm{I}_{z'}} \right) \mathbf{e}_\theta = \mathbf{0}, \end{aligned} \tag{3.61}$$

$$\begin{aligned} \nabla^2 \mathbf{A}_{\mathrm{II}_\theta} &= \left(\frac{\partial^2 A_{\mathrm{II}_\theta}}{\partial r^2} + \frac{1}{r}\frac{\partial A_{\mathrm{II}_\theta}}{\partial r} - \frac{2}{r^2} A_{\mathrm{II}_\theta} + \frac{\partial^2 A_{\mathrm{II}_\theta}}{\partial z^2} \right) \mathbf{e}_\theta \\ &= \left(-\frac{\delta}{\delta z'} B_{\mathrm{II}_r} + \frac{\delta}{\delta r} B_{\mathrm{II}_{z'}} \right) \mathbf{e}_\theta = -m_1 B_{rem} \cos(m_1 z') \mathbf{e}_\theta. \end{aligned} \tag{3.62}$$

These differential equations are again solved by the method of seperation of variables. The solution is given by

$$A_{\mathrm{I}_\theta} = -\frac{1}{m_1} \Big(a_1 \mathcal{B}_{\mathcal{I}1}(m_1 r) + b_1 \mathcal{B}_{\mathcal{K}1}(m_1 r) \Big) \cos(m_1 z'), \tag{3.63}$$

$$\begin{aligned} A_{\mathrm{II}_\theta} = -\frac{1}{m_1} \Big\{ &\Big(\mathcal{K}_a(m_1 r) + a_2 \Big) \mathcal{B}_{\mathcal{I}1}(m_1 r) \\ &+ \Big(-\mathcal{K}_b(m_1 r) + b_2 \Big) \mathcal{B}_{\mathcal{K}1}(m_1 r) \Big\} \cos(m_1 z'), \end{aligned} \tag{3.64}$$

where a_1, a_2, b_1 and b_2, are constants resulting from the boundary conditions and $\mathcal{K}_a(m_1 r)$, $\mathcal{K}_b(m_1 r)$ are functions which result from substitution of (3.64) into (3.62). This

gives the following solutions for B_{I_r}, $B_{\mathrm{I}_{z'}}$, B_{II_r} and $B_{\mathrm{II}_{z'}}$

$$B_{\mathrm{I}_r}(r,z') = -\Big(a_1\mathcal{B}_{\mathcal{I}1}(m_1r) + b_1\mathcal{B}_{\mathcal{K}1}(m_1r)\Big)\sin(m_1z'), \tag{3.65}$$

$$B_{\mathrm{I}_{z'}}(r,z') = -\Big(a_1\mathcal{B}_{\mathcal{I}0}(m_1r) - b_1\mathcal{B}_{\mathcal{K}0}(m_1r)\Big)\cos(m_1z'), \tag{3.66}$$

$$\begin{aligned} B_{\mathrm{II}_r}(r,z') = -\Big\{&\Big(\mathcal{K}_a(m_1r) + a_2\Big)\mathcal{B}_{\mathcal{I}1}(m_1r) \\ &- \Big(\mathcal{K}_b(m_1r) - b_2\Big)\mathcal{B}_{\mathcal{K}1}(m_1r)\Big\}\sin(m_1z'), \end{aligned} \tag{3.67}$$

$$\begin{aligned} B_{\mathrm{II}_{z'}}(r,z') = -\Big\{&\Big(\mathcal{K}_a(m_1r) + a_2\Big)\mathcal{B}_{\mathcal{I}0}(m_1r) \\ &+ \Big(\mathcal{K}_b(m_1r) - b_2\Big)\mathcal{B}_{\mathcal{K}0}(m_1r)\Big\}\cos(m_1z'). \end{aligned} \tag{3.68}$$

Substitution of (3.64) into (3.62), using (6.10) and (6.11), gives

$$\begin{aligned} m_1\Big\{&\Big(\mathcal{K}_a(m_1r) + a_2\Big)\mathcal{B}_{\mathcal{I}1}(m_1r) + \Big(-\mathcal{K}_b(pr) + b_2\Big)\mathcal{B}_{\mathcal{K}1}(m_1r)\Big\}\cos(m_1z') \\ &- \Big\{m_1\Big(\mathcal{K}_a(m_1r) + a_2\Big)\mathcal{B}_{\mathcal{I}1}(m_1r) - m_1\Big(\mathcal{K}_b(m_1r) - b_2\Big)\mathcal{B}_{\mathcal{K}1}(m_1r) \\ &+ \frac{\delta\mathcal{K}_a(m_1r)}{\delta r}\mathcal{B}_{\mathcal{I}0}(m_1r) + \frac{\delta\mathcal{K}_b(m_1r)}{\delta r}\mathcal{B}_{\mathcal{K}0}(m_1r)\Big\}\cos(m_1z') = -m_1B_{rem}\cos(m_1z'), \end{aligned} \tag{3.69}$$

which simplifies to:

$$\frac{\delta\mathcal{K}_a(m_1r)}{\delta r}\mathcal{B}_{\mathcal{I}0}(m_1r) + \frac{\delta\mathcal{K}_b(m_1r)}{\delta r}\mathcal{B}_{\mathcal{K}0}(m_1r) = m_1B_{rem}. \tag{3.70}$$

Now define again

$$\mathcal{K}_a(m_1r) = B_{rem}\int_{l_3}^{m_1r}\frac{\mathcal{B}_{\mathcal{K}1}(x)dx}{\mathcal{B}_{\mathcal{I}1}(x)\mathcal{B}_{\mathcal{K}0}(x) + \mathcal{B}_{\mathcal{K}1}(x)\mathcal{B}_{\mathcal{I}0}(x)}, \tag{3.71}$$

$$\mathcal{K}_b(m_1r) = B_{rem}\int_{l_4}^{m_1r}\frac{\mathcal{B}_{\mathcal{I}1}(x)dx}{\mathcal{B}_{\mathcal{I}1}(x)\mathcal{B}_{\mathcal{K}0}(x) + \mathcal{B}_{\mathcal{K}1}(x)\mathcal{B}_{\mathcal{I}0}(x)}, \tag{3.72}$$

for some lowerbounds l_3 and l_4 which will be defined later.

If (3.71) and (3.72) is substituted into (3.70), using property (3.40), it results in

$$\begin{aligned} m_1B_{rem}&\frac{\mathcal{B}_{\mathcal{K}1}(m_1r)}{\mathcal{B}_{\mathcal{I}1}(m_1r)\mathcal{B}_{\mathcal{K}0}(m_1r) + \mathcal{B}_{\mathcal{K}1}(m_1r)\mathcal{B}_{\mathcal{I}0}(m_1r)}\mathcal{B}_{\mathcal{I}0}(m_1r) \\ &+ m_1B_{rem}\frac{\mathcal{B}_{\mathcal{I}1}(m_1r)}{\mathcal{B}_{\mathcal{I}1}(m_1r)\mathcal{B}_{\mathcal{K}0}(m_1r) + \mathcal{B}_{\mathcal{K}1}(m_1r)\mathcal{B}_{\mathcal{I}0}(m_1r)}\mathcal{B}_{\mathcal{K}0}(m_1r) = m_1B_{rem}, \end{aligned} \tag{3.73}$$

which is again true which again concludes that the functions $\mathcal{K}_a(m_1 r)$ and $\mathcal{K}_b(m_1 r)$ can be described as equations (3.71) and (3.72), respectively. Note that the lowerbounds l_3 and l_4 used in (3.71) and (3.72) can have any random value.

Now the constants a_1, a_2, b_1 and b_2 are derived with the given boundary conditions. These are the same as in the radial magnetised topology (3.42)-(3.45).

- The first boundary condition (3.42) gives:

$$B_{\mathrm{I}_{z'}}(R_s, z') = -\Big(a_1 \mathcal{B}_{\mathcal{I}0}(m_1 R_i) - b_1 \mathcal{B}_{\mathcal{K}0}(m_1 R_i)\Big)\cos(m_1 z') = 0,$$
$$\Downarrow$$
$$a_1 \mathcal{B}_{\mathcal{I}0}(m_1 R_i) = b_1 \mathcal{B}_{\mathcal{K}0}(m_1 R_i),$$

which for $\mathcal{B}_{\mathcal{I}0}(m_1 R_i) = c_1$ and $\mathcal{B}_{\mathcal{K}0}(m_1 R_i) = c_2$ reduces to

$$\begin{aligned} a_1 c_1 &= b_1 c_2, \\ &\Downarrow \\ b_1 &= \frac{c_1}{c_2} a_1. \end{aligned} \tag{3.74}$$

- The second boundary condition (3.43) gives

$$\begin{aligned} B_{\mathrm{II}_{z'}}(R_r, z') = -\Big\{ &\Big(\mathcal{K}_a(m_1 R_r) + a_2\Big)\mathcal{B}_{\mathcal{I}0}(m_1 R_r) \\ &+ \Big(\mathcal{K}_b(m_1 R_r) - b_2\Big)\mathcal{B}_{\mathcal{K}0}(m_1 R_r)\Big\}\cos(m_1 z') = 0, \end{aligned}$$
$$\Downarrow$$
$$\Big(\mathcal{K}_a(m_1 R_r) + a_2\Big)\mathcal{B}_{\mathcal{I}0}(m_1 R_r) = -\Big(\mathcal{K}_b(m_1 R_r) - b_2\Big)\mathcal{B}_{\mathcal{K}0}(m_1 R_r),$$

which for $\mathcal{B}_{\mathcal{I}0}(m_1 R_r) = c_3$ and $\mathcal{B}_{\mathcal{K}0}(m_1 R_r) = c_4$ reduces to

$$\Big(\mathcal{K}_a(m_1 R_r) + a_2\Big)c_3 = -\Big(\mathcal{K}_b(m_1 R_r) - b_2\Big)c_4. \tag{3.75}$$

Because the lowerbounds l_3 and l_4 can be chosen randomly, this expression can be simplified by taking $l_3 = l_4 = m_1 R_r$ which results in $\mathcal{K}_a(m_1 R_r) = 0$ and $\mathcal{K}_b(m_1 R_r) = 0$ and simplifies (3.75) to

$$b_2 = \frac{c_3}{c_4} a_2. \tag{3.76}$$

• The third boundary condition (3.44) gives

$$B_{\mathrm{I}_r}(R_m, z') = B_{\mathrm{II}_r}(R_m, z'),$$
$$\Downarrow$$
$$-\Big(a_1\mathcal{B}_{\mathcal{I}1}(m_1R_m) + b_1\mathcal{B}_{\mathcal{K}1}(m_1R_m)\Big)\sin(m_1z')$$
$$= -\Big\{\Big(\mathcal{K}_a(m_1R_m) + a_2\Big)\mathcal{B}_{\mathcal{I}1}(m_1R_m) + \Big(-\mathcal{K}_b(m_1R_m) + b_2\Big)\mathcal{B}_{\mathcal{K}1}(m_1R_m)\Big\}\sin(m_1z'),$$

which for $\mathcal{B}_{\mathcal{I}1}(m_1R_m) = c_7$ and $\mathcal{B}_{\mathcal{K}1}(m_1R_m) = c_8$ together with (3.74) and (3.76) reduces to

$$\begin{aligned} a_1c_7 + b_1c_8 &= \Big(\mathcal{K}_a(m_1R_m) + a_2\Big)c_7 - \Big(+\mathcal{K}_b(m_1R_m) - b_2\Big)c_8, \\ &\Downarrow \\ \Big(\frac{c_7}{c_8} + \frac{c_1}{c_2}\Big)a_1 - \Big(\frac{c_7}{c_8} + \frac{c_3}{c_4}\Big)a_2 &= \mathcal{K}_a(m_1R_m)\frac{c_7}{c_8} - \mathcal{K}_b(m_1R_m). \end{aligned} \tag{3.77}$$

• The fourth boundary condition (3.45) gives:

$$\begin{aligned} H_{\mathrm{I}_{z'}}(R_m, z') &= H_{\mathrm{II}_{z'}}(R_m, z'), \\ &\Downarrow \\ \frac{1}{\mu_0}B_{\mathrm{I}_{z'}}(R_m, z') &= \frac{1}{\mu_0\mu_r}B_{\mathrm{II}_{z'}}(R_m, z') + \frac{1}{\mu_r}M_{z'}(R_m, z'), \\ &\Downarrow \\ \mu_rB_{\mathrm{I}_{z'}}(R_m, z') &= B_{\mathrm{II}_{z'}}(R_m, z') + B_{rem}\cos(m_1z'), \\ &\Downarrow \end{aligned}$$

$$-\mu_r\Big(a_1\mathcal{B}_{\mathcal{I}0}(m_1R_m) - b_1\mathcal{B}_{\mathcal{K}0}(m_1R_m)\Big)\cos(m_1z') = -\Big\{\Big(\mathcal{K}_a(m_1R_m) + a_2\Big)\mathcal{B}_{\mathcal{I}0}(m_1R_m)$$
$$+\Big(\mathcal{K}_b(m_1R_m) - b_2\Big)\mathcal{B}_{\mathcal{K}0}(m_1R_m)\Big\}\cos(m_1z') + B_{rem}\cos(m_1z'),$$

which for $\mathcal{B}_{\mathcal{I}0}(m_1R_m) = c_5$ and $\mathcal{B}_{\mathcal{K}0}(m_1R_m) = c_6$ together with (3.74) and (3.76) reduces to

$$\mu_r(a_1c_5 - b_1c_6) = \Big(\mathcal{K}_a(m_1R_m) + a_2\Big)c_5 + \Big(\mathcal{K}_b(m_1R_m) - b_2\Big)c_6 - B_{rem},$$
$$\Downarrow$$
$$\mu_r\Big(\frac{c_5}{c_6} - \frac{c_1}{c_2}\Big)a_1 - \Big(\frac{c_5}{c_6} - \frac{c_3}{c_4}\Big)a_2 = \mathcal{K}_a(m_1R_m)\frac{c_5}{c_6} + \mathcal{K}_b(m_1R_m) - \frac{B_{rem}}{c_6}. \tag{3.78}$$

In summary:

$$
\begin{aligned}
c_1 &= \mathcal{B}_{\mathcal{I}0}(m_1 R_i), & c_2 &= \mathcal{B}_{\mathcal{K}0}(m_1 R_i), \\
c_3 &= \mathcal{B}_{\mathcal{I}0}(m_1 R_r), & c_4 &= \mathcal{B}_{\mathcal{K}0}(m_1 R_r), \\
c_5 &= \mathcal{B}_{\mathcal{I}0}(m_1 R_m), & c_6 &= \mathcal{B}_{\mathcal{K}0}(m_1 R_m), \\
c_7 &= \mathcal{B}_{\mathcal{I}1}(m_1 R_m), & c_8 &= \mathcal{B}_{\mathcal{K}1}(m_1 R_m),
\end{aligned} \tag{3.79}
$$

$$
\mathcal{K}_a(m_1 r) = B_{rem} \int_{m_1 R_r}^{m_n r} \frac{\mathcal{B}_{\mathcal{K}1}(x)dx}{\mathcal{B}_{\mathcal{I}1}(x)\mathcal{B}_{\mathcal{K}0}(x) + \mathcal{B}_{\mathcal{K}1}(x)\mathcal{B}_{\mathcal{I}0}(x)}, \tag{3.80}
$$

$$
\mathcal{K}_b(m_1 r) = B_{rem} \int_{m_1 R_r}^{m_n r} \frac{\mathcal{B}_{\mathcal{I}1}(x)dx}{\mathcal{B}_{\mathcal{I}1}(x)\mathcal{B}_{\mathcal{K}0}(x) + \mathcal{B}_{\mathcal{K}1}(x)\mathcal{B}_{\mathcal{I}0}(x)}, \tag{3.81}
$$

and the set of four linear equations, (3.74), (3.76), (3.77) and (3.78) result in

$$
a_1 = \frac{\left(\frac{c_5}{c_6} + \frac{c_7}{c_8}\right)\left(\frac{c_3}{c_4}\mathcal{K}_a(m_1 R_m) + \mathcal{K}_b(m_1 R_m) - \frac{B_{rem}}{c_6}\right)}{\left(\frac{c_3}{c_4} - \frac{c_5}{c_6}\right)\left(\frac{c_1}{c_2} + \frac{c_7}{c_8}\right) + \mu_r\left(\frac{c_3}{c_4} + \frac{c_7}{c_8}\right)\left(\frac{c_5}{c_6} - \frac{c_1}{c_2}\right)}, \tag{3.82}
$$

$$
a_2 = \frac{\left(\frac{c_5}{c_6}\mathcal{K}_a(m_1 R_m) + \mathcal{K}_b(m_1 R_m)\right) - \mu_r\left(\frac{c_5}{c_6} - \frac{c_1}{c_2}\right)a_1}{\left(\frac{c_3}{c_4} - \frac{c_5}{c_6}\right)}, \tag{3.83}
$$

$$
b_1 = \frac{c_1}{c_2}a_1, \tag{3.84}
$$

$$
b_2 = \frac{c_3}{c_4}a_2. \tag{3.85}
$$

These field equations are implemented in Matlab and the solution is calculated in the center of the air gap for $\Delta_z = 0$ where the results are shown in Fig. 3.5. It can be observed that the magnetic field is perfectly sinusoidal as expected. No FE calculation could be performed for an ideal halbach magnetised topology due to the current software limitations.

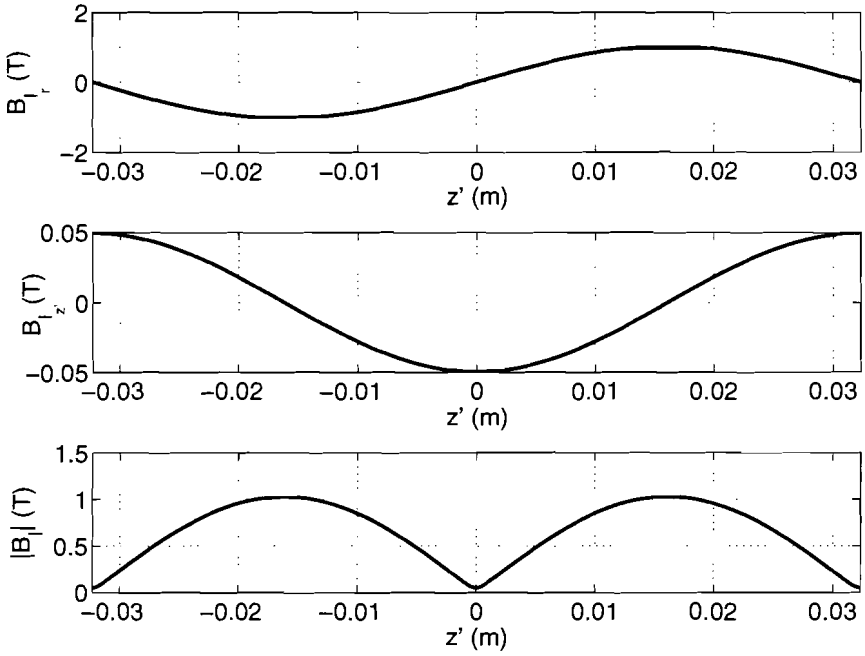

Fig. 3.5: Magnetic flux density of the magnets in the air gap for the halbach magnetised topology for $\Delta_z = 0$.

3.1.3 The slotting effect

In general, a slotted machine will be used because of higher performance. A slotted machine has a smaller air gap and therefore, the main reluctance is lower which results in a higher magnetic field and consequently a higher force. Nevertheless, the slots introduce two effects. The first effect is the distortion in the field of the magnets at the point between the slots, see Fig. 3.6. This distortion was already mentioned in section 3.1.1 in

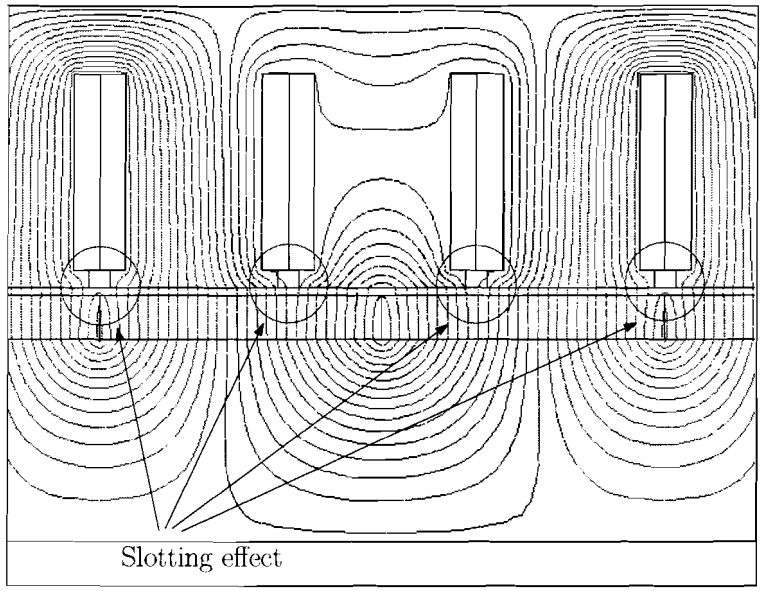

Fig. 3.6: Field distortion between the slots

Fig. 3.3. The second effect is that the magnetic field does not cross the air gap in the radial direction at the positions of the coils, but it frings towards the slots. introducing an axial component. This fringing field will further be mentioned as the slotting effect, which has a related cogging force. Also, since a part of the flux has to fring towards the slots, the flux path will be longer, increasing the reluctance and therefore also decreasing the magnetic flux density.

The second effect is that a part of the flux flows through the coils instead of through the back iron which is in fact a sort of leakage flux since this amount of flux only contributes contribute to the total flux linkage of the coil. The total flux linkage is therefore decreased, and consequently the emf and force decreases. Altough this is not visible in Fig. 3.6, this effect is always present. But, due to the small windings compared to the slot width, this effect will be small in this case, especially at saturation.

When a MEC model is considered, the length of the air gap, g, is extended in order to account for the leakage flux. This is done by means of a Carter's coefficient, which determines the length of the equivalent air gap, g', depending on the tooth pitch, τ_t, and the width of the windings, τ_w. Carter derived this empherical formula by the conformal mapping of a rectangular tooth, as also shown in [25], but since salient poles are considered, this formula is not exact. With this coefficient, the form of the flux lines and the flux density cannot be determined, and it is impossible to calculate the cogging force as function of translator displacement due to the slotting effect.

In [1], a relative permeance function is used, which describes the variation of the per-

meablity in the air gap. This permeance function is determined by means of 2D FE calculations and curve fitting. But, since this is a very time-consuming method, this will not be considered here. In Chapter 5, the slotting effect is determined by means of the Schwarz-Christoffel conformal mapping of the salient slotted structure.

3.2 EMF calculation

For the calculation of the EMF, the flux linkage imposed by every phase is needed. Since only the magnetic field distribution in the air gap is known, the amount of flux in the air gap that flows through the teeth of the corresponding phase needs to be calculated. This is approximatly accomplished by integrating the radial component of the magnetic flux density of the magnets, B_{l_r}, at the inner radius of the stator, R_i, for the area of the tooth of the phase that is considered, see Fig. 3.7 for an illustration. Thus, the flux linkage of

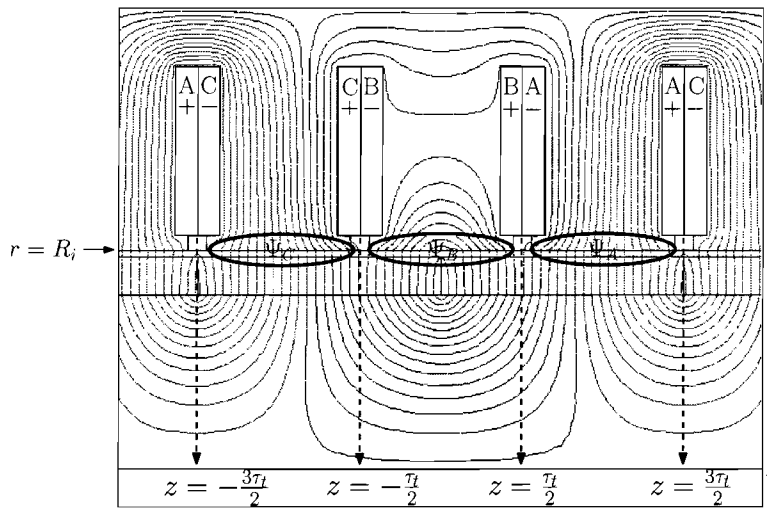

Fig. 3.7: Illustration of the flux imposed by every phase

every phase can be calculated as

$$\begin{aligned}
\Psi_A &= NN_{sp}\int_{S_{slot_A}} B_{\mathrm{l}_r}(r,z')dS,\\
\Psi_B &= NN_{sp}\int_{S_{slot_B}} B_{\mathrm{l}_r}(r,z')dS,\\
\Psi_C &= NN_{sp}\int_{S_{slot_C}} B_{\mathrm{l}_r}(r,z')dS,
\end{aligned} \tag{3.86}$$

where N is the number of windings, N_{sp} is the number of slots per phase, S_{slot} is the area of the slot at the inner radius of the stator and therefore, $dS = 2\pi R_i dz$ which gives

$$\begin{aligned}
\Psi_A &= 2\pi R_i NN_{sp}\int_{\frac{\tau_t}{2}}^{\frac{3\tau_t}{2}} B_{\mathrm{l}_r}(R_i,z')dz,\\
\Psi_B &= 2\pi R_i NN_{sp}\int_{-\frac{\tau_t}{2}}^{\frac{\tau_t}{2}} B_{\mathrm{l}_r}(R_i,z')dz,\\
\Psi_C &= 2\pi R_i NN_{sp}\int_{-\frac{3\tau_t}{2}}^{-\frac{\tau_t}{2}} B_{\mathrm{l}_r}(R_i,z')dz,
\end{aligned} \tag{3.87}$$

with N the number of windings and $N_{sp} = \frac{N_s}{N_{ph}}$ the number of slots per phase. Filling in the equation of B_{I_r}, gives

$$\begin{aligned}
\Psi_A &= -2\pi R_i N N_{sp} \int_{\frac{\tau_t}{2}}^{\frac{3\tau_t}{2}} \sum_{n=1}^{\infty} \Big(a_{1n}\mathcal{B}_{\mathcal{I}1}(m_n R_i) + b_{1n}\mathcal{B}_{\mathcal{K}1}(m_n R_i) \Big) \sin\Big(m_n(z-\Delta_z) \Big) dz, \\
\Psi_B &= -2\pi R_i N N_{sp} \int_{-\frac{\tau_t}{2}}^{\frac{\tau_t}{2}} \sum_{n=1}^{\infty} \Big(a_{1n}\mathcal{B}_{\mathcal{I}1}(m_n R_i) + b_{1n}\mathcal{B}_{\mathcal{K}1}(m_n R_i) \Big) \sin\Big(m_n(z-\Delta_z) \Big) dz, \\
\Psi_C &= -2\pi R_i N N_{sp} \int_{-\frac{3\tau_t}{2}}^{-\frac{\tau_t}{2}} \sum_{n=1}^{\infty} \Big(a_{1n}\mathcal{B}_{\mathcal{I}1}(m_n R_i) + b_{1n}\mathcal{B}_{\mathcal{K}1}(m_n R_i) \Big) \sin\Big(m_n(z-\Delta_z) \Big) dz.
\end{aligned} \tag{3.88}$$

Since the equations hold for every n, the integral and summation may be switched, which gives

$$\begin{aligned}
\Psi_A &= -2\pi R_i N N_{sp} \sum_{n=1}^{\infty} \Big(a_{1n}\mathcal{B}_{\mathcal{I}1}(m_n R_i) + b_{1n}\mathcal{B}_{\mathcal{K}1}(m_n R_i) \Big) \int_{\frac{\tau_t}{2}}^{\frac{3\tau_t}{2}} \sin\Big(m_n(z-\Delta_z) \Big) dz, \\
\Psi_B &= -2\pi R_i N N_{sp} \sum_{n=1}^{\infty} \Big(a_{1n}\mathcal{B}_{\mathcal{I}1}(m_n R_i) + b_{1n}\mathcal{B}_{\mathcal{K}1}(m_n R_i) \Big) \int_{-\frac{\tau_t}{2}}^{\frac{\tau_t}{2}} \sin\Big(m_n(z-\Delta_z) \Big) dz, \\
\Psi_C &= -2\pi R_i N N_{sp} \sum_{n=1}^{\infty} \Big(a_{1n}\mathcal{B}_{\mathcal{I}1}(m_n R_i) + b_{1n}\mathcal{B}_{\mathcal{K}1}(m_n R_i) \Big) \int_{-\frac{3\tau_t}{2}}^{-\frac{\tau_t}{2}} \sin\Big(m_n(z-\Delta_z) \Big) dz,
\end{aligned} \tag{3.89}$$

and after evaluation, the expressions become

$$\begin{aligned}
\Psi_A =& 2\pi R_i N N_{sp} \sum_{n=1}^{\infty} \frac{1}{m_n} \Big(a_{1n}\mathcal{B}_{\mathcal{I}1}(m_n R_i) + b_{1n}\mathcal{B}_{\mathcal{K}1}(m_n R_i) \Big) \\
& \Big\{ \cos\Big(m_n(\frac{3\tau_t}{2} - \Delta_z) \Big) - \cos\Big(m_n(\frac{\tau_t}{2} - \Delta_z) \Big) \Big\}, \\
\Psi_B =& 2\pi R_i N N_{sp} \sum_{n=1}^{\infty} \frac{1}{m_n} \Big(a_{1n}\mathcal{B}_{\mathcal{I}1}(m_n R_i) + b_{1n}\mathcal{B}_{\mathcal{K}1}(m_n R_i) \Big) \\
& \Big\{ \cos\Big(m_n(\frac{\tau_t}{2} - \Delta_z) \Big) - \cos\Big(m_n(\frac{\tau_t}{2} + \Delta_z) \Big) \Big\}, \\
\Psi_C =& 2\pi R_i N N_{sp} \sum_{n=1}^{\infty} \frac{1}{m_n} \Big(a_{1n}\mathcal{B}_{\mathcal{I}1}(m_n R_i) + b_{1n}\mathcal{B}_{\mathcal{K}1}(m_n R_i) \Big) \\
& \Big\{ \cos\Big(m_n(\frac{\tau_t}{2} + \Delta_z) \Big) - \cos\Big(m_n(\frac{3\tau_t}{2} + \Delta_z) \Big) \Big\}.
\end{aligned} \tag{3.90}$$

Using (6.16) and $\tau_t = \frac{2\tau_p}{3}$, simplifies the equations to

$$\begin{aligned}
\Psi_A &= -4\pi R_i N N_{sp} \sum_{n=1}^{\infty} \frac{1}{m_n} \Big(a_{1n} \mathcal{B}_{\mathcal{I}1}(m_n R_i) + b_{1n} \mathcal{B}_{\mathcal{K}1}(m_n R_i) \Big) \\
&\quad \sin\left(n\frac{\pi}{3}\right) \sin\Big(m_n(\tau_t - \Delta_z)\Big), \\
\Psi_B &= -4\pi R_i N N_{sp} \sum_{n=1}^{\infty} \frac{1}{m_n} \Big(a_{1n} \mathcal{B}_{\mathcal{I}1}(m_n R_i) + b_{1n} \mathcal{B}_{\mathcal{K}1}(m_n R_i) \Big) \\
&\quad \sin\left(n\frac{\pi}{3}\right) \sin\Big(-m_n \Delta_z\Big), \\
\Psi_C &= -4\pi R_i N N_{sp} \sum_{n=1}^{\infty} \frac{1}{m_n} \Big(a_{1n} \mathcal{B}_{\mathcal{I}1}(m_n R_i) + b_{1n} \mathcal{B}_{\mathcal{K}1}(m_n R_i) \Big) \\
&\quad \sin\left(n\frac{\pi}{3}\right) \sin\Big(m_n(-\tau_t - \Delta_z)\Big).
\end{aligned} \tag{3.91}$$

The EMF for each phase can be calculated as follows

$$\begin{aligned}
e_A &= -\frac{\partial \Psi_a}{\partial t} = -\frac{\partial \Psi_a}{\partial \Delta_z}\frac{\partial \Delta_z}{\partial t} = -\frac{\partial \Psi_a}{\partial \Delta_z} v(t), \\
e_B &= -\frac{\partial \Psi_b}{\partial t} = -\frac{\partial \Psi_b}{\partial \Delta_z}\frac{\partial \Delta_z}{\partial t} = -\frac{\partial \Psi_b}{\partial \Delta_z} v(t), \\
e_C &= -\frac{\partial \Psi_c}{\partial t} = -\frac{\partial \Psi_c}{\partial \Delta_z}\frac{\partial \Delta_z}{\partial t} = -\frac{\partial \Psi_c}{\partial \Delta_z} v(t),
\end{aligned} \tag{3.92}$$

which results in, after filling in the equations for the flux linkages,

$$\begin{aligned}
e_A &= -4\pi R_i v(t) N N_{sp} \sum_{n=1}^{\infty} \Big(a_{1n} \mathcal{B}_{\mathcal{I}1}(m_n R_i) + b_{1n} \mathcal{B}_{\mathcal{K}1}(m_n R_i) \Big) \\
&\quad \sin\left(n\frac{\pi}{3}\right) \cos\Big(m_n(\tau_t - \Delta_z)\Big), \\
e_B &= -4\pi R_i v(t) N N_{sp} \sum_{n=1}^{\infty} \Big(a_{1n} \mathcal{B}_{\mathcal{I}1}(m_n R_i) + b_{1n} \mathcal{B}_{\mathcal{K}1}(m_n R_i) \Big) \\
&\quad \sin\left(n\frac{\pi}{3}\right) \cos\Big(m_n \Delta_z\Big), \\
e_C &= -4\pi R_i v(t) N N_{sp} \sum_{n=1}^{\infty} \Big(a_{1n} \mathcal{B}_{\mathcal{I}1}(m_n R_i) + b_{1n} \mathcal{B}_{\mathcal{K}1}(m_n R_i) \Big) \\
&\quad \sin\left(n\frac{\pi}{3}\right) \cos\Big(m_n(\tau_t + \Delta_z)\Big).
\end{aligned} \tag{3.93}$$

These EMF waveforms are calculated for a constant translator speed of v=0.5 m/s, and a displacement of 360 electrical degrees or $\Delta_z = 0...2\tau_p$. The results are shown in Fig. 3.8

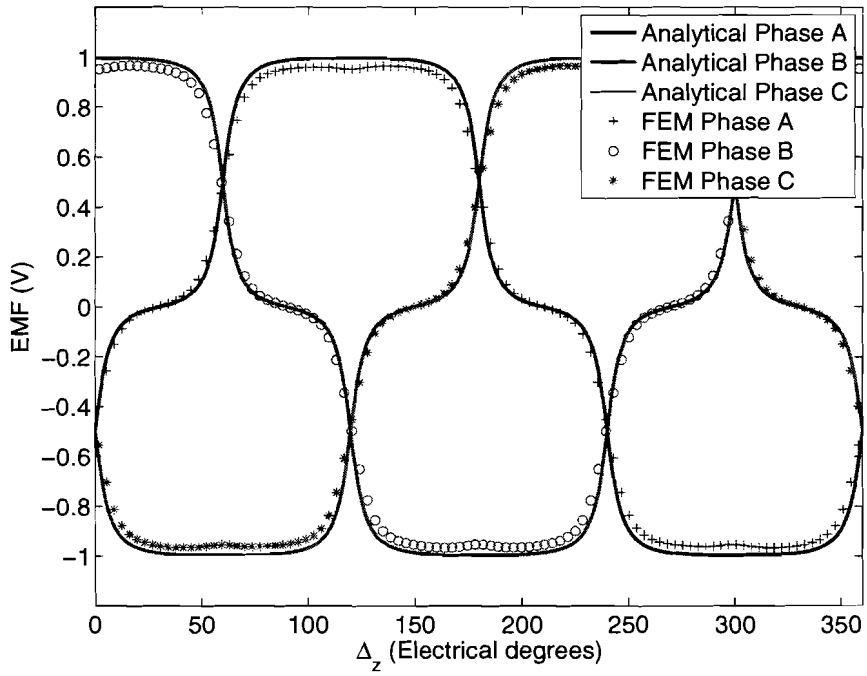

Fig. 3.8: Back EMF per winding at v=0.5 m/s for the numerical calculation and the FE solution.

together with the FE solution. The number of windings, N, is equal to one giving the EMF per winding. Again acceptable agreement has been found, altough the FE solution is slightly lower, which is due the slotting effect which is not incorporated in the semi-analytical model. The assumption is made that the amount of flux entering the tooth at the radius R_i links with every winding of the coil of the considered slot. However, a part of the total flux leaks through the coils instead of flowing through the back iron of the stator which reduces the total flux linkage and hence the EMF.

3.3 Magnetic field of the stator currents

In this section the semi-analytical formulation of the magnetic field in the air gap due to the stator currents is derived. The slotted stator is a complex structure and it is not possible to split it up in radial regions as done in Section 2.1. This is due to the stator slots and windings which introduce boundary conditions in the axial direction. Therefore, the abstraction is made by ignoring everything that happens within the stator and only look at the field distribution in the air gap. Thus, consider the stator as a full iron tube and the stator currents as a current sheet which is positioned at the inner radius of the stator, R_i. This is illustrated in Fig. 3.9. Hereby, the axial boundary conditions are eliminated, which simplifies the mathematical description drastically. Because only the field due to the stator currents is important, the magnets are considered as an air region. This assumption is valid since the μ_r of the magnets is almost equal to 1 using rare-earth permanent magnets. In Fig. 3.10 one pole-pair of the actuator is shown, because the magnets are modelled as an air region region I and region II can be regarded as a new region III (air gap + magnets, $\mu_r = 1$). The iron is again assumed infinitly permeable and end effects are excluded. With these assumptions, four of the five regions are eliminated and only the field equation in one region has to be solved which makes the semi-analytical description simpler as the one for the field of the magnets.

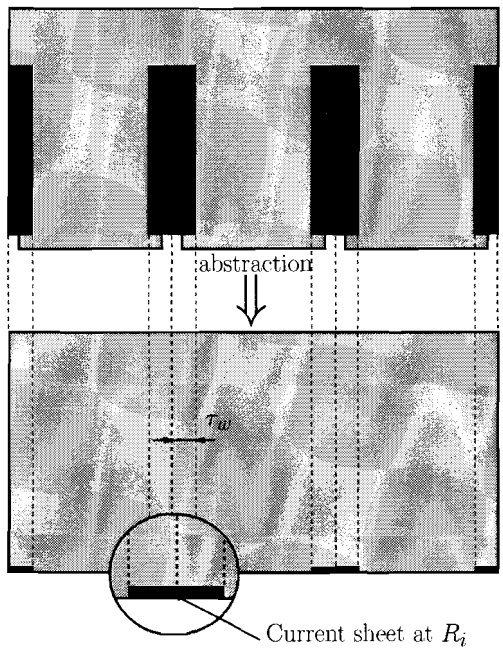

Fig. 3.9: Stator modelling for calculation of the magnetic field in the air gap due to the stator currents.

3.3.1 Current sheet description

This section describes the current sheet distribution at the inner radius of the stator, R_i. The surface current density, J_s, is dependent on two variables. First of all it is dependent on the axial distance, z, due to winding distribution in the stator, which is a concentrated winding topology in this case. Furthermore, it is dependent on the relative

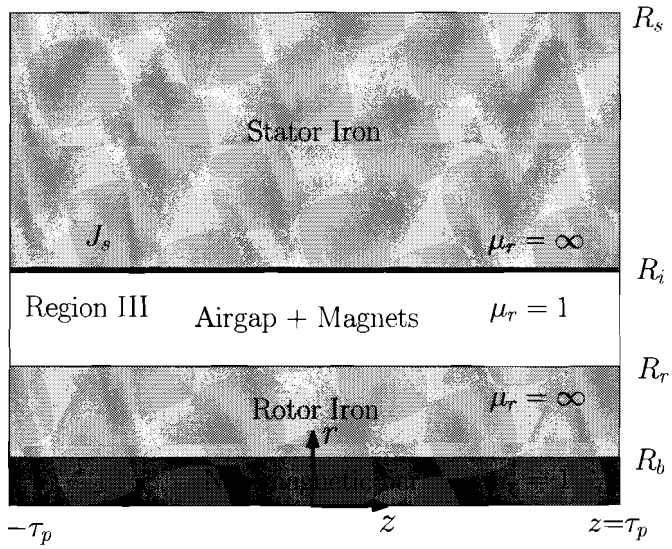

Fig. 3.10: Axial regions of one pole-pair of the TPMA for calculation of the field due to the stator currents.

position between stator and translator, Δ_z, since commutation has to be applied in order to have a constant maximum force for all positions. The surface current density vector can be described as

$$J_s = J_A K_{w_A} + J_B K_{w_B} + J_C K_{w_C},$$

wher J_A, J_B and J_C are the surface current densities and K_{w_A}, K_{w_B} and K_{w_C} are the winding distributions of phase A, B and C respectively. The winding distribution, K_{w_B}, can be described as a Fourier series and K_{w_A} and K_{w_C} are derived from K_{w_B} by a shift in axial direction of $-\tau_t$ and τ_t respectively

$$\begin{aligned} K_{w_A}(z) &= \sum_{n=1}^{\infty} K_{w_n} \sin\Big(m_n(z-\tau_t)\Big), \\ K_{w_B}(z) &= \sum_{n=1}^{\infty} K_{w_n} \sin\Big(m_n z\Big), \\ K_{w_C}(z) &= \sum_{n=1}^{\infty} K_{w_n} \sin\Big(m_n(z+\tau_t)\Big). \end{aligned} \tag{3.94}$$

As seen in (3.94) the Fourier series only consists of sinus terms because it is an odd distribution since the current flows in opposite direction on the other side of the tooth. After Fourier analysis, K_{w_n} is given by

$$K_{w_n} = \frac{2}{\pi n}\left\{ \cos\left(\frac{n\pi}{3}\right) - \cos\left(\frac{n\pi}{3}(1-\frac{3\tau_w}{\tau_p})\right)\right\}. \tag{3.95}$$

Note that any winding topology can be described in this way, only K_{w_n} changes and it may be necessary to include cosinus terms. If we consider sinusoidal excitation, the

surface current densities J_A, J_B and J_C with reference to the proposed coordinate system are given by

$$\begin{aligned} J_A &= J_0 h_c \cos\left(\frac{\pi\Delta_z}{\tau_p} - \frac{2\pi}{3}\right), \\ J_B &= J_0 h_c \cos\left(\frac{\pi\Delta_z}{\tau_p}\right), \\ J_C &= J_0 h_c \cos\left(\frac{\pi\Delta_z}{\tau_p} + \frac{2\pi}{3}\right), \end{aligned} \tag{3.96}$$

where J_0 is the amplitude of the current density and h_c the height of the coils. But since the EMF waveform is more a square waveform, it is more benificial to use DC excitation. In that case the surface current densities J_A, J_B and J_C are described by a Fourier series

$$J_A = J_0 \sum_{k=1}^{\infty} K_{i_k} \cos\left\{k\left(\frac{\pi\Delta_z}{\tau_p} - \frac{2\pi}{3}\right)\right\}, \tag{3.97}$$

$$J_B = J_0 \sum_{k=1}^{\infty} K_{i_k} \cos\left\{k\left(\frac{\pi\Delta_z}{\tau_p}\right)\right\}, \tag{3.98}$$

$$J_C = J_0 \sum_{k=1}^{\infty} K_{i_k} \cos\left\{k\left(\frac{\pi\Delta_z}{\tau_p} - \frac{2\pi}{3}\right)\right\}, \tag{3.99}$$

where K_{i_k} is given by

$$K_{i_k} = \frac{2}{k\pi}\left\{\sin\left(\frac{k\pi}{3}\right) + \sin\left(\frac{2k\pi}{3}\right)\right\} \tag{3.100}$$

The variable k is used instead of n in since both will appear in the force calculation and distinction has to made between both summations. Altough DC excitation gives a higher performance, only AC excitation will be considered from now on since it was not possible to simulate DC excitation in the FE software with the available license and hence no verification was possible.

3.3.2 Field calculation

Now that the surface current density distribution, J_s, as a function of z and Δ_z is known, the magnetic vector potential in region III can be calculated. Since there are no sources inside the air gap, the Poisson equation reduces to a Laplace equation, given by

$$\nabla^2 \mathbf{A}_{\text{III}} = 0, \tag{3.101}$$

and the boundary conditions in this case are

$$\begin{aligned} B_{\text{III}_z}(R_i, z) &= \mu_0 J_s, & (3.102)\\ B_{\text{III}_z}(R_r, z) &= 0, & (3.103) \end{aligned}$$

which together with the Laplace equation (3.101) results in the magnetic vector potential in region III described as

$$A_{\text{III}_\theta} = A_{\text{III}_{\theta_a}} + A_{\text{III}_{\theta_b}} + A_{\text{III}_{\theta_c}}, \tag{3.104}$$

with

$$\begin{aligned} A_{\text{III}_{\theta_A}}(r, z, \Delta_z) = &-\mu_0 J_A \sum_{n=1}^{\infty} \frac{K_{w_n}}{m_n(c_{4n}c_{1n} - c_{2n}c_{3n})} \\ &\left\{ c_{4n}\mathcal{B}_{\mathcal{I}1}(m_n r) + c_{3n}\mathcal{B}_{\mathcal{K}1}(m_n r) \right\} \sin\left(m_n\big(z - \tau_t\big) \right), \\ A_{\text{III}_{\theta_B}}(r, z, \Delta_z) = &-\mu_0 J_B \sum_{n=1}^{\infty} \frac{K_{w_n}}{m_n(c_{4n}c_{1n} - c_{2n}c_{3n})} \\ &\left\{ c_{4n}\mathcal{B}_{\mathcal{I}1}(m_n r) + c_{3n}\mathcal{B}_{\mathcal{K}1}(m_n r) \right\} \sin\left(m_n z \right), \\ A_{\text{III}_{\theta_C}}(r, z, \Delta_z) = &-\mu_0 J_C \sum_{n=1}^{\infty} \frac{K_{w_n}}{m_n(c_{4n}c_{1n} - c_{2n}c_{3n})} \\ &\left\{ c_{4n}\mathcal{B}_{\mathcal{I}1}(m_n r) + c_{3n}\mathcal{B}_{\mathcal{K}1}(m_n r) \right\} \sin\left(m_n\big(z + \tau_t\big) \right). \end{aligned} \tag{3.105}$$

From these equations, the flux densities can be derived with $\mathbf{B} = \nabla \times \mathbf{A}$, which gives

$$
\begin{aligned}
B_{\mathrm{III}_{r_A}} &= \mu_0 J_A \sum_{n=1}^{\infty} \frac{K_{w_n}}{(c_{4_n} c_{1_n} - c_{2_n} c_{3_n})} \\
&\quad \left\{ c_{4_n} \mathcal{B}_{\mathcal{I}1}(m_n r) + c_{3_n} \mathcal{B}_{\mathcal{K}1}(m_n r) \right\} \cos\left(m_n (z - \tau_t) \right), \\
B_{\mathrm{III}_{z_A}} &= -\mu_0 J_A \sum_{n=1}^{\infty} \frac{K_{w_n}}{(c_{4_n} c_{1_n} - c_{2_n} c_{3_n})} \\
&\quad \left\{ c_{4_n} \mathcal{B}_{\mathcal{I}0}(m_n r) - c_{3_n} \mathcal{B}_{\mathcal{K}0}(m_n r) \right\} \sin\left(m_n (z - \tau_t) \right), \\
B_{\mathrm{III}_{r_B}} &= \mu_0 J_B \sum_{n=1}^{\infty} \frac{K_{w_n}}{(c_{4_n} c_{1_n} - c_{2_n} c_{3_n})} \\
&\quad \left\{ c_{4_n} \mathcal{B}_{\mathcal{I}1}(m_n r) + c_{3_n} \mathcal{B}_{\mathcal{K}1}(m_n r) \right\} \cos\left(m_n z \right), \\
B_{\mathrm{III}_{z_B}} &= -\mu_0 J_B \sum_{n=1}^{\infty} \frac{K_{w_n}}{(c_{4_n} c_{1_n} - c_{2_n} c_{3_n})} \\
&\quad \left\{ c_{4_n} \mathcal{B}_{\mathcal{I}0}(m_n r) - c_{3_n} \mathcal{B}_{\mathcal{K}0}(m_n r) \right\} \sin\left(m_n z \right), \\
B_{\mathrm{III}_{r_C}} &= \mu_0 J_C \sum_{n=1}^{\infty} \frac{K_{w_n}}{(c_{4_n} c_{1_n} - c_{2_n} c_{3_n})} \\
&\quad \left\{ c_{4_n} \mathcal{B}_{\mathcal{I}1}(m_n r) + c_{3_n} \mathcal{B}_{\mathcal{K}1}(m_n r) \right\} \cos\left(m_n (z + \tau_t) \right), \\
B_{\mathrm{III}_{z_C}} &= -\mu_0 J_C \sum_{n=1}^{\infty} \frac{K_{w_n}}{(c_{4_n} c_{1_n} - c_{2_n} c_{3_n})} \\
&\quad \left\{ c_{4_n} \mathcal{B}_{\mathcal{I}0}(m_n r) - c_{3_n} \mathcal{B}_{\mathcal{K}0}(m_n r) \right\} \sin\left(m_n (z + \tau_t) \right).
\end{aligned}
\tag{3.106}
$$

These equations are again implemented in MATLAB® for the nominal dimensions given in Table 2.1. The magnetic field of the stator currents is calculated at the radius R_{ag} for $J_0 = 7.5\mathrm{A/mm}^2$ and for sinusoidal excitation, the results together with the FE calculation are given in Fig. 3.11 for $\Delta_z = 0$.

It can be observed that the numerical solution has the same behaviour as the FE solution but the peaks do not coincide with eachother. There is a shift in displacement, which is the same for every peak. The distance between the two positive peaks of the semi-analytical solution is almost equal to τ_{tt} and the distance between the two positive peaks of the FE solution is almost equal to τ_{tp}. This indicates a wrong discription of the current sheet modelling with the wrong value of τ_w. Thus, a better way to model the stator is by a smaller τ_w which is equal to $\tau_{ws} = \frac{\tau_t - \tau_{tp}}{2}$ which is illustrated in Fig. 3.12. This error occured since the saliency of the poles was not taken into account in the first place. Note that by also changing the width of the current sheets, the surface current density has to be corrected by a factor $\frac{\tau_w}{\tau_{ws}}$. The field solutions are now obtained by replacing τ_w by τ_{ws}

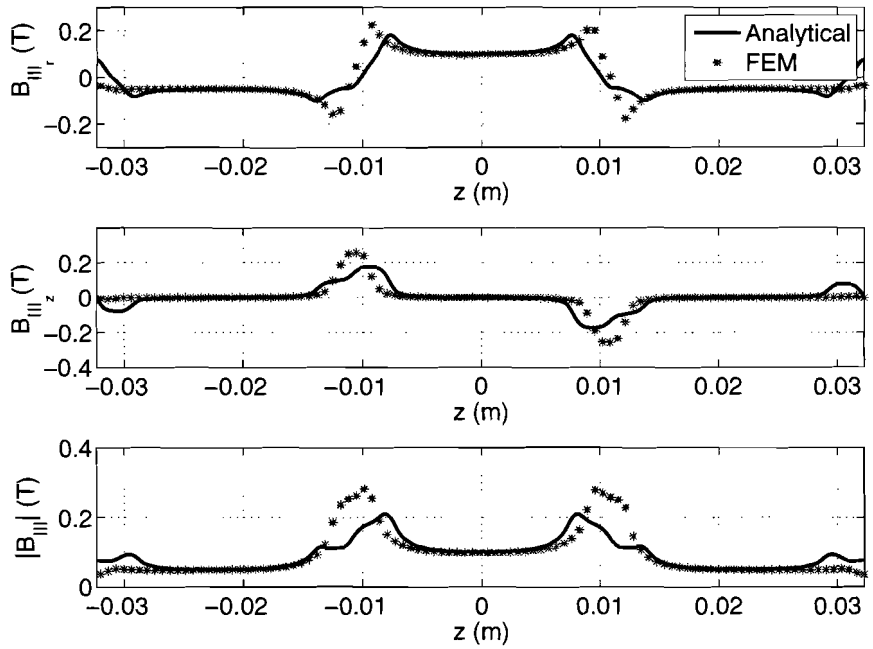

Fig. 3.11: Magnetic flux density in the air gap of the stator currrents for $\Delta_z = 0$

and plotted in Fig. 3.13 for $J_0 = 7.5\text{A/mm}^2$ and $\Delta_z = 0$. Now an acceptable agreement has been found between the semi-analytical solution and the FE solution. Altough there is a large error at the sides which is at the position of coils $A+$ and $C-$ which have a current density of -3.75 A/mm^2 and 3.75 A/mm^2, respectively. This is an abrupt change in sign of the current density, which is also visible in the change of the axial component of the semi-analytical field solution, B_{III_z}. However, this abrupt changement is almost not visible in the FE solution, because the coils are actually situated inside the stator. Since the currents are equal but opposite, there is only a local magnetic field but further away, in the air gap for example, no field is existing due these stator currents. Thus, this is an error which is introduced by the current sheet model as illustrated in Fig. 3.14.

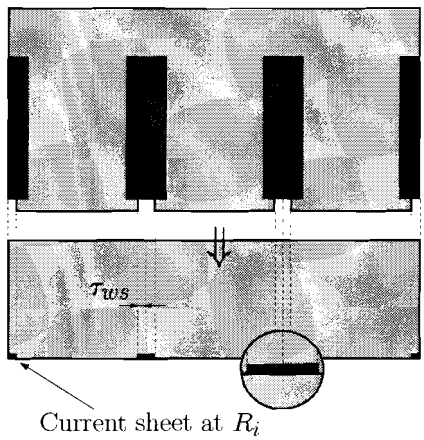

Fig. 3.12: Adapted stator modelling for calculation of the magnetic field in the air gap due to the stator currents.

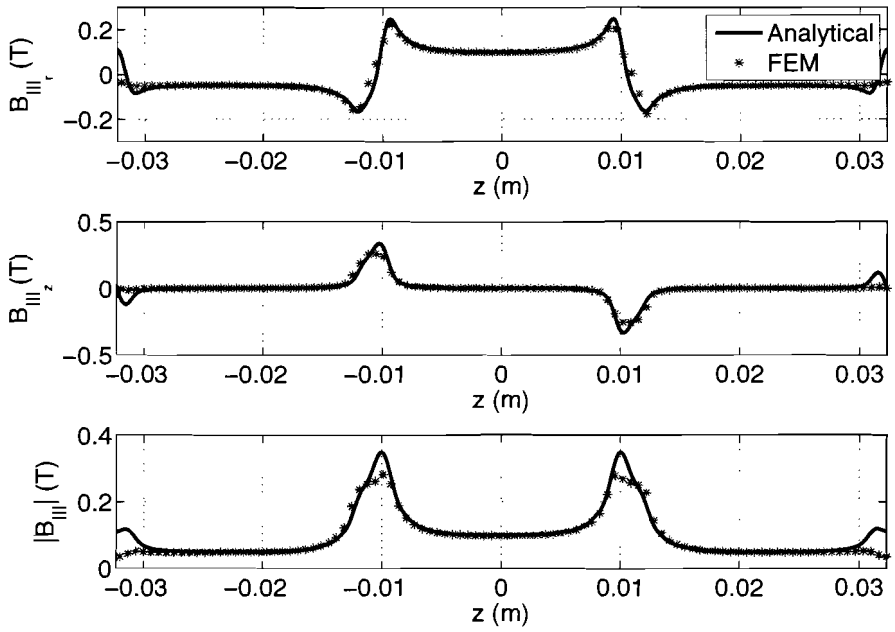

Fig. 3.13: Flux density of the coils in the air gap for $\Delta_z = 0$

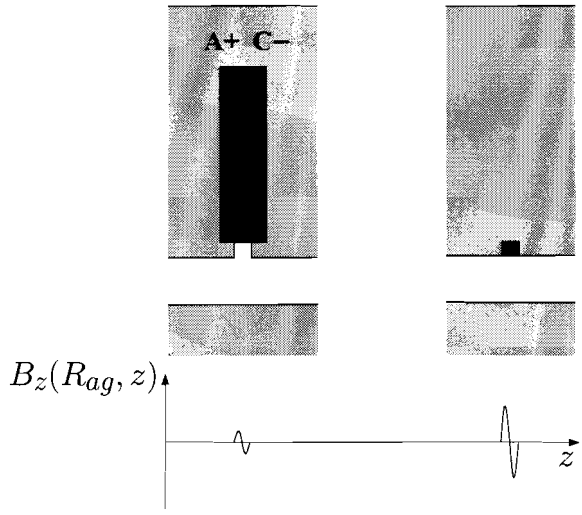

Fig. 3.14: Illustration of the error in the magnetic field solution of the stator currents due to the current sheet modelling.

3.4 Total field solution

The total field distribution in the air gap is accomplished by superposition of the field distribution due to the magnets and stator currents.

$$\mathbf{B}_{ag} = \mathbf{B}_{\mathrm{I}} + \mathbf{B}_{\mathrm{III}} \tag{3.107}$$

$$\Downarrow$$

$$B_{ag_r} = B_{\mathrm{I}_r} + B_{\mathrm{III}_{r_A}} + B_{\mathrm{III}_{r_B}} + B_{\mathrm{III}_{r_C}}, \tag{3.108}$$

$$B_{ag_z} = B_{\mathrm{I}_z} + B_{\mathrm{III}_{z_A}} + B_{\mathrm{III}_{z_B}} + B_{\mathrm{III}_{z_C}}, \tag{3.109}$$

$$B_{ag} = \sqrt{B_{ag_r}^2 + B_{ag_z}^2}, \tag{3.110}$$

where $B_{\mathrm{I}_z} = B_{\mathrm{I}_{z'}}(r, z' + \Delta_z)$. In Fig. 3.15 the total semi-analytical field solution together with the FE calculation is shown. The errors are mainly due to the slotting effect and current sheet modelling as discussed in previous Sections.

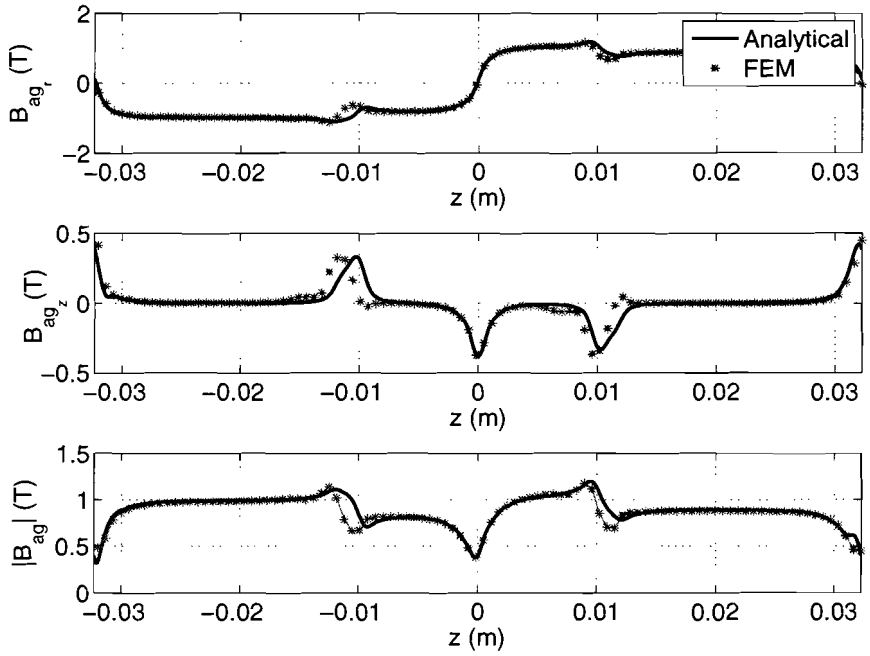

Fig. 3.15: Total flux density in the air gap for $\Delta_z = 0$

3.5 Force calculation

Now that the total description of the magnetic field in the air gap is given, the force can be calculated. There are many ways of calculating the electromagnetic force, by means of the Lorentz equation, the energy method or with the Maxwell stress tensor. The Lorentz equation holds for current carying wires in a magnetic field. This approach could be used in this case but later on end effects and slotting effects will be modelled. These effects exist without the presence of current and therefore, the Lorentz equation cannot be used. The energy method works under the assumption that the current is constant, or the flux is constant, which is never the case. This method is the most useful when time discretion is considered, and is therefore used in FE calculations. The force calculation by means of the Maxwell stress tensor is the most general one, since it is always valid. Therefore, this method will be used in our force calculation, and it is given by

$$\mathbf{F} = \frac{1}{\mu_0} \oint_S \mathbb{T}.\mathbf{n} dS, \tag{3.111}$$

where S is the closed surface surrounding the object on which the force is calculated and the tensor $\mathbb{T}$ is given by

$$\mathbb{T} = \begin{bmatrix} B_r^2 - \frac{|B|^2}{2} & B_r B_\theta & B_r B_z \\ B_\theta B_r & B_\theta^2 - \frac{|B|^2}{2} & B_\theta B_z \\ B_z B_r & B_z B_\theta & B_z^2 - \frac{|B|^2}{2} \end{bmatrix}. \tag{3.112}$$

Normally, the closed surface, S, should surround the total translator, but since end effects are neglected and only one pole-pair of the total geometry is modelled, S only has to surround one pole pair of the translator. The total force is then obtained by multiplication with the number of pole-pairs, N_p. The closed surface, S, is defined by the three surfaces given by

$$\begin{aligned} S_1: &\quad r = R_{ag} &&\text{for } -\tau_p \leq z \leq \tau_p, \\ S_2: &\quad z = -\tau_p &&\text{for } 0 \leq r \leq R_{ag}, \\ S_3: &\quad z = \tau_p &&\text{for } 0 \leq r \leq R_{ag}, \end{aligned} \tag{3.113}$$

with their normal vectors given by

$$\begin{aligned} \mathbf{n}_1 &= \mathbf{e}_r, \\ \mathbf{n}_2 &= -\mathbf{e}_z, \\ \mathbf{n}_3 &= \mathbf{e}_z. \end{aligned} \tag{3.114}$$

But since the field solution at S_2 is equal to S_3 due to the periodical boundary conditions, and the normal vector of both surfaces are in opposite direction, evaluation of (3.111) on both surfaces results in zero. Therefore, only surface S_1 has to be considered, and dS is then given by $2\pi R_{ag} dz$. The total force is then calculated by multiplication with the

number of pole-pairs, N_p. Evaluation of (3.111) gives

$$\begin{bmatrix} F_r \\ F_\theta \\ F_z \end{bmatrix} = \frac{2\pi R_{ag} N_p}{\mu_0} \int_{-\tau_p}^{\tau_p} \begin{bmatrix} B_r^2 - \frac{|B|^2}{2} & B_r B_\theta & B_r B_z \\ B_\theta B_r & B_\theta^2 - \frac{|B|^2}{2} & B_\theta B_z \\ B_z B_r & B_z B_\theta & B_z^2 - \frac{|B|^2}{2} \end{bmatrix} \cdot \begin{bmatrix} \mathbf{e}_r \\ 0 \\ 0 \end{bmatrix} dz \Bigg|_{r=R_{ag}},$$

$$\Downarrow$$

$$F_r = \frac{2\pi R_{ag} N_p}{\mu_0} \int_{-\tau_p}^{\tau_p} B_r^2 - \frac{|B|^2}{2} dz \Bigg|_{r=R_{ag}}, \tag{3.115}$$

$$F_\theta = \frac{2\pi R_{ag} N_p}{\mu_0} \int_{-\tau_p}^{\tau_p} B_\theta B_r dz \Bigg|_{r=R_{ag}}, \tag{3.116}$$

$$F_z = \frac{2\pi R_{ag} N_p}{\mu_0} \int_{-\tau_p}^{\tau_p} B_z B_r dz \Bigg|_{r=R_{ag}}. \tag{3.117}$$

Equation (3.115) gives us the radial strain, which is sometimes useful when bearings have to be designed, but it will not be considered here. Equation (3.116) is zero, since B_θ is zero which is expected due to the axisymmetry. The most important one is the axial force given by (3.117). Altough this equation seems to be very simple, the evaluation is complex since both field components are superpositions of other field components. Since all the field equations are evaluated at $r = R_{ag}$, the field equations can be written as a constant times a sine or cosine function for every harmonic, which simplifies the formulation. Define

$$Q_{1n} = -\Big(a_{1n} \mathcal{B}_{\mathcal{I}1}(m_n R_{ag}) + b_{1n} \mathcal{B}_{\mathcal{K}1}(m_n R_{ag}) \Big), \tag{3.118}$$

$$Q_{2n} = -\Big(a_{1n} \mathcal{B}_{\mathcal{I}0}(m_n R_{ag}) - b_{1n} \mathcal{B}_{\mathcal{K}0}(m_n R_{ag}) \Big), \tag{3.119}$$

$$Q_{3n} = \frac{1}{(c_{4_n} c_{1_n} - c_{2_n} c_{3_n})} \Big\{ c_{4_n} \mathcal{B}_{\mathcal{I}1}(m_n R_{ag}) + c_{3_n} \mathcal{B}_{\mathcal{K}1}(m_n R_{ag}) \Big\}, \tag{3.120}$$

$$Q_{4n} = \frac{-1}{(c_{4_n} c_{1_n} - c_{2_n} c_{3_n})} \Big\{ c_{4_n} \mathcal{B}_{\mathcal{I}0}(m_n R_{ag}) - c_{3_n} \mathcal{B}_{\mathcal{K}0}(m_n R_{ag}) \Big\}, \tag{3.121}$$

then the field equations at $r = R_{ag}$ can be written as

$$B_{\mathrm{I}_r} = \sum_{n=1}^{\infty} Q_{1n} \sin\Big(m_n(z+\Delta_z)\Big), \tag{3.122}$$

$$B_{\mathrm{I}_z} = \sum_{n=1}^{\infty} Q_{2n} \cos\Big(m_n(z+\Delta_z)\Big), \tag{3.123}$$

$$B_{\mathrm{III}_{r_A}} = \mu_0 J_A \sum_{n=1}^{\infty} K_{w_n} Q_{3n} \cos\Big(m_n(z-\tau_t)\Big), \tag{3.124}$$

$$B_{\mathrm{III}_{z_A}} = \mu_0 J_A \sum_{n=1}^{\infty} K_{w_n} Q_{4n} \sin\Big(m_n(z-\tau_t)\Big), \tag{3.125}$$

$$B_{\mathrm{III}_{r_B}} = \mu_0 J_B \sum_{n=1}^{\infty} K_{w_n} Q_{3n} \cos\Big(m_n z\Big), \tag{3.126}$$

$$B_{\mathrm{III}_{z_B}} = \mu_0 J_B \sum_{n=1}^{\infty} K_{w_n} Q_{4n} \sin\Big(m_n z\Big), \tag{3.127}$$

$$B_{\mathrm{III}_{r_C}} = \mu_0 J_C \sum_{n=1}^{\infty} K_{w_n} Q_{3n} \cos\Big(m_n(z+\tau_t)\Big), \tag{3.128}$$

$$B_{\mathrm{III}_{z_C}} = \mu_0 J_C \sum_{n=1}^{\infty} K_{w_n} Q_{4n} \sin\Big(m_n(z+\tau_t)\Big). \tag{3.129}$$

During evaluation of (3.117), the trigonometric identities in Appendix A.2 are used, which gives

$$F_z = \frac{2\pi R_{ag} N_p}{\mu_0} \int_{-\tau_p}^{\tau_p} (B_{I_z} + B_{III_{z_A}} + B_{III_{z_B}} + B_{III_{z_C}})(B_{I_r} + B_{III_{r_A}} + B_{III_{r_B}} + B_{III_{r_C}})dz,$$

$$\Downarrow$$

$$\begin{aligned} F_z = {} & 2\pi R_{ag} N_p \tau_p \sum_{n=1}^{\infty} K_{w_n} \Bigg[\\ & + Q_1 Q_4 \Bigg\{ J_A \cos\Big(m_n(\Delta_z - \tau_t)\Big) + J_B \cos\Big(m_n \Delta_z\Big) + J_C \cos\Big(m_n(\Delta_z + \tau_t)\Big) \Bigg\} \\ & + Q_2 Q_3 \Bigg\{ J_A \cos\Big(m_n(\Delta_z - \tau_t)\Big) + J_B \cos\Big(m_n \Delta_z\Big) + J_C \cos\Big(m_n(\Delta_z + \tau_t)\Big) \Bigg\} \\ & + \mu_0 K_{w_n} Q_3 Q_4 \Bigg\{ J_A J_B \sin(m_n \tau_t) + J_A J_C \sin(2 m_n \tau_t) + J_B J_A \sin(-m_n \tau_t) \\ & + J_B J_C \sin(m_n \tau_t) + J_C J_A \sin(-2 m_n \tau_t) + J_C J_B \sin(-m_n \tau_t) \Bigg\} \Bigg], \end{aligned}$$

and since $\sin(\alpha) = -\sin(-\alpha)$ this simplifies to

$$F_z = 2\pi R_{ag} N_p \tau_p \sum_{n=1}^{\infty} \left[(Q_1 Q_4 + Q_2 Q_3) \left\{ J_A \cos\left(m_n(\Delta_z - \tau_t) \right) + J_B \cos\left(m_n \Delta_z \right) + J_C \cos\left(m_n(\Delta_z + \tau_t) \right) \right\} \right]. \tag{3.130}$$

If (3.118)-(3.121) are substituted, and simplification is performed, the equation of the force becomes

$$F_z = \pi R_{ag} L_{ax} \sum_{n=1}^{\infty} \left[K_{w_n} C_n \left\{ J_A \cos\left(m_n(\Delta_z - \tau_t) \right) + J_B \cos\left(m_n \Delta_z \right) + J_C \cos\left(m_n(\Delta_z + \tau_t) \right) \right\} \right], \tag{3.131}$$

with

$$C_n = \frac{b_{1n} c_{4n} - a_{1n} c_{3n}}{c_{4n} c_{1n} - c_{2n} c_{3n}} \left(\mathcal{B}_{I0}(m_n R_{ag}) \mathcal{B}_{K1}(m_n R_{ag}) + \mathcal{B}_{I1}(m_n R_{ag}) \mathcal{B}_{K0}(m_n R_{ag}) \right).$$

and $L_{ax} = 2N_p\tau_p$ the axial length of the stator. Now a simulation at constant speed is done and force is calculated as function of the position Δ_z for a distance of 360 electrical degrees (τ_{wp}). The amplitude of the current density is 7.5 A/mm^2 and the excitation is sinusoidal. In Fig. 3.16 the numerical solution together with the two different FE calculations is shown. One FE calculation is performed with the slotted stator and the other FE calculation is performed with the stator modelled as a current sheet, applying the same assumption as in the semi-analytical model. Again good agreement has been found between the semi-analytical solution and the FE solution. The discrepancy is mainly caused by the current sheet modelling which translates in a force error of the sixth and twelfth harmonic, the mean value is almost exactly calculated. The different harmonics of the force of the different models are given in Table 3.1.

Tab. 3.1: Amplitude of the harmonics of the force waveform for the different models.

Harmonic	Semi-analytical	FEM with slots	FEM with current sheets
0	1586	1585	1589
6	-173.6	-82	-129
12	-58	0.2	-17.3
18	-25	16.8	10.2

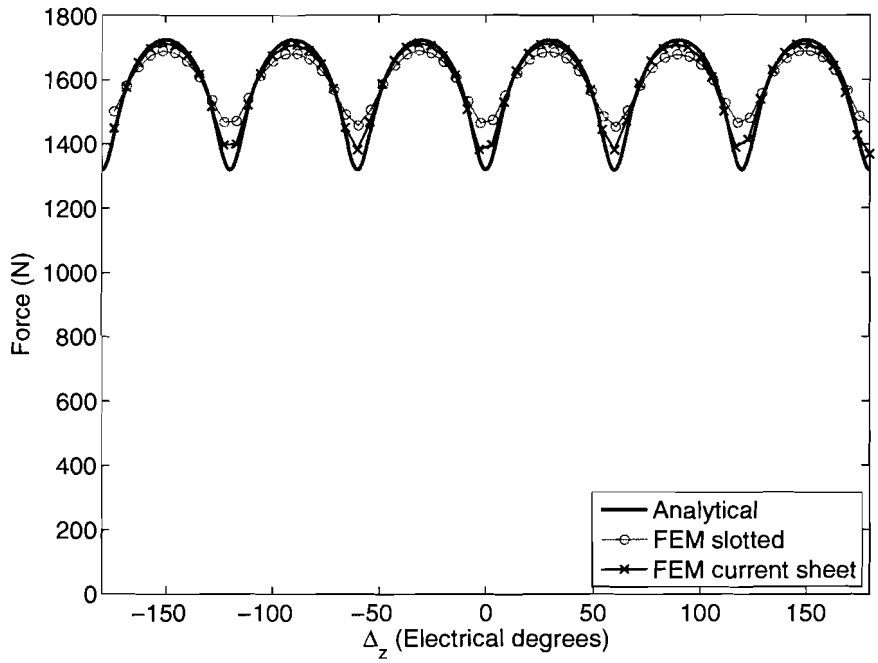

Fig. 3.16: Axial force for 360 electrical degrees with $J_0 = 7.5\text{A/mm}^2$ and sinusoidal excitation.

3.6 Inductance calculation

In order to model the dynamic behaviour of the machine, the self-inductances and mutual inductances for every phase must be known. The field distribution due to the stator coils is solved, thus the self inductance of a phase can be calculated as follows

$$L_{ph} = \frac{\Psi_{ph}}{I_{ph}}, \tag{3.132}$$

where Ψ_{ph} is the flux linkage due to the stator currents of the considered phase, which is approximatly the amount of radial flux passing through the tooth of the considered phase. This flux linkage is therefore given by

$$\begin{aligned}
\Psi_A &= NN_{sp}\int_{S_{slot_A}} B_{\mathrm{III}_{r_A}}(r,z)dS, \\
\Psi_B &= NN_{sp}\int_{S_{slot_B}} B_{\mathrm{III}_{r_B}}(r,z)dS, \\
\Psi_C &= NN_{sp}\int_{S_{slot_C}} B_{\mathrm{III}_{r_C}}(r,z)dS,
\end{aligned} \tag{3.133}$$

where S_{slot} is the area of the slot at the inner radius of the stator and therefore $dS = 2\pi R_i dz$, which gives

$$\begin{aligned}
\Psi_A &= 2\pi R_i NN_{sp}\int_{\frac{\tau_t}{2}}^{\frac{3\tau_t}{2}} B_{\mathrm{III}_{r_A}}(R_i,z)dz, \\
\Psi_B &= 2\pi R_i NN_{sp}\int_{\frac{-\tau_t}{2}}^{\frac{\tau_t}{2}} B_{\mathrm{III}_{r_B}}(R_i,z)dz, \\
\Psi_C &= 2\pi R_i NN_{sp}\int_{\frac{-3\tau_t}{2}}^{\frac{-\tau_t}{2}} B_{\mathrm{III}_{r_C}}(R_i,z)dz,
\end{aligned} \tag{3.134}$$

and filling in the expressions for $B_{\mathrm{III}_{r_A}}$, $B_{\mathrm{III}_{r_B}}$, and $B_{\mathrm{III}_{r_C}}$ gives

$$\begin{aligned}
\Psi_A &= 2\pi R_i NN_{sp}\int_{\frac{\tau_t}{2}}^{\frac{3\tau_t}{2}} \mu_0 J_A \sum_{n=1}^{\infty} \frac{K_{w_n}}{(c_{4_n}c_{1_n} - c_{2_n}c_{3_n})} \\
&\quad \left\{ c_{4_n}\mathcal{B}_{\mathcal{I}1}(m_n R_i) + c_{3_n}\mathcal{B}_{\mathcal{K}1}(m_n R_i) \right\} \cos\Big(m_n\big(z - \tau_t\big) \Big) dz, \\
\Psi_B &= 2\pi R_i NN_{sp}\int_{\frac{-\tau_t}{2}}^{\frac{\tau_t}{2}} \mu_0 J_B \sum_{n=1}^{\infty} \frac{K_{w_n}}{(c_{4_n}c_{1_n} - c_{2_n}c_{3_n})} \\
&\quad \left\{ c_{4_n}\mathcal{B}_{\mathcal{I}1}(m_n R_i) + c_{3_n}\mathcal{B}_{\mathcal{K}1}(m_n R_i) \right\} \cos\Big(m_n z \Big) dz, \\
\Psi_C &= 2\pi R_i NN_{sp}\int_{\frac{-3\tau_t}{2}}^{\frac{-\tau_t}{2}} \mu_0 J_C \sum_{n=1}^{\infty} \frac{K_{w_n}}{(c_{4_n}c_{1_n} - c_{2_n}c_{3_n})} \\
&\quad \left\{ c_{4_n}\mathcal{B}_{\mathcal{I}1}(m_n R_i) + c_{3_n}\mathcal{B}_{\mathcal{K}1}(m_n R_i) \right\} \cos\Big(m_n\big(z + \tau_t\big) \Big) dz,
\end{aligned} \tag{3.135}$$

and since the expression should hold for every n, the integral and summation may be switched which gives

$$\begin{aligned}
\Psi_A &= 2\pi R_i N N_{sp} \mu_0 J_A \sum_{n=1}^{\infty} \frac{K_{w_n}}{(c_{4_n} c_{1_n} - c_{2_n} c_{3_n})} \\
&\quad \left\{ c_{4_n} \mathcal{B}_{\mathcal{I}1}(m_n R_i) + c_{3_n} \mathcal{B}_{\mathcal{K}1}(m_n R_i) \right\} \int_{\frac{\tau_t}{2}}^{\frac{3\tau_t}{2}} \cos\left(m_n \big(z - \tau_t\big) \right) dz, \\
\Psi_B &= 2\pi R_i N N_{sp} \mu_0 J_B \sum_{n=1}^{\infty} \frac{K_{w_n}}{(c_{4_n} c_{1_n} - c_{2_n} c_{3_n})} \\
&\quad \left\{ c_{4_n} \mathcal{B}_{\mathcal{I}1}(m_n R_i) + c_{3_n} \mathcal{B}_{\mathcal{K}1}(m_n R_i) \right\} \int_{\frac{-\tau_t}{2}}^{\frac{\tau_t}{2}} \cos\left(m_n z \right) dz, \\
\Psi_C &= 2\pi R_i N N_{sp} \mu_0 J_C \sum_{n=1}^{\infty} \frac{K_{w_n}}{(c_{4_n} c_{1_n} - c_{2_n} c_{3_n})} \\
&\quad \left\{ c_{4_n} \mathcal{B}_{\mathcal{I}1}(m_n R_i) + c_{3_n} \mathcal{B}_{\mathcal{K}1}(m_n R_i) \right\} \int_{\frac{-3\tau_t}{2}}^{\frac{-\tau_t}{2}} \cos\left(m_n \big(z + \tau_t\big) \right) dz. \qquad (3.136)
\end{aligned}$$

Evaluation of the integral results in

$$\begin{aligned}
\Psi_A &= 4\pi R_i N N_{sp} \mu_0 J_A \sum_{n=1}^{\infty} \frac{K_{w_n}}{m_n (c_{4n} c_{1n} - c_{2n} c_{3n})} \\
&\quad \left\{ c_{4_n} \mathcal{B}_{\mathcal{I}1}(m_n R_i) + c_{3_n} \mathcal{B}_{\mathcal{K}1}(m_n R_i) \right\} \sin\left(\frac{n\pi}{3} \right), \\
\Psi_B &= 4\pi R_i N N_{sp} \mu_0 J_B \sum_{n=1}^{\infty} \frac{K_{w_n}}{m_n (c_{4n} c_{1n} - c_{2n} c_{3n})} \\
&\quad \left\{ c_{4_n} \mathcal{B}_{\mathcal{I}1}(m_n R_i) + c_{3_n} \mathcal{B}_{\mathcal{K}1}(m_n R_i) \right\} \sin\left(\frac{n\pi}{3} \right), \\
\Psi_C &= 4\pi R_i N N_{sp} \mu_0 J_C \sum_{n=1}^{\infty} \frac{K_{w_n}}{m_n (c_{4n} c_{1n} - c_{2n} c_{3n})} \\
&\quad \left\{ c_{4_n} \mathcal{B}_{\mathcal{I}1}(m_n R_i) + c_{3_n} \mathcal{B}_{\mathcal{K}1}(m_n R_i) \right\} \sin\left(\frac{n\pi}{3} \right). \qquad (3.137)
\end{aligned}$$

It can be observed that the formulas are identical for all the three phases which is as expected since end effects are excluded.

The surface current densities can be written in function of the phase currents, I_{ph}.

$$J_{ph} = \frac{N I_{ph}}{\tau_{ws}}, \qquad (3.138)$$

and applying (3.132) gives the inductances

$$\begin{aligned}
L_{ph} &= \frac{4\pi R_i N^2 N_{sp} \mu_0}{\tau_{ws}} \sum_{n=1}^{\infty} \frac{K_{w_n}}{m_n (c_{4n} c_{1n} - c_{2n} c_{3n})} \\
&\quad \left\{ c_{4_n} \mathcal{B}_{\mathcal{I}1}(m_n R_i) + c_{3_n} \mathcal{B}_{\mathcal{K}1}(m_n R_i) \right\} \sin\left(\frac{n\pi}{3} \right). \qquad (3.139)
\end{aligned}$$

The same derivation can be done for calculation of the mutual inductances

$$M_{ph_i,ph_j} = \frac{\Psi_{ph_i,ph_j}}{I_{ph_j}}, \tag{3.140}$$

where Ψ_{ph_i,ph_j} is the flux linkage of phase i due to a current of phase j. Since again end effect are neglected, the assumption is made that $M_{ph_i,ph_j} = M_{ph_j,ph_i}$, the flux linkages are given by

$$\begin{aligned}
\Psi_{A,B} &= 2\pi R_i N N_{sp} \int_{\frac{\tau_t}{2}}^{\frac{3\tau_t}{2}} B_{\mathrm{III}_{r_B}}(R_i, z)dz, \\
\Psi_{B,C} &= 2\pi R_i N N_{sp} \int_{\frac{-\tau_t}{2}}^{\frac{\tau_t}{2}} B_{\mathrm{III}_{r_C}}(R_i, z)dz, \\
\Psi_{C,A} &= 2\pi R_i N N_{sp} \int_{\frac{-3\tau_t}{2}}^{\frac{-\tau_t}{2}} B_{\mathrm{III}_{r_A}}(R_i, z)dz,
\end{aligned} \tag{3.141}$$

and after filling in the expressions for $B_{\mathrm{III}_{r_A}}$, $B_{\mathrm{III}_{r_B}}$, and $B_{\mathrm{III}_{r_C}}$, the equations become

$$\begin{aligned}
\Psi_{A,B} &= 2\pi R_i N N_{sp} \int_{\frac{\tau_t}{2}}^{\frac{3\tau_t}{2}} \mu_0 J_B \sum_{n=1}^{\infty} \frac{K_{w_n}}{(c_{4_n} c_{1_n} - c_{2_n} c_{3_n})} \\
&\quad \left\{ c_{4_n} \mathcal{B}_{\mathcal{I}1}(m_n R_i) + c_{3_n} \mathcal{B}_{\mathcal{K}1}(m_n R_i) \right\} \cos\left(m_n z \right) dz, \\
\Psi_{B,C} &= 2\pi R_i N N_{sp} \int_{\frac{-\tau_t}{2}}^{\frac{\tau_t}{2}} \mu_0 J_C \sum_{n=1}^{\infty} \frac{K_{w_n}}{(c_{4_n} c_{1_n} - c_{2_n} c_{3_n})} \\
&\quad \left\{ c_{4_n} \mathcal{B}_{\mathcal{I}1}(m_n R_i) + c_{3_n} \mathcal{B}_{\mathcal{K}1}(m_n R_i) \right\} \cos\left(m_n \left(z + \tau_t \right) \right) dz, \\
\Psi_{C,A} &= 2\pi R_i N N_{sp} \int_{\frac{-3\tau_t}{2}}^{\frac{-\tau_t}{2}} \mu_0 J_A \sum_{n=1}^{\infty} \frac{K_{w_n}}{(c_{4_n} c_{1_n} - c_{2_n} c_{3_n})} \\
&\quad \left\{ c_{4_n} \mathcal{B}_{\mathcal{I}1}(m_n R_i) + c_{3_n} \mathcal{B}_{\mathcal{K}1}(m_n R_i) \right\} \cos\left(m_n \left(z - \tau_t \right) \right) dz,
\end{aligned} \tag{3.142}$$

and after switching the integral and summation the expressions become

$$\begin{aligned}
\Psi_{A,B} &= 2\pi R_i N N_{sp} \mu_0 J_B \sum_{n=1}^{\infty} \frac{K_{w_n}}{(c_{4_n} c_{1_n} - c_{2_n} c_{3_n})} \\
&\quad \left\{ c_{4_n} \mathcal{B}_{\mathcal{I}1}(m_n R_i) + c_{3_n} \mathcal{B}_{\mathcal{K}1}(m_n R_i) \right\} \int_{\frac{\tau_t}{2}}^{\frac{3\tau_t}{2}} \cos\left(m_n z\right) dz, \\
\Psi_{B,C} &= 2\pi R_i N N_{sp} \mu_0 J_C \sum_{n=1}^{\infty} \frac{K_{w_n}}{(c_{4_n} c_{1_n} - c_{2_n} c_{3_n})} \\
&\quad \left\{ c_{4_n} \mathcal{B}_{\mathcal{I}1}(m_n R_i) + c_{3_n} \mathcal{B}_{\mathcal{K}1}(m_n R_i) \right\} \int_{\frac{-\tau_t}{2}}^{\frac{\tau_t}{2}} \cos\left(m_n (z + \tau_t)\right) dz, \\
\Psi_{C,A} &= 2\pi R_i N N_{sp} \mu_0 J_A \sum_{n=1}^{\infty} \frac{K_{w_n}}{(c_{4_n} c_{1_n} - c_{2_n} c_{3_n})} \\
&\quad \left\{ c_{4_n} \mathcal{B}_{\mathcal{I}1}(m_n R_i) + c_{3_n} \mathcal{B}_{\mathcal{K}1}(m_n R_i) \right\} \int_{\frac{-3\tau_t}{2}}^{\frac{-\tau_t}{2}} \cos\left(m_n (z - \tau_t)\right) dz. \qquad (3.143)
\end{aligned}$$

Evaluating the integral gives

$$\begin{aligned}
\Psi_{A,B} &= 2\pi R_i N N_{sp} \mu_0 J_B \sum_{n=1}^{\infty} \frac{K_{w_n}}{m_n (c_{4n} c_{1n} - c_{2n} c_{3n})} \\
&\quad \left\{ c_{4_n} \mathcal{B}_{\mathcal{I}1}(m_n R_i) + c_{3_n} \mathcal{B}_{\mathcal{K}1}(m_n R_i) \right\} \sin\left(\frac{n\pi}{3}\right), \\
\Psi_{B,C} &= 2\pi R_i N N_{sp} \mu_0 J_C \sum_{n=1}^{\infty} \frac{K_{w_n}}{m_n (c_{4n} c_{1n} - c_{2n} c_{3n})} \\
&\quad \left\{ c_{4_n} \mathcal{B}_{\mathcal{I}1}(m_n R_i) + c_{3_n} \mathcal{B}_{\mathcal{K}1}(m_n R_i) \right\} \sin\left(\frac{n\pi}{3}\right), \\
\Psi_{C,A} &= 2\pi R_i N N_{sp} \mu_0 J_A \sum_{n=1}^{\infty} \frac{K_{w_n}}{m_n (c_{4n} c_{1n} - c_{2n} c_{3n})} \\
&\quad \left\{ c_{4_n} \mathcal{B}_{\mathcal{I}1}(m_n R_i) + c_{3_n} \mathcal{B}_{\mathcal{K}1}(m_n R_i) \right\} \sin\left(\frac{n\pi}{3}\right) \qquad (3.144)
\end{aligned}$$

and applying equation (3.140) and (3.138) the mutual inductance can be expressed as

$$\begin{aligned}
M_{ph_i, ph_j} &= \frac{2\pi R_i N^2 N_{sp} \mu_0}{\tau_{ws}} \sum_{n=1}^{\infty} \frac{K_{w_n}}{m_n (c_{4n} c_{1n} - c_{2n} c_{3n})} \\
&\quad \left\{ c_{4_n} \mathcal{B}_{\mathcal{I}1}(m_n R_i) + c_{3_n} \mathcal{B}_{\mathcal{K}1}(m_n R_i) \right\} \sin\left(\frac{n\pi}{3}\right), \qquad (3.145)
\end{aligned}$$

which is again the same for every phase as expected and equal to $\frac{L_{ph}}{2}$. Finally the inductances per winding, $N = 1$, can be calculated and the results are

$$M = \begin{bmatrix} L_a & M_{ab} & M_{ac} \\ M_{ba} & L_b & M_{bc} \\ M_{ca} & M_{cb} & L_c \end{bmatrix} = \begin{bmatrix} 4.14\mu\text{H} & 2.07\mu\text{H} & 2.07\mu\text{H} \\ 2.07\mu\text{H} & 4.14\mu\text{H} & 2.07\mu\text{H} \\ 2.07\mu\text{H} & 2.07\mu\text{H} & 4.14\mu\text{H} \end{bmatrix}.$$

The inductances can also be calculated with the FE software and those are given by

$$M = \begin{bmatrix} L_a & M_{ab} & M_{ac} \\ M_{ba} & L_b & M_{bc} \\ M_{ca} & M_{cb} & L_c \end{bmatrix} = \begin{bmatrix} 10.38\mu\text{H} & 5.23\mu\text{H} & 4.52\mu\text{H} \\ 5.23\mu\text{H} & 11.02\mu\text{H} & 5.23\mu\text{H} \\ 4.52\mu\text{H} & 5.23\mu\text{H} & 10.38\mu\text{H} \end{bmatrix}.$$

It can be observed that in the FE calculation the self inductances are not equal due to the inclusion of the end effects, the same holds for the mutual inductances. However the values are a factor 2.5 times higher then the semi-analytical solution. Due to the time lag, this discrepancy is not investigated, but is a future research topic.

4. SKEWING

A skewed topology offers the benefit of reducing the large cogging force in the tubular actuator, [11]. Further, the force ripple due to the winding distribution and harmonics of the magnetic field can be reduced. By skewing the magnets or the stator slots, the variation of the flux linkage during movement is much smoother, giving a more sinusoidal waveform, hence less force ripples. There are a variety of skewing possibilities, each with their own practical advantages and disadvantages. A semi-analytical description of the EMF- and force waveforms for different skewing topologies can give insight into which skewing topology is the optimal one given the performance specifications.

Skewed finite element models need a lot of computation time and the current software packages can only handle a linear skewing topology. When a skewed topology is modelled with FE software, the total structure is divided into angular layers which are shifted in axial direction. As mentioned before, these layers can only be shifted in a linear way. In order to check the semi-analytical model for nonlinear skewing topologies, a MATLAB® script is written which uses the unskewed FE results and calculates the skewed results based upon a shift and add method, [11]. It is basically the same as how the FE software handles the results but now also nonlinear skewing topologies can be calculated, and can be expressed in a formula as

$$e_{\text{sk}}(\Delta_z) = \frac{1}{N_\theta} \sum_{n=1}^{N_\theta} e_{\text{unsk}}\left(\Delta_z + \mathcal{S}\left(\frac{n2\pi}{N_\theta}\right)\right), \tag{4.1}$$

where e_{sk} is the skewed EMF waveform, e_{unsk} is the unskewed EMF waveform, N_θ the number of angular layers and $\mathcal{S}$ is the skewing transformation which differs for every skewing topology and will defined in the next section. This is exactly how the FLUX software, [20], internally calculates linear skewing applied to rotary machines.

In the previous Chapter, the field equations in the air gap and the magnets were derived in an axisymmetric coordinate system. It means that the derived field equations have a two-dimensional discription. For force and EMF calculation the abstraction is made by considering only the magnetic fields in the center of the air gap, R_{ag}, and the inner radius of the stator, R_i, respectively. This abstraction reduced the field equations to a one-dimensional discription. A skewed topology does not have axisymmetry anymore and therefore, the field discriptions should be three-dimensional, but due to the abstraction of considering a constant radius for calculation of force and EMF this description only has to be two-dimensional.

In this Chapter, semi-analytical equations for the force and EMF waveforms for different skewed topologies will be derived. These descriptions make use of the results in Chapter 3, together with a skewing transformation. First the use of this skewing transformation is given and afterwards the EMF and force waveforms are calculated for both stator and translator skewing. In the last section a comparative study is done for different skewing

topologies in order to find the skewing topology which gives the lowest force ripple with a minimal reduction of the mean force.

4.1 Skew transformation

In Fig. 4.1 a skewing transformation is shown. The left drawing is a cylindrical magnet array with a given radius where the magnets are magnetised in positive and negative radial direction alternatively (denoted as colors), and at a given radius the magnetic field is only dependent on z. In the right drawing, a linear skewing transformation is applied

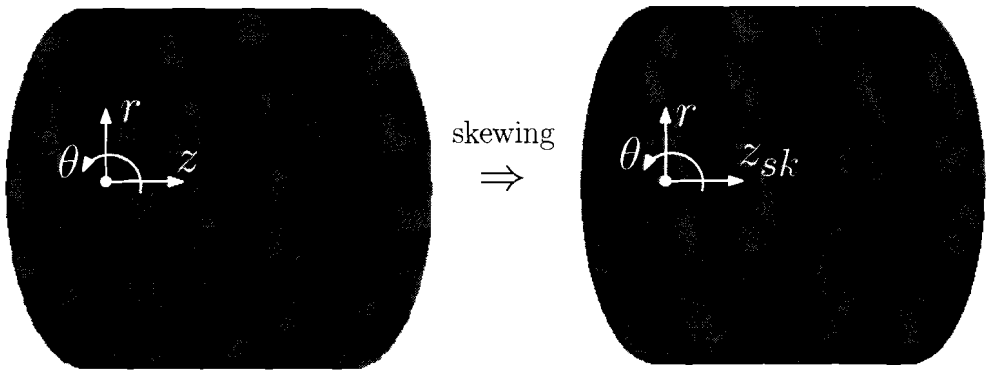

Fig. 4.1: Skew transformation

and the magnetic field at a given radius becomes also dependent on θ. If both topologies could be linked by some transformation function then the field equations of Chapter 3 could be transformed to field equations which hold for a skewed topology. Skewing can be regarded as a shift of the z-axis which is dependent on θ. Therefore, define the skewing transformation $\mathcal{S}$ as follows

$$z_{sk} = z + \mathcal{S}(\theta) \text{ for stator skewing,} \tag{4.2}$$

$$z_{sk} = z' + \mathcal{S}(\theta) \text{ for translator skewing.} \tag{4.3}$$

Various skewing topologies exists, the ones discussed in [11] are given in Fig. 4.2.

The corresponding skewing transformations are

- Linear (a):
  $\mathcal{S}(\theta) = \frac{\Delta_s \theta}{2\pi}$,

- Triangular (b), (c):
  $$\mathcal{S}(\theta) = \begin{cases} \frac{p\Delta_s\theta}{\pi} - kp\Delta_s & \frac{k2\pi}{p} < \theta < \frac{(2k+1)\pi}{p} \\ \frac{-p\Delta_s\theta}{\pi} + (k+1)p\Delta_s & \frac{(k+1)\pi}{p} < \theta < \frac{2(k+1)\pi}{p} \end{cases} \text{ for } k = 0...(p-1),$$

- Sinusoidal (d), (f):
  $\mathcal{S}(\theta) = \Delta_s \sin(p\theta)$,

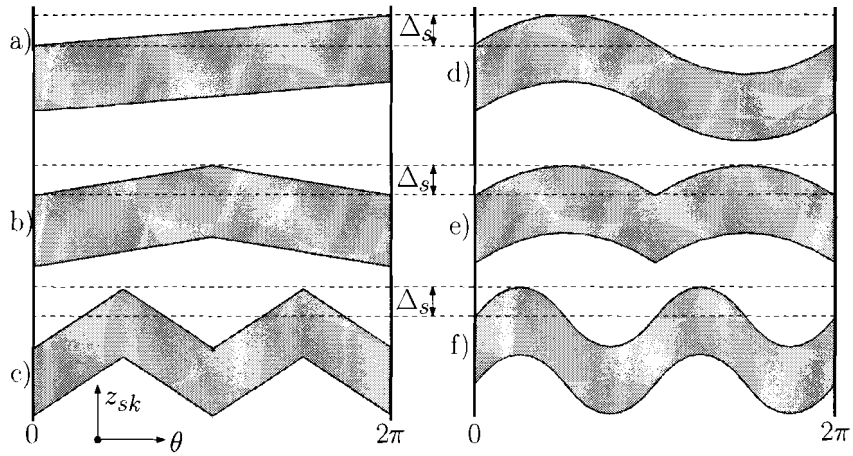

Fig. 4.2: Possible skewing topologies. The skewing amplitude is indicated by Δ_s.

- Half Sinusoidal (e):
  $\mathcal{S}(\theta) = \Delta_s |\sin(p\theta)|$.

In this respect can the field equations of Chapter 2 be transformed, replacing z or z' with $z + \mathcal{S}(\theta)$ or $z' + \mathcal{S}(\theta)$.

The distinction has to be made if stator or translator skewing is considered. Both have the same influence on the EMF form but the total axial force will be different. Also stator skewing introduces an angular force, trying to rotate the translator, however this angular force can be eliminated by choosing a skewing transformation which has a periodicity of 180° like (c),(e) or (f). Due to leakage, translator skewing can also give a rotational force, however significantly less. Translator skewing has a disadvantage regarding the construction of the magnets whereas stator skewing can give rise to winding problems if sharp corners exists.

4.2 EMF calculation

The EMF waveform resulting from a skewed topology is invariant of the choice of stator or translator skewing. This can be shown mathematically. For calculation of the EMF waveform, the flux linkage imposed by every phase should be calculated. Again the flux linkage is assumed to be the amount of radial flux density of the magnets at the stator bore, R_i, at the tooth of the phase that is considered, given by

$$\begin{aligned}
\Psi_A &= NN_{sp} \int_{S_{slot_A}} B_{\mathrm{I}_r} dS, \\
\Psi_B &= NN_{sp} \int_{S_{slot_B}} B_{\mathrm{I}_r} dS, \\
\Psi_C &= NN_{sp} \int_{S_{slot_C}} B_{\mathrm{I}_r} dS.
\end{aligned} \tag{4.4}$$

In the case of stator skewing, S_{slot} is the skewed area of the slots, and thus dependent on θ, furthermore $dS = R_i dz d\theta$ since $dz_{sk} = dz$ and everything is evaluated at $r = R_i$, which gives in case of stator skewing

$$\begin{aligned}
\Psi_A &= R_i N N_{sp} \int_0^{2\pi} \int_{\frac{\tau_t}{2}+\mathcal{S}}^{\frac{3\tau_t}{2}+\mathcal{S}} B_{\mathrm{I}_r}(R_i, z') dz d\theta, \\
\Psi_B &= R_i N N_{sp} \int_0^{2\pi} \int_{-\frac{\tau_t}{2}+\mathcal{S}}^{\frac{\tau_t}{2}+\mathcal{S}} B_{\mathrm{I}_r}(R_i, z') dz d\theta, \\
\Psi_C &= R_i N N_{sp} \int_0^{2\pi} \int_{-\frac{3\tau_t}{2}+\mathcal{S}}^{-\frac{\tau_t}{2}+\mathcal{S}} B_{\mathrm{I}_r}(R_i, z') dz d\theta.
\end{aligned} \tag{4.5}$$

In the case of translator skewing the EMF waveform is calculated by applying the skewing transformation to the magnetic field equations of the magnets, S_{slot} is now unskewed, but z' is replaced by z_{sk} which gives in case of translator skewing

$$\begin{aligned}
\Psi_A &= R_i N N_{sp} \int_0^{2\pi} \int_{\frac{\tau_t}{2}}^{\frac{3\tau_t}{2}} B_{\mathrm{I}_r}(R_i, z' + \mathcal{S}) dz d\theta, \\
\Psi_B &= R_i N N_{sp} \int_0^{2\pi} \int_{-\frac{\tau_t}{2}}^{\frac{\tau_t}{2}} B_{\mathrm{I}_r}(R_i, z' + \mathcal{S}) dz d\theta, \\
\Psi_C &= R_i N N_{sp} \int_0^{2\pi} \int_{-\frac{3\tau_t}{2}}^{-\frac{\tau_t}{2}} B_{\mathrm{I}_r}(R_i, z' + \mathcal{S}) dz d\theta.
\end{aligned} \tag{4.6}$$

After integration over z expressions (4.5) and (4.6) become the same which prooves that the EMF waveforms are equal for stator or translator skewing. Now the evaluation of (4.6) will be done but only for phase A since the equations for phase B and phase C are similar. This gives for the flux linkage of phase A

$$\begin{aligned}
\Psi_A &= -R_i N N_{sp} \int_0^{2\pi} \int_{\frac{\tau_t}{2}}^{\frac{3\tau_t}{2}} \sum_{n=1}^{\infty} \Big(a_{1n} \mathcal{B}_{\mathcal{I}1}(m_n R_i) + b_{1n} \mathcal{B}_{\mathcal{K}1}(m_n R_i) \Big) \\
&\quad \sin\Big(m_n (z' + \mathcal{S}) \Big) dz d\theta, \qquad (4.7) \\
&\Downarrow \\
\Psi_A &= -R_i N N_{sp} \sum_{n=1}^{\infty} \Big(a_{1n} \mathcal{B}_{\mathcal{I}1}(m_n R_i) + b_{1n} \mathcal{B}_{\mathcal{K}1}(m_n R_i) \Big) \\
&\quad \int_0^{2\pi} \int_{\frac{\tau_t}{2}}^{\frac{3\tau_t}{2}} \sin\Big(m_n (z - \Delta_z + \mathcal{S}) \Big) dz d\theta. \qquad (4.8)
\end{aligned}$$

Using (6.14), the expression becomes

$$\begin{aligned}
\Psi_A &= -R_i N N_{sp} \sum_{n=1}^{\infty} \Big(a_{1n} \mathcal{B}_{\mathcal{I}1}(m_n R_i) + b_{1n} \mathcal{B}_{\mathcal{K}1}(m_n R_i) \Big) \\
&\quad \int_0^{2\pi} \int_{\frac{\tau_t}{2}}^{\frac{3\tau_t}{2}} \sin\Big(m_n (z - \Delta_z) \Big) \cos(m_n \mathcal{S}) + \cos\Big(m_n (z - \Delta_z) \Big) \sin(m_n \mathcal{S}) dz d\theta.
\end{aligned} \tag{4.9}$$

Tab. 4.1: Coefficients T_{c_n} and T_{s_n} for different skewing topologies.

	T_{c_n}	T_{s_n}
Linear	$\frac{2\pi}{m_n\Delta_s}\sin(m_n\Delta_s)$	$\frac{2\pi}{m_n\Delta_s}\Big(1-\cos(m_n\Delta_s)\Big)$
Triangular	$\frac{2\pi}{m_n\Delta_s}\sin(m_n\Delta_s)$	0
Sinusoidal	$2\pi\mathcal{B}_{\mathcal{J}0}(m_n\Delta_s)$	0
Half sinusoidal	$2\pi\mathcal{B}_{\mathcal{J}0}(m_n\Delta_s)$	$2\int_0^{\pi}\sin\Big(m_n\Delta_s\sin(\theta)\Big)d\theta$

Because the variables are seperated, the double integral can be changed into a product of integrals

$$\begin{aligned}\Psi_A &= -R_iNN_{sp}\sum_{n=1}^{\infty}\Big(a_{1n}\mathcal{B}_{\mathcal{I}1}(m_nR_i)+b_{1n}\mathcal{B}_{\mathcal{K}1}(m_nR_i)\Big)\\ &\quad\Bigg\{\int_0^{2\pi}\cos(m_n\mathcal{S})d\theta\int_{\frac{\tau_t}{2}}^{\frac{3\tau_t}{2}}\sin\Big(m_n(z-\Delta_z)\Big)dz\\ &\quad+\int_0^{2\pi}\sin(m_n\mathcal{S})d\theta\int_{\frac{\tau_t}{2}}^{\frac{3\tau_t}{2}}\cos\Big(m_n(z-\Delta_z)\Big)dz\Bigg\}. \qquad (4.10)\end{aligned}$$

Now introduce two variables, T_{c_n} and T_{s_n}, which are given by

$$T_{c_n} = \int_0^{2\pi}\cos\Big(m_n\mathcal{S}(\theta)\Big)d\theta, \qquad (4.11)$$

$$T_{s_n} = \int_0^{2\pi}\sin\Big(m_n\mathcal{S}(\theta)\Big)d\theta. \qquad (4.12)$$

These integrals can be evaluated, if possible, for the different skewing topologies, the results are listed in Table 4.1. Note that after evaluation of the integrals, T_{c_n} and T_{s_n} become independent of the number of repetitions, p, therefore the number of repetitions does not influence the skewed EMF waveforms.

Finally the flux linkages are given by

$$
\begin{aligned}
\Psi_A &= -2\pi R_i N N_{sp} \sum_{n=1}^{\infty} \frac{1}{m_n} \Big(a_{1n} \mathcal{B}_{\mathcal{I}1}(m_n R_i) + b_{1n} \mathcal{B}_{\mathcal{K}1}(m_n R_i) \Big) \\
&\quad \Bigg[T_{c_n} \Big\{ \cos\Big(m_n (\frac{\tau_t}{2} - \Delta_z) \Big) - \cos\Big(m_n (\frac{3\tau_t}{2} - \Delta_z) \Big) \Big\} \\
&\quad + T_{s_n} \Big\{ \sin\Big(m_n (\frac{3\tau_t}{2} - \Delta_z) \Big) - \sin\Big(m_n (\frac{\tau_t}{2} - \Delta_z) \Big) \Big\} \Bigg], \\
\Psi_B &= -2\pi R_i N N_{sp} \sum_{n=1}^{\infty} \frac{1}{m_n} \Big(a_{1n} \mathcal{B}_{\mathcal{I}1}(m_n R_i) + b_{1n} \mathcal{B}_{\mathcal{K}1}(m_n R_i) \Big) \\
&\quad \Bigg[T_{c_n} \Big\{ \cos\Big(m_n (-\frac{\tau_t}{2} - \Delta_z) \Big) - \cos\Big(m_n (\frac{\tau_t}{2} - \Delta_z) \Big) \Big\} \\
&\quad + T_{s_n} \Big\{ \sin\Big(m_n (\frac{\tau_t}{2} - \Delta_z) \Big) - \sin\Big(m_n (-\frac{\tau_t}{2} - \Delta_z) \Big) \Big\} \Bigg], \\
\Psi_C &= -2\pi R_i N N_{sp} \sum_{n=1}^{\infty} \frac{1}{m_n} \Big(a_{1n} \mathcal{B}_{\mathcal{I}1}(m_n R_i) + b_{1n} \mathcal{B}_{\mathcal{K}1}(m_n R_i) \Big) \\
&\quad \Bigg[T_{c_n} \Big\{ \cos\Big(m_n (-\frac{3\tau_t}{2} - \Delta_z) \Big) - \cos\Big(m_n (-\frac{\tau_t}{2} - \Delta_z) \Big) \Big\} \\
&\quad + T_{s_n} \Big\{ \sin\Big(m_n (-\frac{\tau_t}{2} - \Delta_z) \Big) - \sin\Big(m_n (-\frac{3\tau_t}{2} - \Delta_z) \Big) \Big\} \Bigg], \qquad (4.13)
\end{aligned}
$$

which can be simplified using $\cos(\alpha - \beta) - \cos(-\alpha - \beta) = -2\sin(\alpha)\sin(\beta)$

$$
\begin{aligned}
\Psi_A &= -4\pi R_i N N_{sp} \sum_{n=1}^{\infty} \frac{1}{m_n} \Big(a_{1n} \mathcal{B}_{\mathcal{I}1}(m_n R_i) + b_{1n} \mathcal{B}_{\mathcal{K}1}(m_n R_i) \Big) \\
&\quad \sin\Big(\frac{n\pi}{3}\Big) \Big[T_{c_n} \sin\Big(m_n (\tau_t - \Delta_z) \Big) + T_{s_n} \cos\Big(m_n (\tau_t - \Delta_z) \Big) \Big], \\
\Psi_B &= -4\pi R_i N N_{sp} \sum_{n=1}^{\infty} \frac{1}{m_n} \Big(a_{1n} \mathcal{B}_{\mathcal{I}1}(m_n R_i) + b_{1n} \mathcal{B}_{\mathcal{K}1}(m_n R_i) \Big) \\
&\quad \sin\Big(\frac{n\pi}{3}\Big) \Big[- T_{c_n} \sin\Big(m_n \Delta_z \Big) + T_{s_n} \cos\Big(m_n \Delta_z \Big) \Big], \\
\Psi_C &= -4\pi R_i N N_{sp} \sum_{n=1}^{\infty} \frac{1}{m_n} \Big(a_{1n} \mathcal{B}_{\mathcal{I}1}(m_n R_i) + b_{1n} \mathcal{B}_{\mathcal{K}1}(m_n R_i) \Big) \\
&\quad \sin\Big(\frac{n\pi}{3}\Big) \Big[- T_{c_n} \sin\Big(m_n (\tau_t + \Delta_z) \Big) + T_{s_n} \cos\Big(m_n (\tau_t + \Delta_z) \Big) \Big], \qquad (4.14)
\end{aligned}
$$

and finally for the EMF waveforms, using (3.92)

$$
\begin{aligned}
e_A &= -4\pi R_i v N N_{sp} \sum_{n=1}^{\infty} \left(a_{1n} \mathcal{B}_{\mathcal{I}1}(m_n R_i) + b_{1n} \mathcal{B}_{\mathcal{K}1}(m_n R_i) \right) \\
&\quad \sin\left(\frac{n\pi}{3}\right) \left[T_{c_n} \cos\left(m_n(\tau_t - \Delta_z) \right) - T_{s_n} \sin\left(m_n(\tau_t - \Delta_z) \right) \right], \\
e_B &= -4\pi R_i v N N_{sp} \sum_{n=1}^{\infty} \left(a_{1n} \mathcal{B}_{\mathcal{I}1}(m_n R_i) + b_{1n} \mathcal{B}_{\mathcal{K}1}(m_n R_i) \right) \\
&\quad \sin\left(\frac{n\pi}{3}\right) \left[T_{c_n} \cos\left(m_n \Delta_z \right) + T_{s_n} \sin\left(m_n \Delta_z \right) \right], \\
e_C &= -4\pi R_i v N N_{sp} \sum_{n=1}^{\infty} \left(a_{1n} \mathcal{B}_{\mathcal{I}1}(m_n R_i) + b_{1n} \mathcal{B}_{\mathcal{K}1}(m_n R_i) \right) \\
&\quad \sin\left(\frac{n\pi}{3}\right) \left[T_{c_n} \cos\left(m_n(\tau_t + \Delta_z) \right) + T_{s_n} \sin\left(m_n(\tau_t + \Delta_z) \right) \right]. \qquad (4.15)
\end{aligned}
$$

It can be observed that the only difference between these expressions and the ones for the unskewed EMF waveforms is the coefficient T_{c_n} and the additional sine terms with a coefficient T_{s_n}. In the case of sinusoidal or triangular skewing, T_{s_n} is zero and the sine terms can be disregarded leaving the only difference of the coefficient T_{c_n}. A calculation of the EMF waveforms has been performed for the sinusoidal skewing transformation (d) with a skewing amplitude of $\Delta_s = 65$ el.deg. and the results are shown in Fig. 4.3 together with the overlay and add method (4.1), the constant velocity is 0.5 m/s. Good agreement has been found between the semi-analytical and overlay and add method of the unskewed FE calculation. It can be observed that the EMF waveform has a more sinusoidal shape and the harmonic content is decreased, dispite of a decrease in the fundamental harmonic.

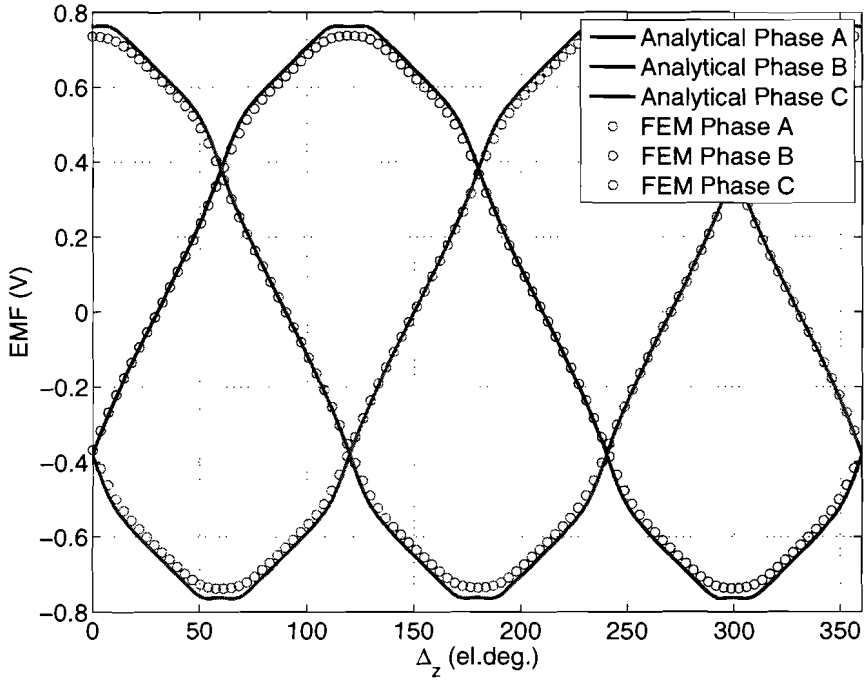

Fig. 4.3: EMF waveform for the sinusoidal skewing transformation (d) with a skewing amplitude of $\Delta_s = 65$ el.deg.

4.3 Force calculation

There is a difference in the force level when translator or stator skewing is considered. To explain this in a clear way, let us consider only the Lorentz force density $\mathbf{f} = \mathbf{J} \times \mathbf{B}$, where $\mathbf{B}$ is mainly the field due to the magnets where the radial component is dominating. By approximation this gives $f_z = J_\theta B_{\mathrm{I}_r}$. If translator skewing is considered, then B_{I_r} does not change in direction and the two vectors $\mathbf{J}$ and $\mathbf{B}$ are still orthogonal. If, however, stator skewing is considered, the θ-component of the current density vector $\mathbf{J}$ decreases and an extra component in the z-direction appears which does not contribute to axial thrust. Therefore, in general the force level will be slightly lower for stator skewing then for translator skewing depending on the skewing amplitude, Δ_s.

The force calculation is again performed by means of the Maxwell Stress Tensor and again it is shown that the formula of the unskewed model still holds but with a correction factor T_{c_n} for the cosine terms and additional sine terms with a factor T_{s_n}. For stator skewing the form of these coefficients is slighlty different and it becomes difficult, if not impossible to solve analytically, therefore, these coefficients are calculated numerically.

4.3.1 Translator skewing

The axial force given by the Maxwell Stress method (3.117) is

$$F_z = \frac{R_{ag} N_p}{\mu_0} \int_0^{2\pi} \int_{-\tau_p}^{\tau_p} B_{ag_z} B_{ag_r} dz d\theta \Big|_{r=R_{ag}}, \tag{4.16}$$

$$\Downarrow$$

$$F_z = \frac{R_{ag} N_p}{\mu_0} \int_0^{2\pi} \int_{-\tau_p}^{\tau_p} (B_{\mathrm{I}_z} + B_{\mathrm{III}_{z_A}} + B_{\mathrm{III}_{z_B}} + B_{\mathrm{III}_{z_C}}) (B_{\mathrm{I}_r} + B_{\mathrm{III}_{r_A}} + B_{\mathrm{III}_{r_B}} + B_{\mathrm{III}_{r_C}}) dz d\theta \Big|_{r=R_{ag}}, \tag{4.17}$$

where B_{I_z} and B_{I_r} are now skewed according to the considered skewing transformation $\mathcal{S}(\theta)$. Using the same simplification of the field equations as done for the unskewed force calculation and the trigonometric properties given in Appendix A.2, the axial force expression becomes

$$F_z = R_{ag} N_p \tau_p \int_0^{2\pi} \sum_{n=1}^{\infty} K_{w_n} \Bigg[(Q_1 Q_4 + Q_2 Q_3) \Bigg\{ J_A \cos\Big(m_n(\Delta_z - \tau_t - \mathcal{S})\Big) + J_B \cos\Big(m_n(\Delta_z - \mathcal{S})\Big) + J_C \cos\Big(m_n(\Delta_z + \tau_t - \mathcal{S})\Big) \Bigg\} \Bigg] d\theta,$$

using property (6.15), the variable $\mathcal{S}$ can be separated giving

$$\begin{aligned} F_z &= R_{ag}N_p\tau_p\sum_{n=1}^{\infty}K_{w_n}(Q_1Q_4+Q_2Q_3)\Bigg[\int_0^{2\pi}\cos(\mathcal{S})d\theta\Bigg\{J_A\cos\Big(m_n(\Delta_z-\tau_t)\Big) \\ &\quad +J_B\cos\Big(m_n(\Delta_z)\Big)+J_C\cos\Big(m_n(\Delta_z+\tau_t)\Big)\Bigg\} \\ &\quad +\int_0^{2\pi}\sin(\mathcal{S})d\theta\Bigg\{J_A\sin\Big(m_n(\Delta_z-\tau_t)\Big) \\ &\quad +J_B\sin\Big(m_n(\Delta_z)\Big)+J_C\sin\Big(m_n(\Delta_z+\tau_t)\Big)\Bigg\}\Bigg]. \end{aligned} \tag{4.18}$$

Define $L_{ax}=2N_p\tau_p$ as the axial length of the stator and $C_n=Q_1Q_4+Q_2Q_3$ together with the definitions of T_{c_n} and T_{s_n} and the expression becomes

$$\begin{aligned} F_z &= \frac{R_{ag}L_{ax}}{2}\sum_{n=1}^{\infty}\Bigg[K_{w_n}C_n \\ &\quad T_{c_n}\Bigg\{J_A\cos\Big(m_n(\Delta_z-\tau_t)\Big)+J_B\cos\Big(m_n(\Delta_z)\Big)+J_C\cos\Big(m_n(\Delta_z+\tau_t)\Big)\Bigg\} \\ &\quad T_{s_n}\Bigg\{J_A\sin\Big(m_n(\Delta_z-\tau_t)\Big)+J_B\sin\Big(m_n(\Delta_z)\Big)+J_C\sin\Big(m_n(\Delta_z+\tau_t)\Big)\Bigg\}\Bigg], \end{aligned}$$

with

$$C_n=\frac{b_{1n}c_{4n}-a_{1n}c_{3n}}{c_{4n}c_{1n}-c_{2n}c_{3n}}\Big(\mathcal{B}_{\mathcal{I}0}(m_nR_{ag})\mathcal{B}_{\mathcal{K}1}(m_nR_{ag})+\mathcal{B}_{\mathcal{I}1}(m_nR_{ag})\mathcal{B}_{\mathcal{K}0}(m_nR_{ag})\Big).$$

and again the same force expression is obtained despite of the extra coefficient T_{c_n} and additional sine terms with a coefficient T_{s_n}. The force waveform is calculated for a translator displacement of 360 electrical degrees, a current density of $J_0=7.5A/mm^2$ with sinusoidal excitation with sinusoidal skewing for different skewing amplitudes. The results are shown in Fig. 4.4. In order to confirm the analytical solution, a 3D FEM is needed. However the force can approximatly be calculated as

$$F_{sk}=\frac{e_{sk_A}i_A+e_{sk_B}i_B+e_{sk_C}i_C}{v}, \tag{4.19}$$

where e_{sk_A}, e_{sk_B} and e_{sk_C} are the skewed EMF waveforms obtained by the overlay and add method described by (4.1). Acceptable agreement has been found, the apparent errors in the analytical model are probably caused by neglecting the slotting effect and the abstraction of the current sheet model. Further, the comparison with the FE solution is not exact since the approximation of the force by (4.19) is not exact. It can be observed that the force ripple does not decreases monotonally with the skewing amplitude, and there will be optimum values which will be calculated in section 4.4.

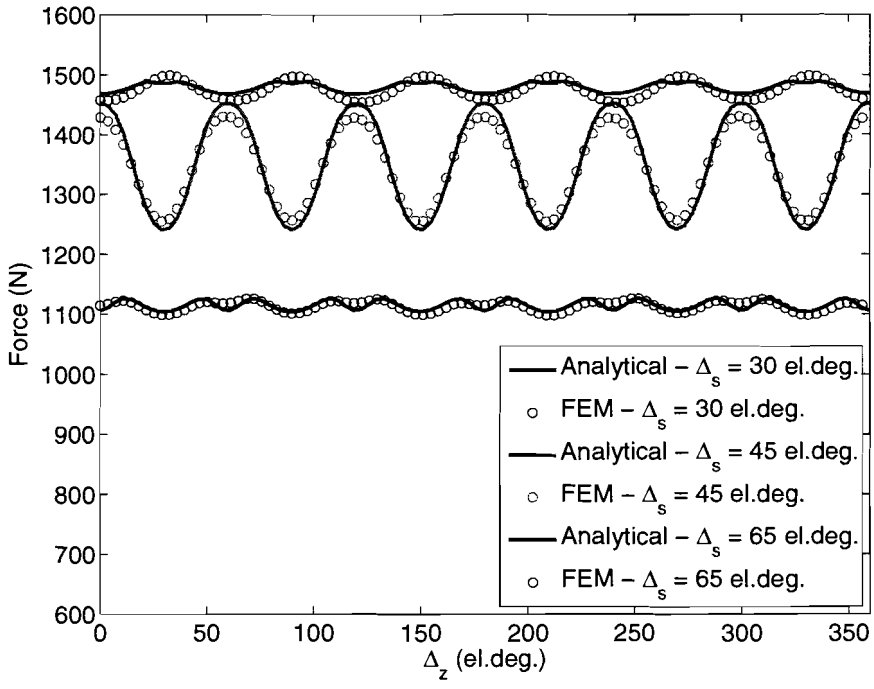

Fig. 4.4: Force as function of displacement for sinusoidal translator skewing.

4.3.2 Stator skewing

In Fig. 4.5 one pole-pair of the machine is unrolled for the case that the stator is sinusoidally skewed. When stator skewing is applied, the currents have two components, one in the θ-direction and one in the z-direction. The unskewed magnets have a field component in the radial and axial direction. Thus by calculating the Lorentz force with the crossproduct $\mathbf{J} \times \mathbf{B}$ gives us three components. The axial thrust force is proportional to $J_\theta B_r$, the angular component which is proportional to $J_z B_r$ and a radial strain proportional to $J_\theta B_z$. The two last components are eliminated by the use of a skewing transformation with more then one period, $p > 1$.

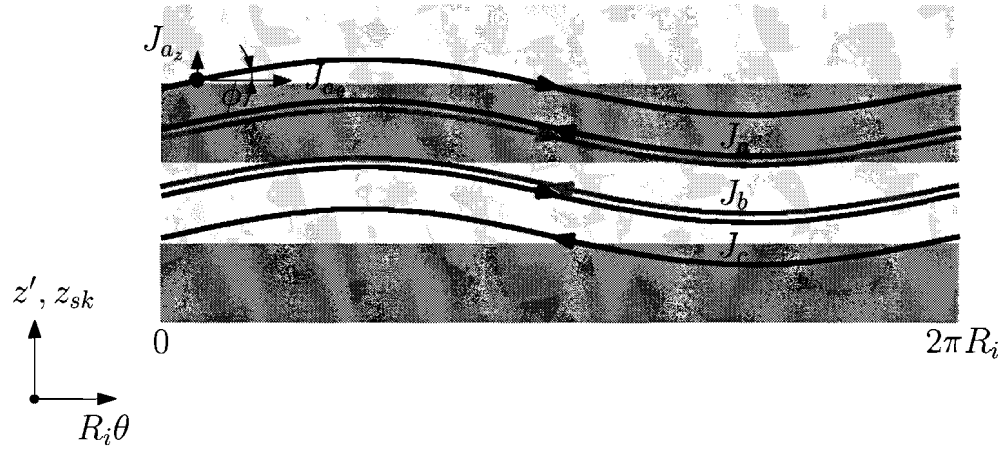

Fig. 4.5: Schematic view of sinusoidal stator skewing.

In Section 2.3 the distribution of the current density is discribed which was a vector in the angular direction. In the case of stator skewing the direction of the current density depends on the skewing transformation and therefore, the angular component of the current density vector is

$$J_{s_\theta} = J_s \cos(\phi) \tag{4.20}$$

Where ϕ is the angle of the skewing transformation with the θ-axis as indicated in Fig. 4.5 and can be calculated as

$$\phi = \arctan\left(\frac{1}{R_i}\frac{d\mathcal{S}(\theta)}{d\theta}\right) \tag{4.21}$$

Now that the angular current density as function of the skewing transformation is known, the axial force can be calculated as

$$F_z = \frac{R_{ag}N_p}{\mu_0}\int_0^{2\pi}\int_{-\tau_p}^{\tau_p} B_{ag_z}B_{ag_r}\,dz\,d\theta\Big|_{r=R_{ag}}, \tag{4.22}$$

$$\Downarrow$$

$$F_z = \frac{R_{ag}N_p}{\mu_0}\int_0^{2\pi}\int_{-\tau_p}^{\tau_p}(B_{\mathrm{I}_z} + B_{\mathrm{III}_{z_A}} + B_{\mathrm{III}_{z_B}} + B_{\mathrm{III}_{z_C}})$$
$$(B_{\mathrm{I}_r} + B_{\mathrm{III}_{r_A}} + B_{\mathrm{III}_{r_B}} + B_{\mathrm{III}_{r_C}})\,dz\,d\theta\Big|_{r=R_{ag}}, \tag{4.23}$$

where the magnetic fields of the stator currents are now skewed according to the skewing transformation, $\mathcal{S}$, and where the current densities are scaled by $\cos(\phi)$. Using the same simplification of the field equations as done for the unskewed force calculation and the trigonometric identities given in Appendix A.2, the axial force expression becomes

$$\begin{aligned} F_z &= R_{ag}N_p\tau_p \int_0^{2\pi} \sum_{n=1}^{\infty} K_{w_n} \Bigg[(Q_1Q_4 + Q_2Q_3) \Bigg\{ J_A \cos(\phi) \cos\left(m_n(\Delta_z - \frac{2\tau_p}{3} - \mathcal{S})\right) \\ &\quad + J_B \cos(\phi) \cos\left(m_n(\Delta_z - \mathcal{S})\right) + J_C \cos(\phi) \cos\left(m_n(\Delta_z + \frac{2\tau_p}{3} - \mathcal{S})\right) \Bigg\} \Bigg] d\theta, \end{aligned}$$

using (6.15). the variable $\mathcal{S}$ can be separated giving

$$\begin{aligned} F_z &= R_{ag}N_p\tau_p \sum_{n=1}^{\infty} K_{w_n}(Q_1Q_4 + Q_2Q_3) \Bigg[\int_0^{2\pi} \cos(\mathcal{S}) \cos(\phi) d\theta \Bigg\{ J_A \cos\left(m_n(\Delta_z - \frac{2\tau_p}{3})\right) \\ &\quad + J_B \cos\left(m_n(\Delta_z)\right) + J_C \cos\left(m_n(\Delta_z + \frac{2\tau_p}{3})\right) \Bigg\} \\ &\quad + \int_0^{2\pi} \sin(\mathcal{S}) \cos(\phi) d\theta \Bigg\{ J_A \sin\left(m_n(\Delta_z - \frac{2\tau_p}{3})\right) \\ &\quad + J_B \sin\left(m_n(\Delta_z)\right) + J_C \sin\left(m_n(\Delta_z + \frac{2\tau_p}{3})\right) \Bigg\} \Bigg]. \end{aligned} \tag{4.24}$$

Define again the axial length of the stator as $L_{ax} = 2N_p\tau_p$, and $C_n = Q_1Q_4 + Q_2Q_3$ gives

$$\begin{aligned} F_z &= \frac{R_{ag}L_{ax}}{2} \sum_{n=1}^{\infty} \Bigg[K_{w_n}C_n \\ &\quad T_{c_n} \Bigg\{ J_A \cos\left(m_n(\Delta_z - \frac{2\tau_p}{3})\right) + J_B \cos\left(m_n(\Delta_z)\right) + J_C \cos\left(m_n(\Delta_z + \frac{2\tau_p}{3})\right) \Bigg\} \\ &\quad T_{s_n} \Bigg\{ J_A \sin\left(m_n(\Delta_z - \frac{2\tau_p}{3})\right) + J_B \sin\left(m_n(\Delta_z)\right) + J_C \sin\left(m_n(\Delta_z + \frac{2\tau_p}{3})\right) \Bigg\} \Bigg], \end{aligned}$$

with

$$C_n = \frac{b_{1n}c_{4n} - a_{1n}c_{3n}}{c_{4n}c_{1n} - c_{2n}c_{3n}} \Big(\mathcal{B}_{\mathcal{I}0}(m_nR_{ag})\mathcal{B}_{\mathcal{K}1}(m_nR_{ag}) + \mathcal{B}_{\mathcal{I}1}(m_nR_{ag})\mathcal{B}_{\mathcal{K}0}(m_nR_{ag}) \Big).$$

and where T_{c_n} and T_{s_n} are now changed to

$$T_{c_n} = \int_0^{2\pi} \cos\left(\arctan\left(\frac{1}{R_i} \frac{d\mathcal{S}(\theta)}{d\theta} \right) \right) \cos\left(m_n\mathcal{S}(\theta)\right) d\theta \tag{4.25}$$

$$T_{s_n} = \int_0^{2\pi} \cos\left(\arctan\left(\frac{1}{R_i} \frac{d\mathcal{S}(\theta)}{d\theta} \right) \right) \sin\left(m_n\mathcal{S}(\theta)\right) d\theta \tag{4.26}$$

The expressions of T_{c_n} and T_{s_n} are very difficult, if not impossible, to solve analytical. Therefore, these integrals are calculated numerically for a given skewing transformation.

The only difference between stator and translator skewing is an extra term in the integrals of T_{c_n} and T_{s_n} which is caused by the angle ϕ of the coils with respect to the θ-axis. This angle causes a force decrement which is proportional to the skewing amplitude and it is invers proportional to the inner radius of the stator. Another important remark is that the number of periods definitely influences the force decrement, since the higher the number of periods, the larger the angle ϕ will be. Thus, stator and translator skewing have the same behaviour albeit a small force decrement for stator skewing. Therefore, regarding maximum force topologies, translator skewing is more preferred, despite of the high costs for the magnets since the magnets have to be made of segments of different shapes.

4.4 Dependency on the skewing amplitude

One of the main reason to apply skewing is to reduce the cogging effect, the force ripple due to the winding distribution and the harmonics of the magnetic field, and the THD of the EMF waveform, THD_e. A disadvantage of skewing is that not only the higher harmonics decrease, but also the fundamental and subharmonics of the magnetic field, which contribute to the mean value of the force, decrease. A compromise has to be made between the amount of harmonic content and the amplitude of the fundamental of the EMF waveform, e_1. In Fig. 4.6, the amplitude of the fundamental of the EMF waveform, e_1, normalised on the amplitude of the fundamental of the unskewed waveform, $e_{1_{unsk}}$, is plotted as a function of the skewing amplitude for different skewing topologies.

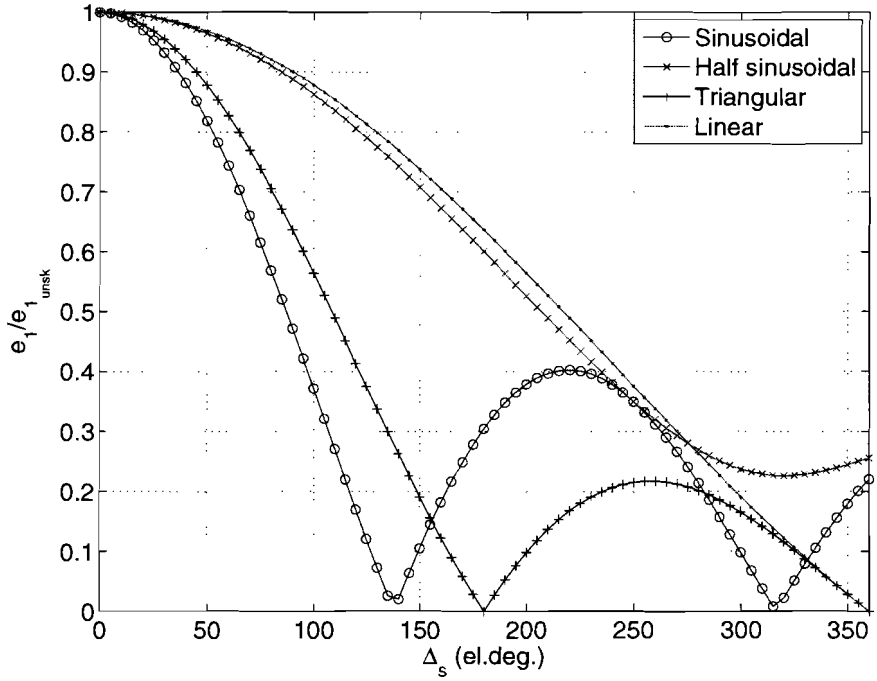

Fig. 4.6: Normalised fundamental of the EMF-waveform for different skewing topologies.

The result is quite understandable, if, for example, triangular skewing is considered, then it is obvious that for a skewing amplitude of 180 el.deg. (or 360 el.deg.), e_1 drops to zero since every slot of the stator links as much positive flux as negative flux, and the total flux linkage is always zero. For linear skewing this happens at 360 el.deg.

Furthermore, the THD_e normalised on the $THD_{e_{unsk}}$ of the unskewed actuator is plotted as function of the skewing amplitude for different skewing topologies in Fig. 4.7. It can be seen that the THD_e drops much faster then e_1, which means that the THD_e can be decreased drastically without loosing much performance. If, for example, the first suboptimal skewing amplitude of 25 electrical degrees of the sinusoidal skewing is considered, then e_1 is only decreased with 6%, whereas the THD_e is decreased with 82%. The same thing can be done for the force waveform but similar results are found since the coefficients, T_{c_n} and T_{s_n}, are the same for the force and EMF calculation for a given skewing topology. The only difference is a lower level of the force for stator skewing, depending on the skewing amplitude, stator bore radius and number of periods.

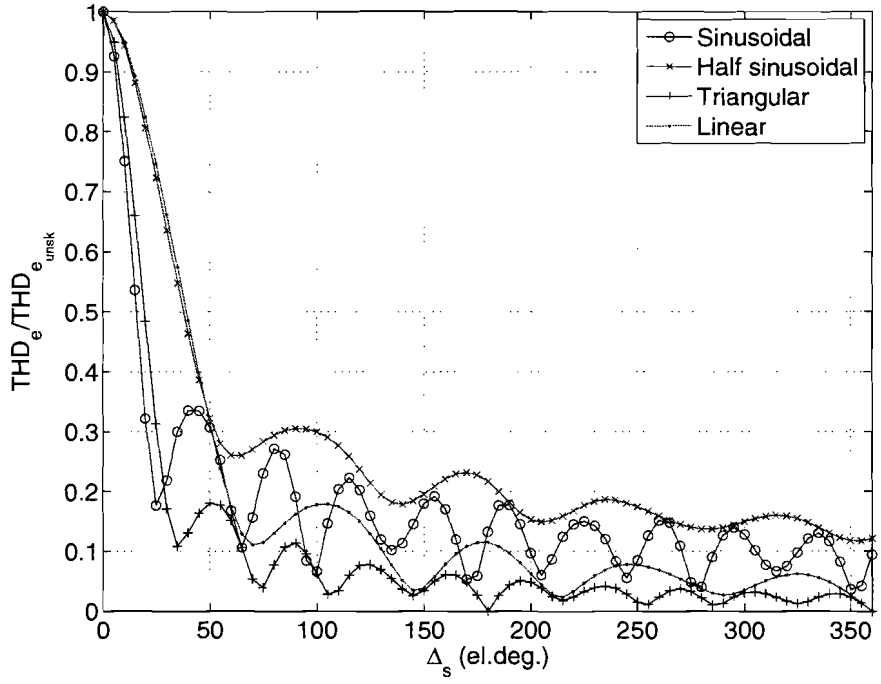

Fig. 4.7: Normalised THD of the EMF-waveform for different skewing topologies.

From the four considered skewing topologies, sinusoidal skewing is more preferred since the skewing amplitudes are the smallest for a given desired THD reduction. Therefore, the cost of the magnets will be decreased since fabrication and magnetisation is simplified for smaller skewing amplitudes. However, due to the small difference between triangular skewing and sinusoidal skewing, it is in most cases better to choose triangular skewing, since a perfect sinusoidal skewing increases the costs of the magnets.

5. SCHWARZ-CHRISTOFFEL CONFORMAL MAPPING

Analytical descriptions of the magnetic field distribution and the related force and EMF waveforms have the advantage of giving physical insight into the design and optimisation problem of finding the optimal geometry for a given set of performance specifications. Although these methods are very elegant and fast, for a geometry with a slotted structure, the slotting effect is difficult to incorporate. This slotting effect and its related cogging force can be eliminated by means of control, [9], however, reducing this effect during the design offers the benefit of reducing the need for control, and thereby increasing the efficiency and stability of the actuator. In [10], it is shown that the cogging force due to the slotting effect can have an amplitude of 120 N, which is relativly large depending on the application and therefore, it cannot be neglected during the design and optimisation process.

In order to model this effect, the Schwarz-Christoffel (SC) conformal mapping technique is used, [3]. This theory originates form the Riemann mapping theorem (1851) which states that any simply connected region in the complex domain can be mapped onto any other provided that neither is the entire plane. This method was widely described in the literature and mainly adressed to the rotary machines: synchronous and asynchronous ones, [13, 14, 15, 16, 19]. This Chapter explains the application of this method for a tubular PM actuator in order to calculate the related cogging force due to the slotting effect, as well as the total force (neglecting end effects). The tubular structure of the machine gives some complications since the SC-mapping technique only applies to two-dimensional Cartesian domains. A mapping based upon 'unrolling' and 'stretching' the tubular machine into a linear machine is used to solve this problem. Furthermore, the modelling of coils and magnets in the mapping domain is considered and the results are verified with the FEM of FLUX 2D®, [20].

5.1 Principle and strategy

Conformal mapping is a mathematical transformation of one domain to another. It has the ability to map a complex structure, like a slotted stator, to a relative simple structure (circle, rectangle, bi-infinite strip, upper half plane, etc.) of which the field solutions are given in the literature. The original domain is called as the W-domain, where the actuator consists of vertices, $w_1, ..., w_n$, and interior angles, $a_1\pi, ..., a_n\pi$, in counterclockwise order. The mapping domain is denoted as the Z-domain, with corresponding prevertices, $z_1, ..., z_n$. It is possible to consider the total actuator including end and slotting effects, however one pole-pair, see Fig. 5.1, has already 28 vertices. Taking into account that the total actuator consists of five pole-pairs, $N_p = 5$, this would result in a polygon of more than 140 points since the extra pole-pairs of the translator, which are situated outside the stator, have to be taken into account in order to model the end effects. The calculation of the mapping function and magnetic field distribution would therefore need a long computation time. However, the end effects can be considered seperately from the total force by firstly, considering only one pole-pair of the total actuator, hereby excluding the end effects, and secondly, considering only end effects by modelling the stator as a full iron block, which drastically decreases the number of vertices. In this hesis only one pole-pair of the actuator is considered, where end effects can be modelled following the same strategy.

Due to the physical nature of the electrical machines, the conversion of the electromagnetic energy takes place in the air gap. Thus, the identification of the magnetic field inside the air gap is one of the major steps within the design procedure of electrical machines. The polygon, P_w, should therefore represent the air gap together with the magnet region. However, the polygon, P_w, must be closed and since the airgap region for one pole-pair is not a closed structure in a linear machine, periodical boundary conditions are applied, which are represented by two extra lines in the total polygon, (w_1, w_2) and (w_3, w_4), see Fig. 5.1. The mapping of this polygon onto a rectangle is applied, where it is ensured that the left and right sides of the rectangle correspond to the extra lines, (w_1, w_2) and (w_3, w_4), in the W-domain. Therefore, the same periodical boundary conditions can be applied in the Z-domain, hereby eliminating the need of an extra transformation to enforce periodical boundary conditions. Normally, the rectangle is mapped onto a circle to enforce periodical boundary conditions, [16].

The mapping function from a rectangle polygon, P_z, in the Z-domain to the actuator airgap polygon, P_w, in the W-domain is given by [3]

$$w = f(z) = C_1 + C_2 \int_z \prod_{k=1}^{n} (z - z_k)^{a_k - 1} dz. \tag{5.1}$$

where C_1 and C_2 are a complex offset and scaling constant, respectively.

In Fig. 5.2 the mapping in the Z-domain is shown. Note that the four corners in the W-domain, $(w_1, ..., w_4)$, correspond to the four corners in the Z-domain, $(z_1, ..., z_4)$. This is necessary in order to have the same boundary conditions on each side of the rectangle in the Z-domain. So, the lines, (z_1, z_2) and (z_3, z_4), are periodic boundary conditions and the lines, (z_2, z_3) and (z_4, z_1), represent the boundary conditions at the iron.

The goal is to calculate the field at the center radius of the air gap, $R_{ag} = \frac{R_m + R_i}{2}$, therefore it is necessary to know which points in the Z-domain correspond to the points of the

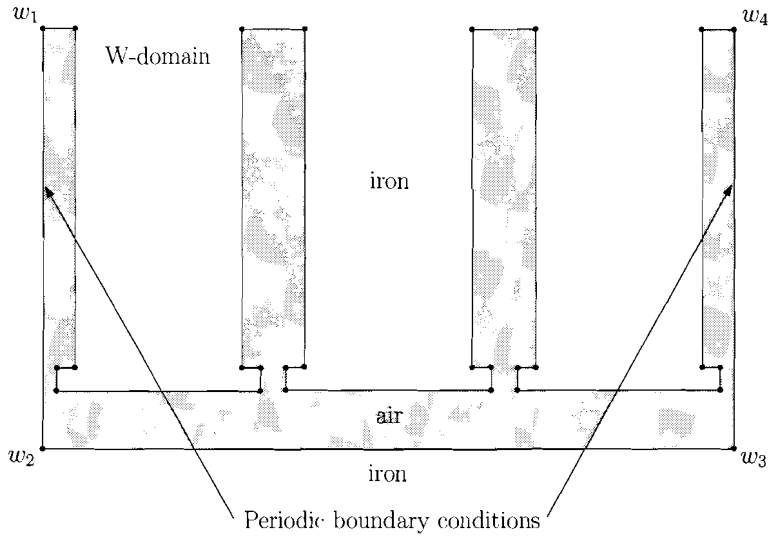

Fig. 5.1: Polygon P_w of the airgap region of one pole-pair of the tubular PM actuator.

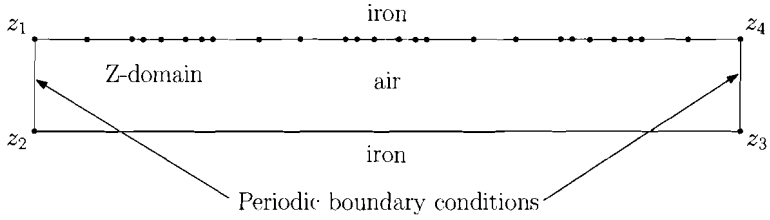

Fig. 5.2: Mapping of the polygon P_w to the rectangular Z-domain.

center radius of the air gap in the W-domain. This is done by the inverse transformation, $z = f^{-1}(w)$, which is impossible to solve analytically for polygons which consist of more then four points, and therefore this inverse transformation is calculated numerically. Since this increases the computation time, these points have to be limited according to the application. Once the points in the Z-domain are determined, the field solution can be calculated at these points. The field solution obtained at the points, z_i, can then be plotted as function of the corresponding points in the W-domain, w_i, which is the desired solution. So the strategy can be summerised as:

- Define polygon P_w in the W-domain,
- Calculate mapping function $f(z)$,
- Define grid (z_i) in the Z-domain by $f^{-1}(w_i)$,
- Calculate field in the Z-domain at points z_i,
- Mapping of the field solution to the W-domain,
- Proceed with EMF and force calculation.

5.2 Coordinate system

The SC-mapping strategy is applied to one pole-pair of the tubular PM actuator. In order to use the SC-mapping method for field calculation in the Z-domain and transform it to the W-domain. Consider again the magnetic field equation in terms of the magnetic vector potential, $\mathbf{A}$, given by the Poisson equation

$$\nabla^2 \mathbf{A} = -\mu_0(\mathbf{J} + \nabla \times \mathbf{M}), \tag{5.2}$$

Note that, since it is a two-dimensional problem, also the scalar potential could be used. For a source-free region the Poisson equation reduces to the Laplace equation $\nabla^2 \mathbf{A} = \mathbf{0}$. These equations should be the same in both domains. The Z-domain is always a two-dimensional Cartesian coordinate system, (x, y), but the W-domain is a two-dimensional axisymmetric cylindrical coordinate system, (r, z), which has a different form of Laplace equation. In both domains the magnetic field has only directions in (r, z) and (x, y), respectively. Therefore, the magnetic vector potential, $\mathbf{A}$, has only a direction orthogonal to both directions of both domains, which is independent on the orthogonal direction. In summary

$$\mathbf{A}_{W-dom} = A_\perp(r, z)\mathbf{e}_\perp, \tag{5.3}$$
$$\mathbf{A}_{Z-dom} = A_\perp(x, y)\mathbf{e}_\perp, \tag{5.4}$$

where $\mathbf{e}_\perp$ is the unit vector in orthogonal direction of both domains, and evaluation of $\nabla^2 \mathbf{A}$ gives

$$\nabla^2 \mathbf{A}_{W-dom} = \frac{\partial^2 A_\perp}{\partial r^2} + \frac{1}{r}\frac{\partial A_\perp}{\partial r} - \frac{2}{r^2}A_\perp + \frac{\partial^2 A_\perp}{\partial z^2}, \tag{5.5}$$
$$\nabla^2 \mathbf{A}_{Z-dom} = \frac{\partial^2 A_\perp}{\partial x^2} + \frac{\partial^2 A_\perp}{\partial y^2}. \tag{5.6}$$

This means that a field solution in the Z-domain does not correspond to a field solution in the W-domain. Therefore, the geometry of the actuator is transferred from the axisymmetric cylindrical coordinate system, (r, z), to a Cartesian coordinate system, (u, v), by 'unrolling' and 'stretching' the tubular actuator, see Fig. 5.3. The mean area of the air gap is kept constant by taking the depth of the two-dimensional Cartesian model, L, equal to the circumference of the air gap, $2\pi R_{ag}$, and the geometry parameters in the direction of movement are also kept the same, $v = z$.

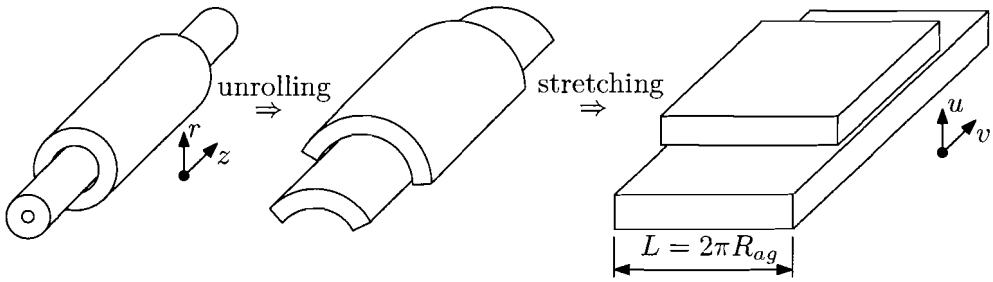

Fig. 5.3: Unrolling from (r, z) to (u, v).

While unrolling the actuator from (r, z) to (u, v), the permeances in the r- and z-directions should be the same as the permeances in u- and v-directions in order to have the same

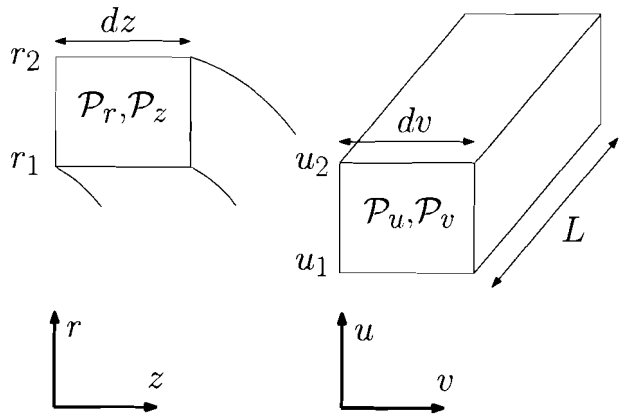

Fig. 5.4: The permeances in both coordinate systems.

electromechanical behaviour. This means that $\mathcal{P}_u = \mathcal{P}_r$ and $\mathcal{P}_v = \mathcal{P}_z$. However since v is already defined, there is only a freedom of changing u. Solving two independent equations with only one variable is impossible. Therefore, in general, it will be impossible to describe the tubular actuator as a linear actuator with the exactly the same behaviour. If a piece of material is considered in both the tubular and linear actuator, as depicted in Fig. 5.4 then the permeances in r-, z-, u- and v-directions are given by

$$\mathcal{P}_r = \frac{\mu\pi(r_1 + r_2)dz}{r_2 - r_1}, \tag{5.7}$$

$$\mathcal{P}_z = \frac{\mu\pi(r_2^2 - r_1^2)}{dz}, \tag{5.8}$$

$$\mathcal{P}_u = \frac{\mu L dv}{u_2 - u_1}, \tag{5.9}$$

$$\mathcal{P}_v = \frac{\mu L(u_2 - u_1)}{dv}. \tag{5.10}$$

It can be observed that the axial permeances depend quadratically on r. Therefore, the transformation from the axisymmetric cylindrical coordinate system to the two-dimensional Cartesian coordinate system is performed by keeping the axial permeances equal, $\mathcal{P}_v = \mathcal{P}_z$. And since $dv = dz$, the final transformation of the coordinate system is given by

$$u = \frac{r^2}{2R_{ag}}, \tag{5.11}$$

$$v = z. \tag{5.12}$$

Note that this introduces an error for the radial permeances, however this error is zero in the middle of the air gap, which is the most important position since the force is evaluated on the magnetic field solution in the middle of the air gap.

5.3 Field calculation

For calculation of the mapping function, the MATLAB® SC Toolbox [4] is used, the current version was released in 2005. This toolbox allows for automatic calculation of the mapping function (5.1). The polygon, P_w, is defined as in Fig. 5.1, where the transformation (5.11)-(5.12) is applied. If the mapping function is calculated, the grid in the W-domain has to be defined according to the points where the magnetic field has to be calculated. The grid points in the W-domain, $w_i = v_i + ju_i$, are complex numbers where the real part corresponds to the v-direction and the imaginary part corresponds to the u-direction. If a uniform grid is considered, all these points undergo an inverse transformation which is very time-consuming, and it is useful to consider only points inside the polygon, P_w, and eliminate the other ones, since for these points the mapping function (5.1) does not hold, see Fig. 5.5.

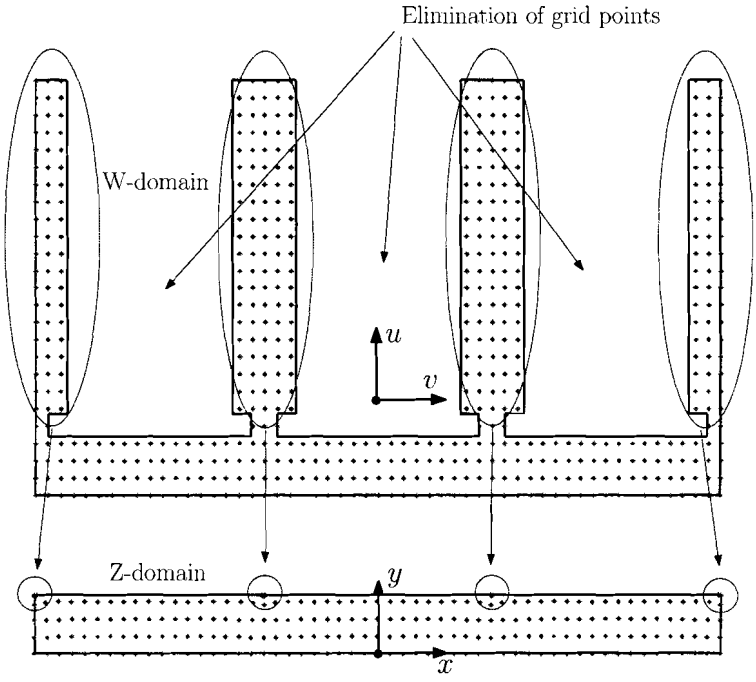

Fig. 5.5: Grid in the W-domain and Z-domain of one pole-pair of the tubular PM actuator.

These points are then transformed to the Z-domain by the inverse transformation $f^{-1}(w_i)$. The grid in the air gap and the magnets is relatively unchangable due to the SC-transformation, whereas the grid of the coils however, is almost mapped into a point as indicated in Figs. 5.5 and 5.7. This phenomenon is called crowding and it is best to avoid it because it influences the accuracy of the solution [2].

The coils are squares in the W-domain but in the Z-domain they are definitely not. In order to use standard field solutions in the Z-domain, the square coil is divided into a finite number of points, w_p, each with a current, $I_c = \frac{NI_{ph}}{N_c}$, where I_{ph} is the phase current, N is the number of windings and N_c is the number of point wires used for mapping the square coil. These point wires, z_p, are also mapped into the Z-domain, where the magnetic field is calculated for each of them. The same holds for the magnets and therefore, they are modelled as two current sheets at the side of the magnets. This equivalency is valid for rare-earth permanent magnets where μ_r is close to unity and when a homogeneous

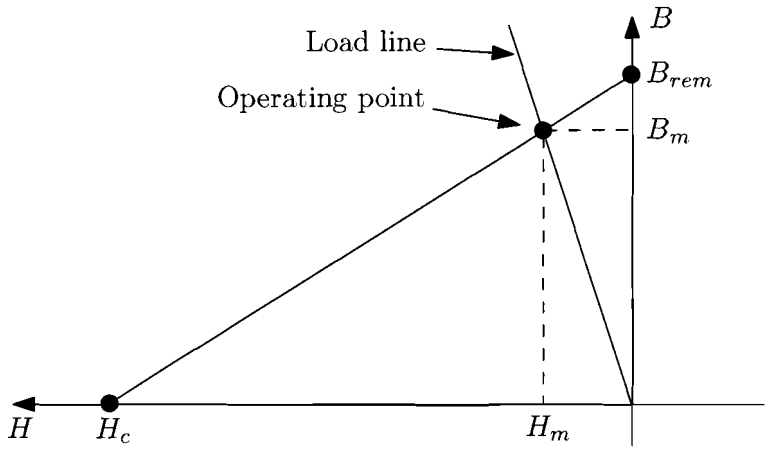

Fig. 5.6: Demagnetisation curve of the magnets and the load line.

magnetisation is considered. These current sheets consist of a finite number, N_m, of points, which are also mapped to the Z-domain. The value of the current for one wire of the current sheet is defined as

$$I_m = \pm\frac{H_m h_m}{N_m}, \tag{5.13}$$

$$H_m = \frac{B_m}{\mu_r \mu_0}, \tag{5.14}$$

where B_{rem} is the remanence flux density, μ_r is the recoil permeability and h_m is the original height of the magnets in the cylindrical coordinate system. The working point of the magnet is approximately given by

$$B_m = \frac{B_{rem}}{1 + \frac{\mu_r g(R_r + R_m)}{2 h_m R_{ag}}}. \tag{5.15}$$

The total mapping of the wires is shown in Fig. 5.7. The next step is to calculate the field solution in the Z-domain for all these point wires. The flux density has directions in u and v, but due to the transformation the u-direction (or v-direction) in the W-domain does not correspond to the y-direction (or x-direction) in the Z-domain, and therefore if the flux density has to be mapped back to the W-domain, the gradient of the mapping function has to be taken into account

$$\mathbf{B}_{W-dom}(w) = \frac{\mathbf{B}_{Z-dom}(z)}{\nabla f(z)}. \tag{5.16}$$

Another option is to calculate the magnetic vector potential in the Z-domain, since it has only a component in the θ-direction, which is unchanged due to the transformation. The magnetic vector potential is then easily obtained in the W-domain and the magnetic field in the W-domain can then be calculated by

$$\mathbf{A}_{W-dom}(w) = \mathbf{A}_{Z-dom}(z), \tag{5.17}$$

$$\mathbf{B}_{W-dom}(w) = \nabla \times \mathbf{A}_{W-dom}(w). \tag{5.18}$$

However, since (5.18) requires more points, w_i, to be mapped in order to calculate the curl, it is more efficient to calculate $\mathbf{B}$ in the Z-domain and use (5.16) to calculate the magnetic

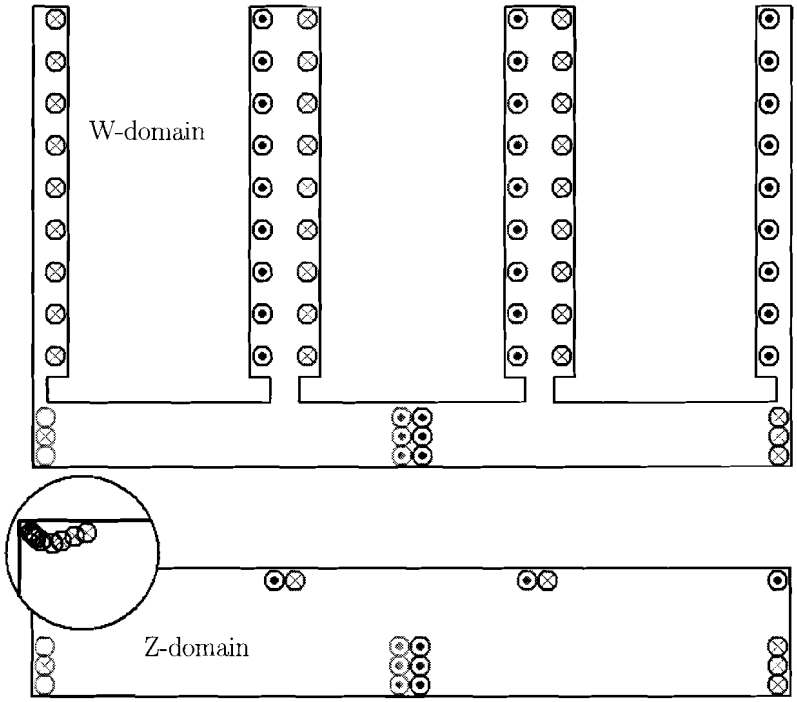

Fig. 5.7: Point wires in the W-domain and Z-domain of one pole-pair of the tubular PM actuator.

field in the W-domain. The total magnetic field solution is obtained by superposition of the individual field solutions of every point wire.

Thus, consider the Z-domain with one-point wire. The top and bottom of the rectangle have an iron boundary, whereas the left and right ones have periodic boundary conditions. The magnetic field solution is obtained by applying the imaging method to the top and bottom boundaries, and translation to the left and right boundaries. Normally, the imaging method requires a summation over the imaged point wires, but an analytical description is given in [7]. The only summation left is for superposition of the magnetic field of the translated point wires in the x-direction, Fig. 5.8. In practice, only a finite number of translations is considered, N_t.

The magnetic field of a single point wire is given in [7]

$$\mathbf{B}_{Z-dom}(x,y) = B_x(x,y)\mathbf{e}_x + B_y(x,y)\mathbf{e}_y, \tag{5.19}$$

with

$$B_x = \frac{I\mu_0}{4d_y}\sum_{k=-\infty}^{\infty}\left[\frac{\sin\left(\frac{\pi(y+y_p)}{d_y}\right)}{\cosh\left(\frac{\pi(x-x_p-kd_x)}{d_y}\right)-\cos\left(\frac{\pi(y+y_p)}{d_y}\right)} + \frac{\sin\left(\frac{\pi(y-y_p)}{d_y}\right)}{\cosh\left(\frac{\pi(x-x_p-kd_x)}{d_y}\right)-\cos\left(\frac{\pi(y-y_p)}{d_y}\right)}\right], \tag{5.20}$$

$$B_y = \frac{I\mu_0}{4d_y}\sum_{k=-\infty}^{\infty}\left[\frac{\sinh\left(\frac{\pi(x-x_p-kd_x)}{d_y}\right)}{\cosh\left(\frac{\pi(x-x_p-kd_x)}{d_y}\right)-\cos\left(\frac{\pi(y+y_p)}{d_y}\right)} + \frac{\sin\left(\frac{\pi(x-x_p-kd_x)}{d_y}\right)}{\cosh\left(\frac{\pi(x-x_p-kd_x)}{d_y}\right)-\cos\left(\frac{\pi(y-y_p)}{d_y}\right)}\right], \tag{5.21}$$

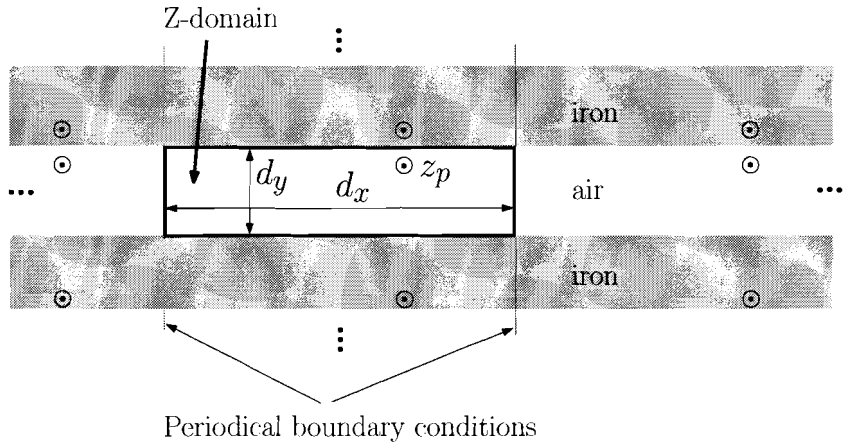

Fig. 5.8: Imaging and translation of a point wire in the Z-domain of one pole-pair of the tubular PM actuator.

where $x_p = \mathrm{Re}(z_p)$, $y_p = \mathrm{Im}(z_p)$, d_x- and d_y- the dimensions of the rectangle of the Z-domain and I is the current of the point wire, I_c, in the case of the coils and I_m, in the case of the magnets.

Additionally the magnetic field in the W-domain is calculated by (5.16) and compared with a FEM calculation for a phase current of $I_{ph} = \frac{J_0}{NA_c}$, for $J_0 = 7.5$ A/mm^2, A_c the area of the coils in the cylindrical domain and the parameters given in Tables 2.1, ?? and 5.1, the solution is plotted in Fig. 5.9. Very good agreement of the field solution inside the air gap has been found within 2%. Note that the FE calculation is performed on the axisymmetric cylindrical model and the relative permeability of the magnets is 1.05.

Tab. 5.1: Simulation parameters.

Variable	Value	Description
N_c	5	Number of point wires per coil
N_m	20	Number of point wires per current sheet of the magnets
N_t	5	Number of translations

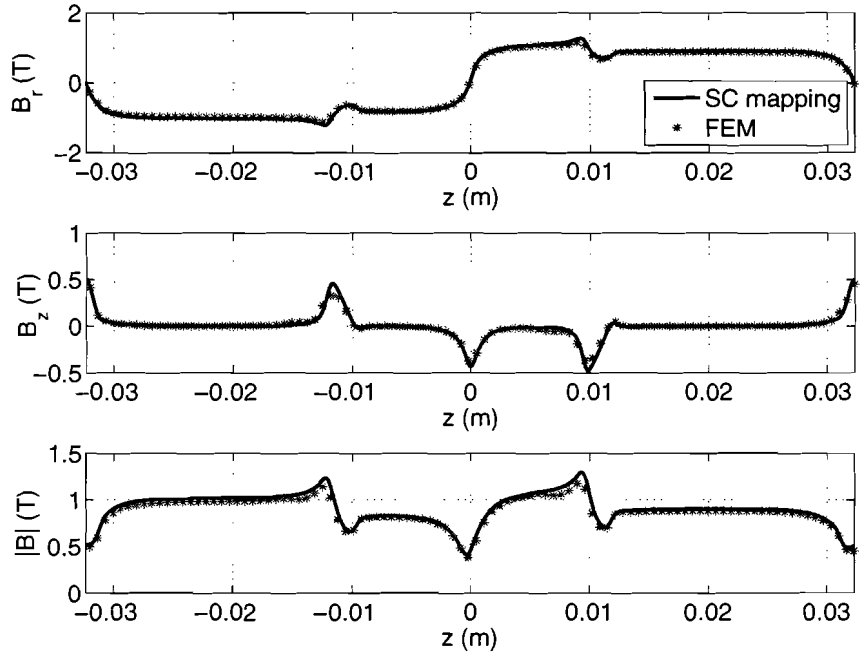

Fig. 5.9: Magnetic field in the air gap of one pole-pair of the tubular PM actuator.

5.4 EMF calculation

For the evaluation of the EMF waveform, the flux linkage of each phase must be calculated. The magnetic field is evaluated at the stator bore, R_i, instead of R_{ag} and the flux linkage is approximately the amount of radial flux at the tooth of the phase that is considered

$$\Psi_A = 2\pi R_i N \int_{\frac{\tau_t}{2}+D}^{\frac{3\tau_t}{2}+D} B_u dz \Big|_{r=R_i, I_c=0}, \tag{5.22}$$

$$\Psi_B = 2\pi R_i N \int_{-\frac{\tau_t}{2}+D}^{\frac{\tau_t}{2}+D} B_u dz \Big|_{r=R_i, I_c=0}, \tag{5.23}$$

$$\Psi_C = 2\pi R_i N \int_{-\frac{3\tau_t}{2}+D}^{-\frac{\tau_t}{2}+D} B_u dz \Big|_{r=R_i, I_c=0}. \tag{5.24}$$

This is the flux linkage of one tooth per phase and it has to be multiplied by the number of teeth per phase, N_{sp}, for the total flux linkage per phase. The EMF is then calculated as

$$e = -\frac{\partial \Psi}{\partial t} = -\frac{\partial \Psi}{\partial \Delta_z}\frac{\partial \Delta_z}{\partial t}. \tag{5.25}$$

These waveforms are calculated for a constant speed of $\frac{\partial \Delta_z}{\partial t} = 0.5$ m/s and shown in Fig. 5.10 together with the FE calculation, good agreement has been found. The EMF waveforms of the SC-mapping are slightly higher then the FE calculation due to the calculation of the fields at R_i which introduces a small error caused by the transformation from (r, z) to (u, v).

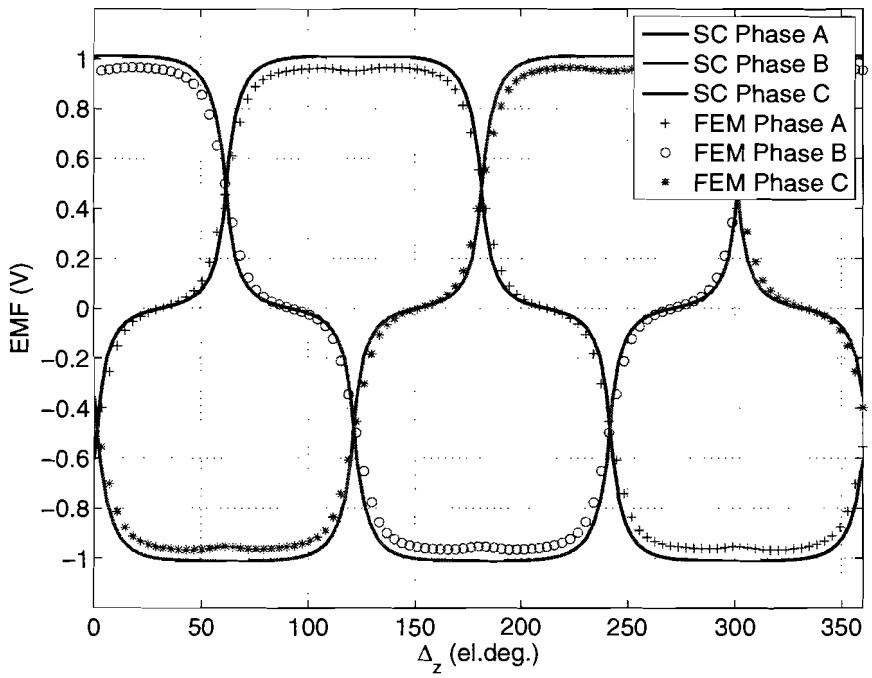

Fig. 5.10: EMF waveforms of the tubular PM actuator for a constant speed of 0.5 m/s.

5.5 Force calculation

When the total field distribution in the air gap is known, the force acting on the translator can be calculated by means of the Maxwell Stress Tensor

$$F = \frac{N_p}{\mu_0} \oint_S \mathbb{T}.\mathbf{n} dS, \tag{5.26}$$

where $\mathbf{n}$ is the normal vector on the surface S, N_p is the number of pole-pairs and the tensor is defined as

$$\mathbb{T} = \begin{bmatrix} B_r^2 - \frac{|B|^2}{2} & B_r B_\theta & B_r B_z \\ B_\theta B_r & B_\theta^2 - \frac{|B|^2}{2} & B_\theta B_z \\ B_z B_r & B_z B_\theta & B_z^2 - \frac{|B|^2}{2} \end{bmatrix}, \tag{5.27}$$

where B_r, B_θ and B_z is the total radial, angular and axial magnetic field at the surface S, respectively. In (5.26), S is the closed surface which consists of the airgap surface, $S_1 : u = g(R_{ag})$, the sides of the W-domain, $S_2 : v = -\tau_p$ and $S_3 : v = \tau_p$, and a surface in the back iron of the translator, $S_4 : u = g(R_b)$. If (5.26) is evaluated on S, only the surface of the air gap, S_1, is important because the sides of the w-plane, S_2 and S_3, have periodic boundary conditions which cancel each other since their normal vectors are in opposite direction, and the surface in the back iron of the magnets, S_4, has a high permeability which is negligible compared to the permeability of the air gap. This simplifies equation (5.26) to

$$F_v = \frac{N_p L}{\mu_0} \int_{-\tau_p}^{\tau_p} B_u\big(g(R_{ag}), v\big) B_v\big(g(R_{ag}), v\big) dv. \tag{5.28}$$

When movement is involved, only the sheets of the magnets are moved in the v-direction. In this way the mapping function stays fixed during movement, no grid mapping and coil mapping have to be performed which take a lot of computation time. The verification with FEM is shown in Fig. 5.11. This total force does not include end effects, however cogging effect due to the slotted structure is identified. The slotting effect itself is also calculated and verified with FEM, shown in Fig. 5.12. In every case acceptable results within 5% accuracy are achieved. The error results mainly from the mapping of the tubular actuator into a linear one. It needs further noting that the force calculation by means of the Maxwell Stress Tensor is very sensitive to the density of the grid.

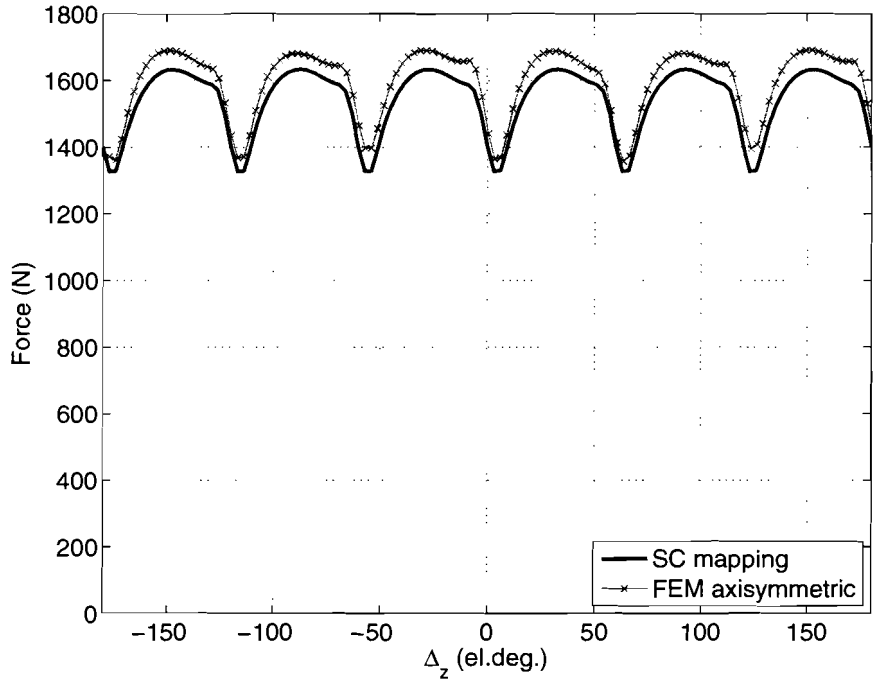

Fig. 5.11: Thrust force excluding end effects.

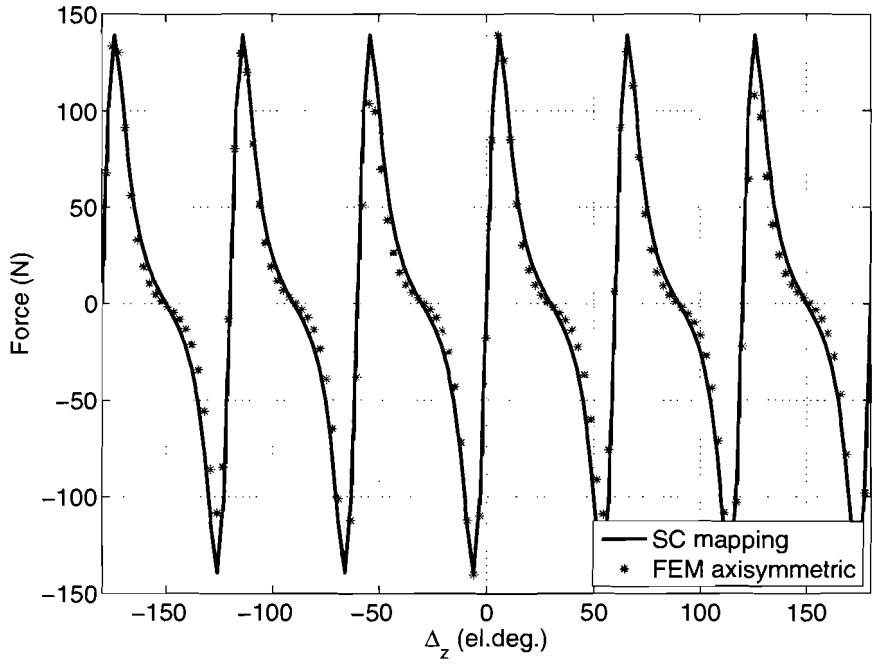

Fig. 5.12: Cogging effect due to slotting.

5.6 Computation time

Another issue that has to be considered is the computation time. In this geometry, a transformation of a polygon of 28 points has to be mapped which takes about 33 seconds, which is quite long when optimisation is considered. But if the polygon is slightly changed, which will be the case during optimisation, the SC-mapping algorithm can use the previous simulated mapping in order to calculate the mapping of the changed polygon, which results in a much faster mapping and is therefore still usefull for optimisation. The field and force calculations take less then a second, depending on the number of images and translations in the Z-domain and the resolution of the air gap. The coils consist of a finite number of wires which are mapped in the Z-domain. In Fig. 5.7 it can be observed that all these wires are almost mapped onto one point in the Z-domain. Thus, if knowledge about the field distribution close to the coils is not necessary (for example, for force calculation) the coils can be modelled by just a single wire which saves a number of field calculations and inverse mappings.

6. CONCLUSIONS AND RECOMMENDATIONS

6.1 Conclusions

In this thesis analytical and numerical techniques were represented for calculation of the magnetic field inside the air gap of a tubular permanent magnet actuator. With these techniques, a model can be derived which can predict the force profile given a set of geometry and material parameters. Given the accuracy of the model, it can be used for either a 'coarse' model or a 'fine' model in an optimisation routine, e.g. the space mapping technique, for finding the optimal geometry given the performance and geometry specifications.

First the semi-analytical magnetostatic framework is presented, where one pole-pair of the actuator is splitted up into radial regions, each with there own constant material properties. Axial periodic boundary conditions are applied and therefore, Fourier theory can be applied in order to describe the magnetisation vector and the winding distribution. Since only radial regions exist, no slotting effect can be included and due to the axial periodicity, end effects are excluded. The stator is therefore modelled as a full iron tube with a surface current sheet at the stator bore. So for this model only the force due to the stator currents can be predicted. The Poisson and Laplace equations are solved for every region of interest, mainly the airgap region. The magnetic field solution is compared to finite element analysis and acceptable agreement has been found, disregarding the slotting effect which is clearly visible in the FE solution and not in the analytical one. This method is applied for magnetic field calculation due to the magnets and the stator currents seperatly, superposition is applied to calculate the total magnetic field solution, since linear material characteristics are assumed and therefore, no saturation is modeled. Force calculation is performed by means of the Maxwell stress tensor. Acceptable agreements are found, albeit that a small error in the sixth harmonic of the force profile exists due to the surface current sheet modelling. Also the EMF waveform is calculated based upon the assumption that the flux linkage per tooth per phase is approximatly the amount of radial flux entering the tooth at the stator bore. This assumption gives good agreement with the FE calculation.

The previous described semi-analytical framework is extended for skewed topologies. By applying skewing to the stator or the translator, the amount of force ripple in the force profile can be decreased since for most applications only a constant force as function of displacement is desired. However, a skewed topology will also decrease the mean force since the flux linkage is decreased in every case. Since the force ripple due to the slotting and end effects is not modelled, only the effect of skewing onto the force ripple due to the stator currents is visible. Skewing is modelled by means of a shift in axial direction depending on angular position. In this way the semi-analytical framework for unskewed topologies can be used by applying the shift in axial direction depending on the chosen skewing transformation. Note that every skewing transformation can be implemented in

this way. The resulting description is almost the same as the unskewed one, despite of a correction factor for every harmonic of the force or EMF waveforms. Verification has been done with an overlay and add method for the unskewed EMF waveforms and good agreement has been found.

In order to model the slotting effect, and its related cogging force, a Schwarz-Christoffel conformal mapping technique has been applied to one pole-pair of the stator. Again, end effects are excluded. The Schwarz-Christoffel mapping technique allows for field calculation in a region where the boundary value problem is very difficult due to the complex geometry, as is the case for a slotted structure. The slotted airgap region for one pole-pair with periodical boundary conditions is mapped onto a rectangular where the left and right sides have the same periodical boundary conditions. The coils and magnets are modelled by current sheets which are discretisised into a finite number of point wires. These point wires are also mapped into the rectangular domain and magnetic field calculation is then performed with the imaging method to top and bottom, and the translation method to left and right sides of the rectangle for every mapped point wire. The total magnetic field solution is then mapped back to the original domain of the slotted air gap and verified with FEA. The total force excluding end effects is calculated by means of the Maxwell stress tensor and acceptable agreement within 3.5% accuracy has been found. Also the slotting effect is calculated seperatly and verified with FEM with an accuracy within 3.5%.

In total, the analytical model is able to predict the force due to the stator currents and EMF waveforms for unskewed and skewed topologies and the slotting effect is calculated by means of the Schwarz-Christoffel mapping. Both models are implemented in a Matlab environment and combination of these models is therefore very easy in order to predict the total force waveform,excluding end effects. The total model can be used as a coarse model in an optimisation routine in order to find the optimal geometry given the performance and geometrical specifications.

6.2 Recommendations

In both models, the end effects are excluded. Nevertheless it is possible to include this effects in both models. For the semi-analytical framework, the left and right end of the actuator can be modelled with radial and axial regions and the same procedure can be followed in order to calculate the left and right forces which contribute to the total end effect. The only difference is that now also axial boundary conditions are involved which make the analytical description much more complex. For the Schwarz-Christoffel mapping method, these end effects can be modelled by considering the stator as a full iron block together with the surroundings. Appropriate boundary condition can be applied and again the same procedure can be followed. Due to the time lag, the end effects are not modelled but it will be a future point of consideration.

If the end effects are modelled in the semi-analytical framework, it can be extended for skewed topologies in order to see the effect of skewing on the end effects. Also the effect of skewing on the slotting effect can be investigated by means of the overlay and add method.

The slotting effect can be calculated in an analytical way by means of dividing the total structure into radial and axial regions but the number of boundary conditions increases

drastically and a way of handling the complexity of the analytical description is necessary. It is also possible to describe the airgap length as a Fourier series, and incorporate that into the boundary conditions.

Since thermal physics is also described by Laplace and Poisson equations, the procedure of the analytical model can be used for investigation of the thermal distribution inside the actuator. However, more regions have to be considered simultaneously since also the environment has to be considered due to the convection currents and emissivity.

Bibliography

[1] M. Chung and D. Gweon. Modeling of the armature slotting effect in the magnetic field distribution of a linear permanent magnet motor. *Electrical engineering*, 84:101–108, 2002.

[2] T. K. Dellilo. The accuracy of numerical conformal mapping methods: A survey of examples and results. *Society for Industrial and Applied mathemathics*, 31(3):788–812, 1994.

[3] T. A. Driscoll and L. N. Trefethen. *Schwarz-Christoffel Mapping.* Cambridge University Press, Cambridge, 2002.

[4] T.A. Driscoll. Schwarz-Christoffel toolbox user's guide: Version 2.3. 2005.

[5] L. Encica, J. J. H. Paulides, E. Lomonova, and A. J. A. Vandenput. Electromagnetic and thermal design of a linear actuator using output polynomial mapping. *Proc. IEEE Industry Application Society 41th Annual Meeting*, 4:1919–1926, 2006.

[6] E.P. Furlani. *Permanent Magnet and Electromechanical devices.* Academic Press, USA, 2001.

[7] B. Hague. *The principles of electromagnetism applied to electrical machines.* Dover Publications Inc., New York, 1962.

[8] S. M. Jang, J. Y. Choi, S. H. Lee, S. K. Cho, and W. B. Jang. Analysis of the tubular motor with halbach and radial magnet array. *International Conference on Electrical Machines and Systems*, 1:250–252, 2003.

[9] J. W. Jansen, E. A. Lomonova, A. J. A Vandenput, J. C. Compter, and A. H. Verweij. Improvement of the dynamic performance of an AC linear permanent magnet machine. Madison, New Jersey, U.S.A., 2003.

[10] J. L. G. Janssen, J. J. H. Paulides, E. Lomonova, and A. J. A. Vandenput. Cogging force reduction in tubular permanent magnet actuators. *International Conference on Electrical Machines and Drives*, pages 1–6, 2006.

[11] J.L.G. Janssen. Design of active suspension using electromagnetic devices. Technical report, University of Technology Eindhoven, October 2006.

[12] E. Laurentiu, D. Echeverria, E. Lomonova, A. Vandenput, P. Hemker, and D. Lahaye. Efficient optimal design of electromagnetic actuators using space-mapping. Rio de Janeiro, Brazil, June 2005.

[13] M. Markovic, M. Jufer, and Y. Perriard. Analyzing an electromechanical actuator by Schwarz-Christoffel mapping. *IEEE Transactions on Magnetics*, 40(4):1858–1863, July 2004.

[14] M. Markovic, M. Jufer, and Y. Perriard. Reducing the cogging torque in brushless DC motors by using conformal mappings. *IEEE Transactions on Magnetics*, 40(2):1858–1863, May 2004.

[15] T. C. O'Connell and P. T. Krein. The Schwarz-Christoffel analytical method applied to electric machine slot shape optimization. *International Conference on Electrical Machines and Drives*, pages 341–346, 2-5/5/2007.

[16] T. C. O'Connell and P. T. Krein. A preliminary investigation of computer-aided Schwarz-Christoffel transformation for electric machine design and analysis. *in 10th IEEE Workshop on Computers in Power Electronics*, pages 166–172, 2006.

[17] V. Ostovic. *Dynamics of saturated electric machines.* Springer-Verlag, New York, 1989.

[18] H. Polinder, J. G. Slootweg, M. J. Hoeijmakers, and J. C. Compter. Modelling of a linear PM machine including magnetic saturation and end effects: maximum force to current ratio. *IEEE Transactions on Industry Applications*, 39(6):1858–1863, 2003.

[19] J. Steinbrink. Analytical determination of the cogging torque in brushless motors excited by permanent magnets. *International Conference on Electrical Machines and Drives*, pages 172–177, 2-5/5/2007.

[20] Cedrat Co.. *Flux 9.10 2D and 3D applications. New features.* Meylan, France, 2005.

[21] J. Wang, D. Howe, and Y. Amara. Armature reaction field and inductances of tubular modular permanent magnet machines. *Journal of applied physics*, 97(10Q504):1–3, 2005.

[22] J. Wang, D. Howe, and G. W. Jewell. Analysis and design optimization of an improved axially magnetized tubular permanent-magnet machine. *IEEE Transactions on Energy Conversion*, 19(2):289–295, June 2004.

[23] J. Wang, G. W. Jewell, and D. Howe. Design optimisation and comparison of tubular permanent magnet machine topologies. *IEE Proceedings on Electrical Power Applications*, 148(5):456–464, 2001.

[24] J. Wang, G. W. Jewell, and D. Howe. A general framework for the analysis and design of tubular linear permanent magnet machines. *IEEE Transactions on Magnetics*, 35(3):1986–2000, May 1999.

[25] Z. Q. Zhu and D. Howe. Instantaneous magnetic field distribution in brushless permanent magnet DC motors, part III: Effect of stator slotting. *IEEE Transactions on Magnetics*, 29(1):143–151, 1993.

APPENDIX A MATHEMATICAL IDENTITIES

A.1 Bessel functions

Bessel functions are canonical solutions, $y(x)$, of Bessel's differential equation given by

$$x^2\frac{dy^2}{dx^2} + x\frac{dy}{dx} + (x^2 - a^2)y = 0, \tag{6.1}$$

for arbitrary real or complex a. If a is an integer, then a is called the order of the Bessel function. These Bessel functions are called the Bessel functions of the first kind if they are finite in the origin and can be expressed as

$$\mathcal{B}_{\mathcal{J}a}(x) = \sum_{n=0}^{\infty} \frac{(-1)^n}{n!\Gamma(n+a+1)}\left(\frac{x}{2}\right)^{2n+a}, \tag{6.2}$$

where Γ is the gamma function defined as

$$\Gamma(x) = \int_0^{\infty} t^{x-1}e^{-t}dt. \tag{6.3}$$

If a is an integer, then the following relation is valid

$$\mathcal{B}_{\mathcal{J}-a(x)} = (-1)^a\mathcal{B}_{\mathcal{J}a}(x) \tag{6.4}$$

Bessel functions of the second kind are also a solution of Bessel's differential equation, but they are infinite at the origin and related by $\mathcal{B}_{\mathcal{J}a}(x)$

$$\mathcal{B}_{\mathcal{Y}a}(x) = \frac{\mathcal{B}_{\mathcal{J}a}(x)\cos(a\pi) - \mathcal{B}_{\mathcal{J}-a}(x)}{\sin(a\pi)}, \tag{6.5}$$

and if a is an integer then again the same relation holds

$$\mathcal{B}_{\mathcal{Y}-a(x)} = (-1)^a\mathcal{B}_{\mathcal{Y}a}(x). \tag{6.6}$$

However in this thesis the modified Bessel functions are used which are the solution to Bessel's modified differential equation given by

$$x^2\frac{dy^2}{dx^2} + x\frac{dy}{dx} - (x^2 + a^2)y = 0, \tag{6.7}$$

and the modified Bessel functions of the first kind are related with the Bessel functions of the first kind by

$$\mathcal{B}_{\mathcal{I}a}(x) = i^{-a}\mathcal{B}_{\mathcal{J}a}(ix), \tag{6.8}$$

where i is the complex identity. Again also modified Bessel functions of the second kind exist which are infinite in the origin, and are related with the modified Bessel functions of the first kind by

$$\mathcal{B}_{\mathcal{K}a}(x) = \frac{\pi}{2}\frac{\mathcal{B}_{\mathcal{I}-a}(x) - \mathcal{B}_{\mathcal{I}a}(x)}{\sin(a\pi)}. \tag{6.9}$$

Bessel functions are oscillating functions with a decaying amplitude, modified Bessel functions on the other hand, are exponential increasing or decaying functions. In Fig. 6.1 the ordinary and modified Bessel functions are plotted as function of their argument, x, for a equal to 0, 1 and 2.

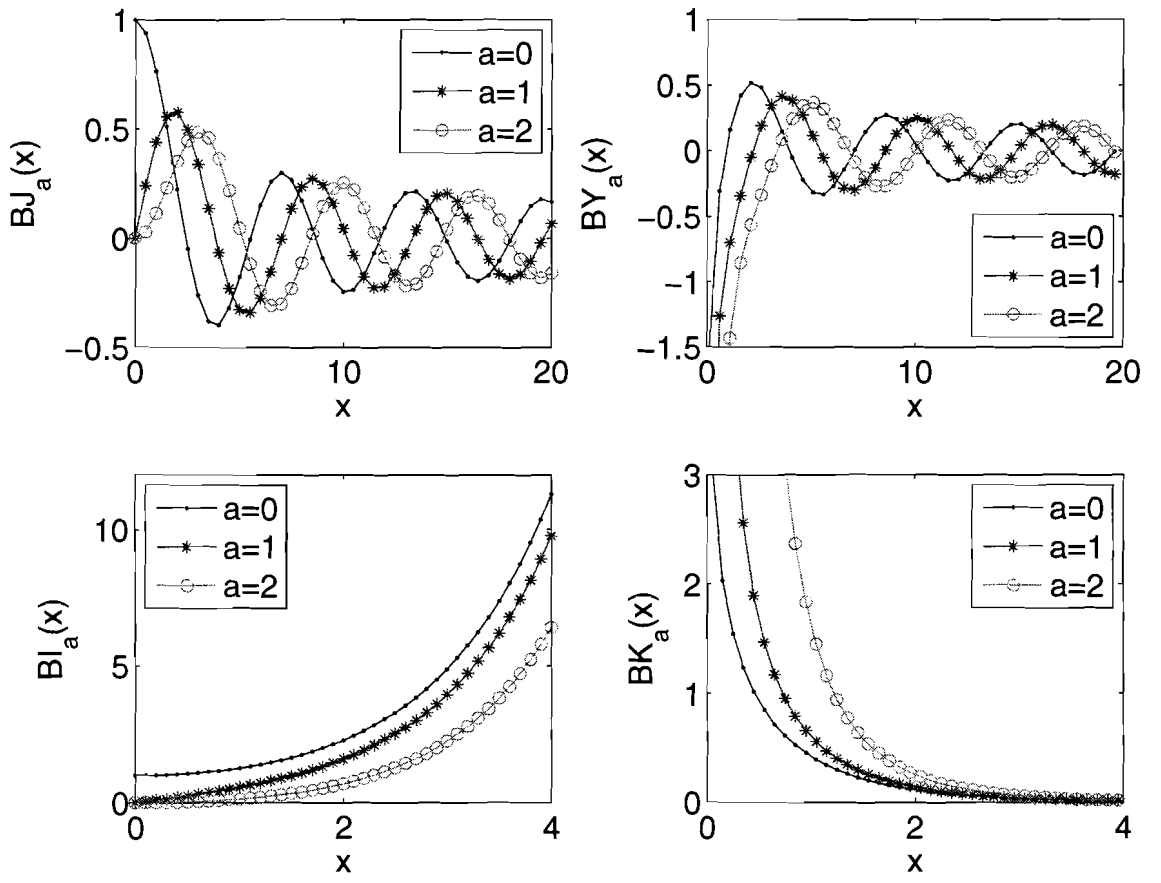

Fig. 6.1: Ordinary and modified Bessel functions of the first and second kind as function of their argument for different orders.

Important identities regarding Bessel functions, which are used throughout this thesis are listed below

- $$\frac{d}{dx}\mathcal{B}_{\mathcal{I}0}(x) = \mathcal{B}_{\mathcal{I}1}(x) \tag{6.10}$$
- $$\frac{d}{dx}\mathcal{B}_{\mathcal{K}0}(x) = -\mathcal{B}_{\mathcal{K}1}(x) \tag{6.11}$$

A.2 Trigonometry

The used trigonometric identities in this thesis are listed below

- $\sin(\alpha) = -\sin(-\alpha)$, (6.12)
- $\cos(\alpha) = \cos(-\alpha)$, (6.13)
- $\sin(\alpha+\beta) = \sin(\alpha)\cos(\beta) + \cos(\alpha)\sin(\beta)$, (6.14)
- $\cos(\alpha+\beta) = \cos(\alpha)\cos(\beta) - \sin(\alpha)\sin(\beta)$, (6.15)
- $\cos(\alpha+\beta) - \cos(\alpha-\beta) = 2\sin(\alpha)\sin(\beta)$, (6.16)
- $\int_{-\pi}^{\pi} \sin(nx+\alpha)\cos(nx+\alpha)dx = 0$, (6.17)
- $\int_{-\pi}^{\pi} \sin(nx+\alpha)\cos\big((n+k)x+\beta\big)dx = \begin{cases} \tau_p \sin(\alpha-\beta) & \text{if } k=0 \\ 0 & \text{if } k\neq 0 \end{cases}$, (6.18)
- $\int_{-\pi}^{\pi} \sin^2(nx+\alpha)dx = \int_{-\pi}^{\pi} \cos^2(nx+\alpha)dx = \pi$, (6.19)
- $\int_{-\pi}^{\pi} \sin(nx+\alpha)\sin\big((n+k)x+\beta\big)dx = \int_{-\pi}^{\pi} \cos(nx+\alpha)\cos\big((n+k)x+\beta\big)dx$
  $= \begin{cases} \tau_p \cos(\alpha-\beta) & \text{if } k=0 \\ 0 & \text{if } k\neq 0 \end{cases}$, (6.20)
- $\int_0^{2\pi} \cos\big(\beta\sin(x)\big)dx = 2\pi\mathcal{B}_{\mathcal{J}_0}(\beta)$, (6.21)
- $\int_0^{2\pi} \sin\big(\beta\sin(x)\big)dx = 0$, (6.22)
- $\int_0^{2\pi} \cos\big(\beta|\sin(x)|\big)dx = 2\pi\mathcal{B}_{\mathcal{J}_0}(\beta)$, (6.23)

for arbitrary variables α and β and arbitrary positive integers n and k.

APPENDIX B. PUBLICATIONS

Analytical and Numerical Techniques for Solving Laplace and Poisson Equations in a Tubular Permanent Magnet Actuator: Part I. Semi-Analytical Framework

B.L.J. Gysen, *Student Member, IEEE*, E.A. Lomonova *Member, IEEE*, J.J.H. Paulides *Member, IEEE*, and A.J.A. Vandenput *Senior Member, IEEE*
Electromechanics and Power Electronics Group
Department of Electrical Engineering
Eindhoven University of Technology
P.O. Box 513, 5600MB, Eindhoven, The Netherlands
Email: B.L.J.Gysen@student.tue.nl

***Abstract*—Analytical and numerical methods are presented for determination of the magnetic field distribution in a tubular permanent magnet actuator (TPMA). First, the semi-analytical method is presented. This method has the advantage of a relatively short computation time and it gives physical insight. Further, an extension is made for skewed topologies, which offer the benefit of reducing the large force ripples of the TPMA. However, a lot of assumptions and simplifications with respect to the slotted structure have to be made in order to come to a relatively simple semi-analytical description. To model the slotting effect and the related cogging force, a Schwarz-Christoffel (SC) mapping is applied for magnetic field and force calculations in Part II of the paper. Validation of the models is done with Finite Element Analysis (FEA).**

I. Introduction

Many numerical and analytical methods exist for analysis, design and optimisation of electrical machines, each with their own strength and pitfalls. The magnetic equivalent circuit (MEC) is widely used because of its simplicity and relative small computation time, [1]–[3]. These equivalent circuits have the analogy of an electrical circuit and are a simplification of the governing quasi-static Maxwell equations

$$\nabla \times \mathbf{E} = -\frac{\partial \mathbf{B}}{\partial t} \quad \Leftrightarrow \quad u_k + e_k = R_k i_k + L_k \frac{\partial i_k}{\partial t}, \qquad (1)$$

$$\nabla \times \mathbf{H} = \mathbf{J} \quad \Leftrightarrow \quad \mathcal{F}_k = \mathcal{R}_k(\Phi_k)\Phi_k. \qquad (2)$$

In general, the simplification (1) in electrical networks is valid since the currents, i_k, are concentrated in wires and the voltages, u_k, e_k, are clearly defined. However, in a magnetic circuit the simplification (2) is not always valid since the flux, Φ_k, does not have predetermined paths due to the slot/tooth structure of the stator and/or translator. The MEC method therefore, needs preliminary knowledge about the flux paths for calculation of the different reluctances, $\mathcal{R}_k$, and the field distribution is only calculated at a few discrete points of the structure, which makes the force calculation very inaccurate. In the case of non-linear ferromagnetic material, the calculation is performed iteratively due to the non-linear reluctances. Finite element analysis (FEA) can be regarded as the most accurate one, because it takes saturation into account and almost no simplification of the actual geometry is needed. But the long computation time makes it sometimes unsuitable for design and optimisation. However, only the initial BH-curve of the materials are taken into account and therefore, hysteresis is neglected.

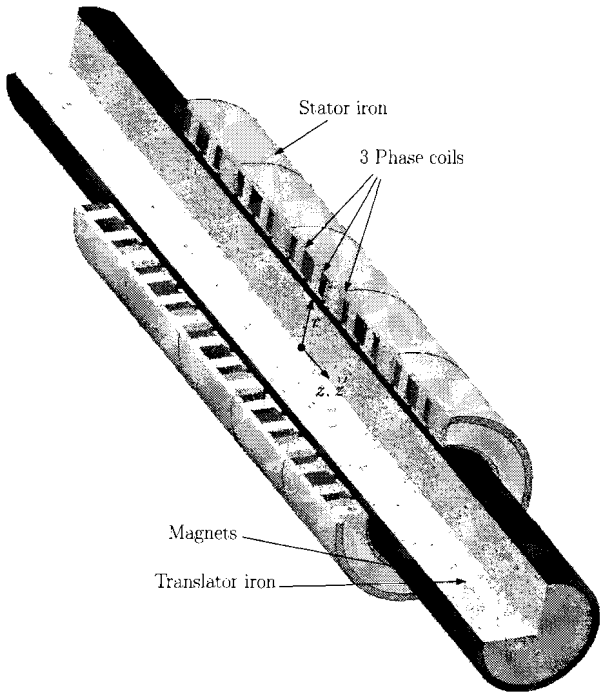

Fig. 1. The tubular permanent magnet actuator.

Schwarz-Christoffel (SC) conformal mapping is a technique which originates from the Riemann mapping theorem (1851), [4], and it is becoming usefull nowadays, due to the com-

putational capabilities of the microprocessors. It states that any simply connected region in the complex plane can be conformally mapped onto any other, provided that neither of these regions spans the entire plane. This method can only handle geometries with a limited number of points but it is able to calculate the field solution numerically at every point within a closed polygon. This method cannot take saturation into account which limits its ability to the linear case. However, the computational time is relatively short compared to the finite element method (FEM). This method is already applied for the various electrical machine types with successfull results, [5]–[7].

The most elegant method for determination of the electromagnetic fields is the analytical solution, which also gives insight into the dependency of the geometry and the material properties on the performance characteristics. The disadvantage of this method is that it only applies to the linear case (no saturation), and a lot of assumptions and simplifications regarding the geometry have to be made.

This paper considers the tubular permanent magnet actuator (TPMA) shown in Fig. 1. It consists of a translator made of iron with surrounding magnets, which are magnetised in positive and negative radial directions alternatively. The inner part of the translator can be made of a non-magnetic material with a low mass density in order to reduce the total mass of the translator. The stator consists of iron slots with a three phase concentrated winding topology. The teeth have saliency in order to reduce the slotting effect. The translator moves in axial direction with a force that consists of four components:

- Mean force caused by the magnetic field of the magnets and the current excitation with the same spatial frequencies,
- Force ripple due to the concentrated winding distribution and higher harmonics in the magnetic field of the magnets,
- Cogging force due to the slotted structure,
- Cogging force due to the finite length of stator and translator.

An undesirable effect of a slotted tubular PM actuator is the apparent cogging force due to the slotted structure and the finite length of the stator. In order to minimise the cogging effect, these effects have to be taken into account by the model that is considered. The MEC model is unsuitable for determing the cogging effect due to the small discretisation of the field distribution. The FEM model can calculate the total cogging but a long computation time is needed. The semi-analytical determination of the end effects is established in [8] but still no exact analytical description of the cogging effect due to the slotted structure is available. The SC-mapping technique however is capable of taking the slotting effect into account and also end effects are possible to include. The main goal is to combine the efforts of the semi-analytical description and the SC-mapping technique in order to calculate the force profile including both cogging effects.

A way of eliminating the apparent force ripple, is by means of skewing of the stator or translator (or both), [9]. This paper describes the semi-analytical description of the skewed topology, neglecting end and slotting effects. Nevertheless,

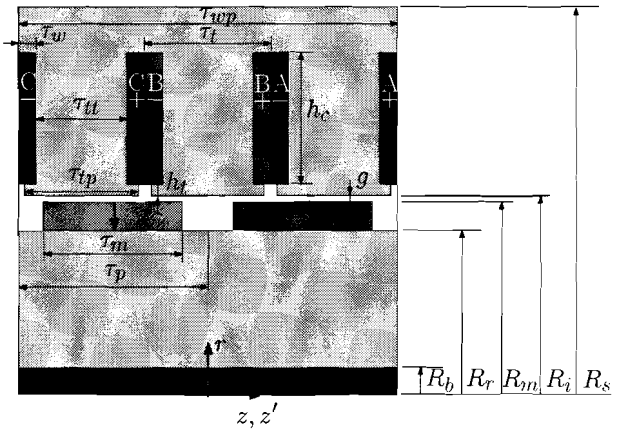

Fig. 2. One pole-pair of the tubular PM actuator with the relevant dimensions.

minimisation of the force ripple due to the winding distribution and minimisation of the total harmonic distortion (THD) on the electro motive force (EMF) is established. The first section derives the semi-analytical description for an unskewed actuator based on the general framework of [10]–[12] and the next section extends these formulas for stator and translator skewing.

II. The semi-analytical framework for an unskewed topology

In Fig. 2, a cross section of one pole-pair of the TPMA is presented. Two axisymmetric coordinate systems are defined, the stator coordinate system, (r, z), and the translator coordinate system, (r, z'), which are related by $z' = z - \Delta_z$, where Δ_z is the relative position of the translator with respect to the stator, which is zero in Fig. 2.

The FEM modelling is done with FLUX 2D, [13], for the full actuator drawn in Fig. 1 with full pitch magnets, $\tau_m = \tau_p$. End effects are thus included in the FEM model. However, in order to make a comparison of the force waveforms without cogging effect, the actuator is also simulated without current. The netto force is then calculated as the total force of the first simulation minus the cogging force, which results from the simulation without current. The mesh for one pole-pair is shown in Fig. 3.

In the semi-analytical framework, only one pole-pair of the actuator is considered with periodical boundary conditions on each side. End effects are thus excluded but can be modelled afterwards [8]. Generally, the electromagnetic analysis concerns three main regions:

- ferromagnetic,
- non-magnetic with a source (coils or magnets),
- empty non-magnetic (air).

Due to the tubular structure, the actuator can be divided into radial regions with the main assumption that the permeability of all the materials is constant for every region. Altough the magnetisation characteristic of the ferromagnetic material is non-linear, no saturation is assumed. Also the configuration of the non-magnetic air gap is changed continiously due to the change of the translator position with respect to the slotted ferromagnetic stator, but under the main assumption no tooth

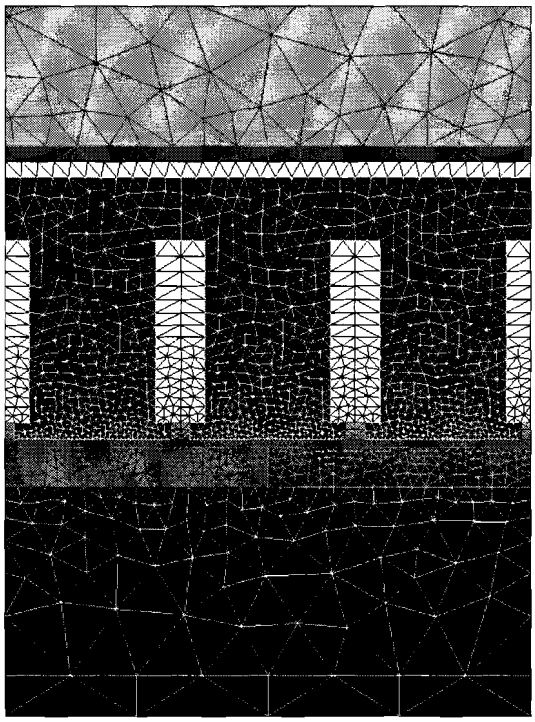

Fig. 3. Mesh distribution of the FE model for one pole-pair of the tubular PM actuator.

effect is included. A Carter's coefficient is often used to scale the fields to account for the leakage flux through the coils, and the fringing fields at the stator teeth, [14]. This coefficient is derived from an empirical formula which is found by the conformal mapping of a general slotted structure. Since salient teeth are considered, the use of a Carter's coefficient is not exact. It only scales the field solution in magnitude but it gives no information about the fringing effect which exists at the teeth tips, and therefore no cogging force can be calculated with the use of this coefficient.

The magnetic fields can be solved in terms of the magnetic vector potential, $\mathbf{A}$, or the scalar potential, φ, [15]. However, since it is a two-dimensional problem, the magnetic vector potential has only one component in the direction of symmetry and can be treated as a scalar potential. The magnetostatic Maxwell equations reduce to a Poisson equation in terms of the magnetic vector potential is given by

$$\nabla^2 \mathbf{A} = -\mu_0(\mathbf{J} + \nabla \times \mathbf{M}), \tag{3}$$

where $-\mu_0(\mathbf{J} + \nabla \times \mathbf{M})$ is the source term depending on the spatial variables, $(r, z$ in this case), and time with $\mathbf{J}$ the current density vector ans $\mathbf{M}$ the magnetisation vector of the magnets. For a source free region, the Poisson equation reduces to a Laplace equation, $\nabla^2 \mathbf{A} = \mathbf{0}$. The Laplace and Poisson equations are solved for every region of interest. The complexity of the semi-analytical description increases with the number of boundary conditions that is considered and thereby also with the number of regions. Therefore, assumptions have to be made, which restrict the number of regions. The fields are solved for the magnets and the stator coils as field sources seperately. Since only linear materials are

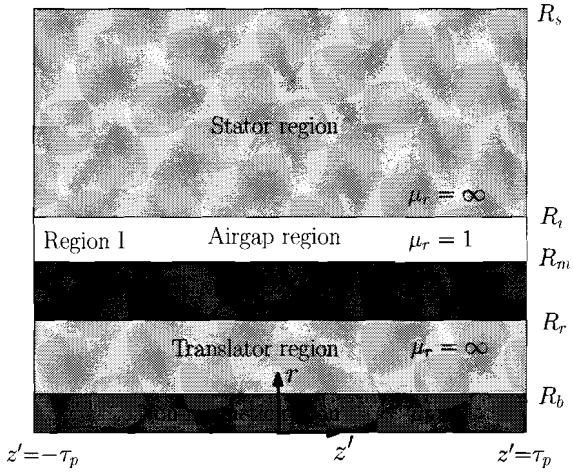

Fig. 4. Division in radial regions of one pole-pair of the tubular PM actuator for calculation of the fields due to the magnets.

considered, the superposition principle is applied to calculate the total magnetic field solution.

A. Magnetic field of the magnets

In Fig. 4 the division in radial regions of one pole-pair of the TPMA is shown. For calculation of the magnetic fields caused by the permanent magnets, the iron is assumed infinitely permeable. This reduces the problem to only two regions, the airgap and the magnet region. The non-magnetic region is isolated from any magnetic behaviour since all the field sources lie in between two regions with infinite permeability. The Laplace and Poisson equations in terms of the magnetic vector potential in both regions are given by

$$\nabla^2 \mathbf{A}_{\mathrm{I}} = \mathbf{0}, \tag{4}$$

$$\nabla^2 \mathbf{A}_{\mathrm{II}} = -\mu_0 \nabla \times \mathbf{M}, \tag{5}$$

where $\mathbf{A}$ has only a component in the θ-direction which is independent of θ due to the axial symmetry, $\mathbf{A} = A_\theta(r, z)\mathbf{e}_\theta$, with $\mathbf{e}_\theta$ the unit vector in the θ-direction. If the coordinate system, (r, z'), indicated in Fig. 4 is considered, then the magnetisation vector, $\mathbf{M}$, can be described as

$$\mathbf{M} = M_r \mathbf{e}_r = \sum_{n=1}^{\infty} M_n \sin(m_n z')\mathbf{e}_r, \tag{6}$$

$$M_n = \frac{2B_{rem}}{\mu_0} \frac{1 - \cos(n\pi)}{n\pi} \cos\left(\frac{n\pi(1-\alpha_p)}{2}\right), \tag{7}$$

$$m_n = \frac{n\pi}{\tau_p}, \tag{8}$$

where $\mathbf{e}_r$ is the unit vector in the r-direction, m_n are the spatial harmonics and B_{rem} is the remanent flux density of the magnets. The Laplace and Poisson equations, (4) and (5), are solved by seperation of variables since it is a two-dimensional case. In case of a three-dimensional problem, seperation of variables is not always possible, [16]. The magnetic flux density $\mathbf{B}$ is derived from $\mathbf{A}$ as

$$\mathbf{B} = \nabla \times \mathbf{A} = -\frac{\partial A_\theta}{\partial z'}\mathbf{e}_r + \frac{\partial}{r\partial r}(rA_\theta)\mathbf{e}_{z'}, \tag{9}$$

with $\mathbf{e}_{z'} = \mathbf{e}_z$ the unit vector in the axial direction. The boundary conditions of regions I and II are given by

$$\begin{aligned} B_{\mathrm{I}_{z'}}|_{r=R_i} &= 0, && (10)\\ B_{\mathrm{II}_{z'}}|_{r=R_r} &= 0, && (11)\\ B_{\mathrm{I}_r}|_{r=R_m} &= B_{\mathrm{II}_r}|_{r=R_m}, && (12)\\ H_{\mathrm{I}_{z'}}|_{r=R_m} &= H_{\mathrm{II}_{z'}}|_{r=R_m}. && (13) \end{aligned}$$

This gives for the magnetic flux densities in regions I and II as

$$\begin{aligned} B_{\mathrm{I}_r} &= -\sum_{n=1}^{\infty}\Big(a_{1n}\mathcal{B}_{\mathcal{I}1}(m_n r) + b_{1n}\mathcal{B}_{\mathcal{K}1}(m_n r)\Big)\sin(m_n z'),\\ B_{\mathrm{I}_{z'}} &= -\sum_{n=1}^{\infty}\Big(a_{1n}\mathcal{B}_{\mathcal{I}0}(m_n r) - b_{1n}\mathcal{B}_{\mathcal{K}0}(m_n r)\Big)\cos(m_n z'),\\ B_{\mathrm{II}_r} &= -\sum_{n=1}^{\infty}\Big\{\Big(\mathcal{K}_{an}(m_n r) + a_{2n}\Big)\mathcal{B}_{\mathcal{I}1}(m_n r)\\ &\quad -\Big(\mathcal{K}_{bn}(m_n r) - b_{2n}\Big)\mathcal{B}_{\mathcal{K}1}(m_n r)\Big\}\sin(m_n z'),\\ B_{\mathrm{II}_{z'}} &= -\sum_{n=1}^{\infty}\Big\{\Big(\mathcal{K}_{an}(m_n r) + a_{2n}\Big)\mathcal{B}_{\mathcal{I}0}(m_n r)\\ &\quad +\Big(\mathcal{K}_{bn}(m_n r) - b_{2n}\Big)\mathcal{B}_{\mathcal{K}0}(m_n r)\Big\}\cos(m_n z'), \quad (14) \end{aligned}$$

where $\mathcal{B}_{\mathcal{I}o}$ and $\mathcal{B}_{\mathcal{K}o}$ are modified bessel functions of the first and second kind of the o^{th} order respectively, and a_{1n}, b_{1n}, a_{2n} and b_{2n} are derived from the boundary conditions and given in Appendix B together with the functions of $\mathcal{K}_{an}$ and $\mathcal{K}_{bn}$. The field is calculated in the center of the air gap, $R_{ag} = \frac{R_m+R_i}{2}$, for the dimensions given in Table II, the material properties in Table III in Appendix A, and for n up to 50, since higher harmonics have an influence of less then 1%. Verification with the FEM is shown in Fig. 5. Good agreement is achieved with the FEM calculation, the only difference is the slotting effect, which is clearly visible at the positions of the coils.

B. Field due to the stator coils

For calculation of the fields due to the stator coils, the iron is again assumed infinitely permeable which again eliminates three regions. Furthermore, since only the magnetic field of the stator coils is considered, the magnets are modelled as an air region, which is an acceptable assumption if μ_r is almost equal to 1, which is true for rare-earth permanent magnets. This results in only one region which consists of the air gap and magnet region of previous section, called as region III, Fig. 6. Note that the coordinate system is now changed to (r, z). The coils are modelled by a surface current density sheet distribution, J_s, at the stator bore, R_i. The description of J_s consists of two parts for every phase, one is dependent on z (winding distribution), K_w, and the other is dependent on Δ_z (commutation), J_A, J_B and J_C. Thus, for a three phase winding distribution this gives

$$J_s = J_A K_{w_A} + J_B K_{w_B} + J_C K_{w_C}, \quad (15)$$

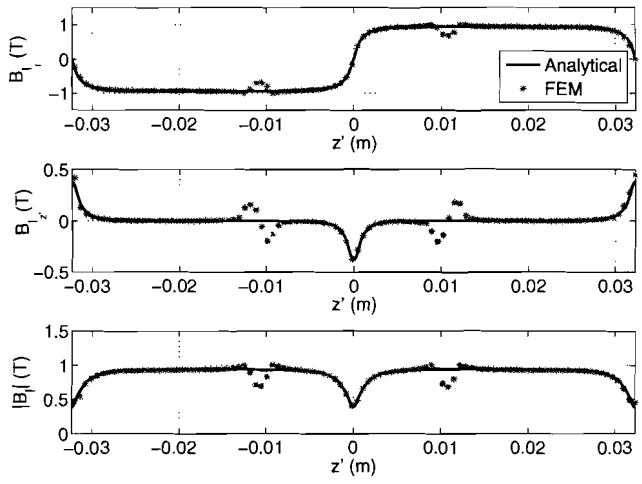

Fig. 5. Field distribution in the air gap due to the magnets for $\Delta_z = 0$.

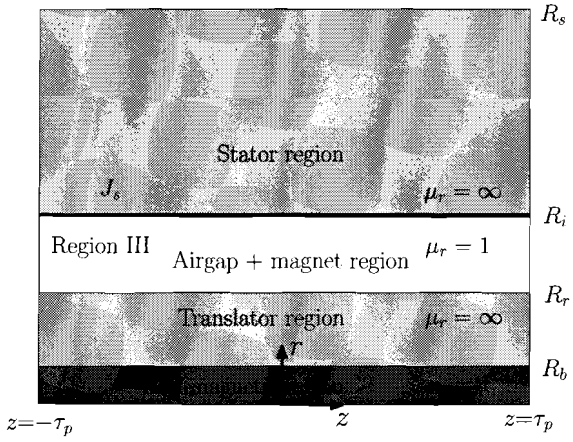

Fig. 6. Division in radial regions for one pole-pair of the tubular PM actuator for calculation of the fields due to the stator coils.

where K_{w_A}, K_{w_B} and K_{w_C} can be described as a Fourier series

$$\begin{aligned} K_{w_A}(z) &= \sum_{n=1}^{\infty} K_{w_n}\sin\Big(m_n(z-\tau_t)\Big),\\ K_{w_B}(z) &= \sum_{n=1}^{\infty} K_{w_n}\sin\Big(m_n z\Big),\\ K_{w_C}(z) &= \sum_{n=1}^{\infty} K_{w_n}\sin\Big(m_n(z+\tau_t)\Big). \quad (16) \end{aligned}$$

Care must be taken when describing K_{w_n} for salient poles. Only the part of the coil which is situated outside the teeth has to be mapped onto a current sheet in order to model the saliency of the slots, see illustration in Fig. 7.

This means that the width of the current sheets is not equal to the width of the coils, τ_w, but equal to $\tau_{ws} = \frac{\tau_t - \tau_{tp}}{2}$, where τ_t is the tooth pitch and τ_{tp} is the width of the tooth tip. Therefore, the amplitude of the surface current density has to be corrected with a factor, $\frac{\tau_w}{\tau_{ws}}$. The winding distribution is

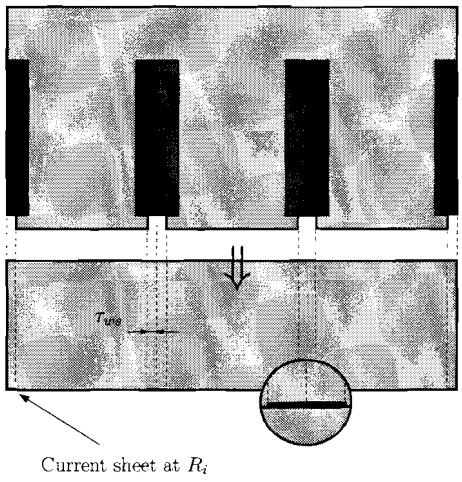

Fig. 7. Mapping of the coils onto a current sheet for salient poles.

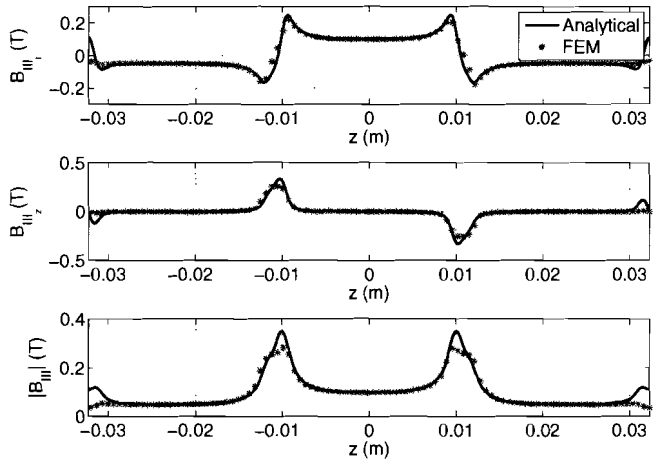

Fig. 8. Field distribution in the air gap due to the stator coils for $\Delta_z = 0$.

discribed as a Fourier series given by

$$K_{w_n} = \frac{2}{\pi n}\left\{ \cos\left(\frac{n\pi}{3}\right) - \cos\left(\frac{n\pi}{3}(1 - \frac{3\tau_{ws}}{\tau_p})\right)\right\}. \quad (17)$$

The commutated surface current densities for a three phase sinusoidal excitation are given by (with reference to the proposed coordinate system)

$$\begin{aligned} J_A &= J_0 \frac{h_c \tau_w}{\tau_{ws}} \cos\left(\frac{\pi\Delta_z}{\tau_p} - \frac{2\pi}{3}\right), \\ J_B &= J_0 \frac{h_c \tau_w}{\tau_{ws}} \cos\left(\frac{\pi\Delta_z}{\tau_p}\right), \\ J_C &= J_0 \frac{h_c \tau_w}{\tau_{ws}} \cos\left(\frac{\pi\Delta_z}{\tau_p} + \frac{2\pi}{3}\right), \end{aligned} \quad (18)$$

and for a three phase rectangular excitation, these surface current densities become

$$J_A = J_0 \sum_{k=1}^{\infty} K_{i_k} \cos\left(k\left(\frac{\pi\Delta_z}{\tau_p} - \frac{2\pi}{3}\right)\right), \quad (19)$$

$$J_B = J_0 \sum_{k=1}^{\infty} K_{i_k} \cos\left(k\left(\frac{\pi\Delta_z}{\tau_p}\right)\right), \quad (20)$$

$$J_C = J_0 \sum_{k=1}^{\infty} K_{i_k} \cos\left(k\left(\frac{\pi\Delta_z}{\tau_p} + \frac{2\pi}{3}\right)\right), \quad (21)$$

where K_{i_k} is given by

$$K_{i_k} = \frac{2}{k\pi}\Big(\sin(k\pi/3) + \sin(2k\pi/3)\Big). \quad (22)$$

The variable, k, is used instead of n since both will appear in the force calculation and distinction has to made between both summations. Since the total surface current sheet distribution is given, the field equation in terms of the magnetic vector potential in region III, is given by a Laplace equation

$$\nabla^2 \mathbf{A}_{\mathrm{III}} = \mathbf{0}, \quad (23)$$

since there are no sources inside region III and can be solved subject to the boundary conditions

$$\begin{aligned} B_{\mathrm{III}_z}(R_i, z) &= \mu_0 J_s, \\ B_{\mathrm{III}_z}(R_r, z) &= 0, \end{aligned} \quad (24)$$

which results for the magnetic field of the stator currents of phase B described as

$$\begin{aligned} B_{\mathrm{III}_{B_r}} &= -\mu_0 J_B \sum_{n=1}^{\infty} \frac{K_{w_n}}{(c_{4_n} c_{1_n} - c_{2_n} c_{3_n})} \\ &\quad \Big\{ c_{4_n} \mathcal{B}_{\mathcal{I}1}(m_n r) + c_{3_n} \mathcal{B}_{K1}(m_n r) \Big\} \cos(m_n z), \\ B_{\mathrm{III}_{B_z}} &= \mu_0 J_B \sum_{n=1}^{\infty} \frac{K_{w_n}}{(c_{4_n} c_{1_n} - c_{2_n} c_{3_n})} \\ &\quad \Big\{ c_{4_n} \mathcal{B}_{\mathcal{I}0}(m_n r) - c_{3_n} \mathcal{B}_{K0}(m_n r) \Big\} \sin(m_n z), \end{aligned} \quad (25)$$

where the coefficients, $c_{1_n}..c_{4_n}$, are given in Appendix B, and the expressions for phases A and C are similar, replacing z by $z - \tau_t$ and $z + \tau_t$, and J_B by J_A and J_C, respectively. The total field due to the stator coils is calculated by superposition of the fields of the different phases. The solution is verified with the FEM and the results are shown in Fig. 8. Again a good agreement has been found, however a relatively large error is obtained at the sides, at coil A positive and C negative. At this position, $\Delta_z = 0$, the current density is equal but opposite in those coils, introducing a fluctuation of the magnetic field in the semi-analytical solution seen in Fig. 8. However, in the FE solution this fluctuation is much smaller since the coils are not as close to the air gap as the current sheets of the semi-analytical model. Also the current is more concentrated in the semi-analytical framework. This leads to an error in the field solution due to the current sheet modelling.

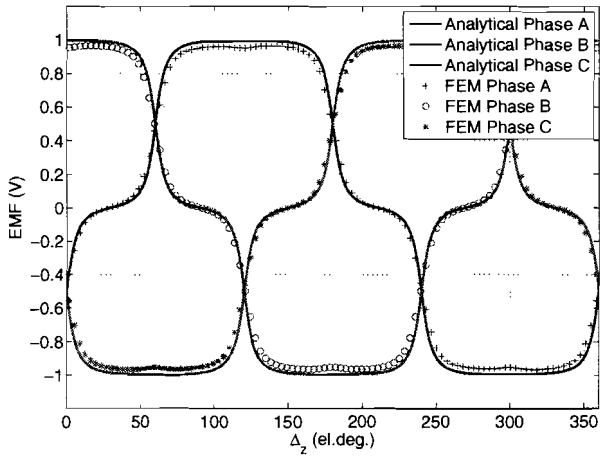

Fig. 9. Electromotive force for a speed of 0.5 m/s for 360 electrical degrees.

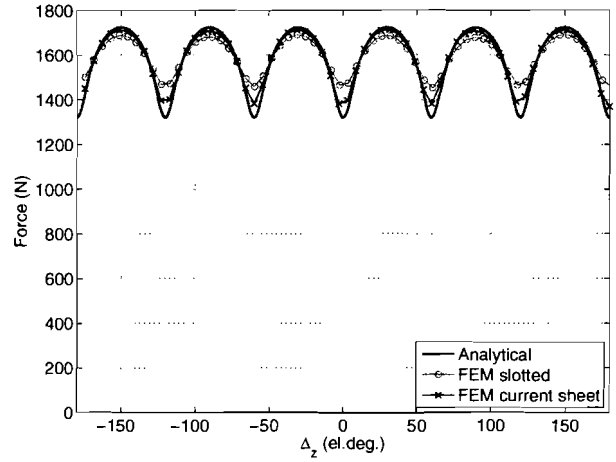

Fig. 10. Force as function of displacement for 360 electrical degrees.

C. EMF calculation

The flux linkage, Ψ, imposed by every phase, is approximately the amount of radial flux due to the magnets imposed by the corresponding teeth at the inner radius of the stator, R_i, given by

$$\Psi = 2\pi R_i N N_{sp} \int_{-\frac{\tau_t}{2}+D}^{\frac{\tau_t}{2}+D} B_{\mathrm{I}_r}(R_i, z')dz,$$

where D is equal to τ_t, 0 or $-\tau_t$ for phases A, B or C, respectively, and N_{sp} is the number of slots per phase. Calculation of the EMF as

$$e = -\frac{\partial \Psi}{\partial t} = -\frac{\partial \Psi}{\partial \Delta_z}\frac{\partial \Delta_z}{\partial t} = -\frac{\partial \Psi}{\partial \Delta_z} v, \tag{26}$$

gives

$$e = -4\pi R_i v N N_{sp} \sum_{n=1}^{\infty} \left(a_{1n}\mathcal{B}_{\mathcal{I}1}(m_n R_i) + b_{1n}\mathcal{B}_{\mathcal{K}1}(m_n R_i) \right) \sin\left(\frac{n\pi}{3}\right) \cos\left(m_n(D - \Delta_z)\right). \tag{27}$$

Evaluation and verification with the FEM is shown in Fig. 9. It can be observed that acceptable agreement is achieved. The FE calculation has a lower amplitude since leakage flux through the coils is not modelled in the semi-analytical model.

D. Force calculation

The force calculation is performed by use of the Maxwell Stress Tensor, [15], calculated on a surface bounded by the translator where the axial length is equal to the length of one pole-pair (since boundary conditions are applied), and the total force is obtained by multiplying with the number of pole-pairs, N_p,

$$F = \frac{N_p}{\mu_0} \oint_S \mathbb{T}.\mathbf{n} dS, \tag{28}$$

where $\mathbf{n}$ is the normal vector on the surface S and the tensor is defined as

$$\mathbb{T} = \begin{bmatrix} B_r^2 - \frac{|B|^2}{2} & B_r B_\theta & B_r B_z \\ B_\theta B_r & B_\theta^2 - \frac{|B|^2}{2} & B_\theta B_z \\ B_z B_r & B_z B_\theta & B_z^2 - \frac{|B|^2}{2} \end{bmatrix}, \tag{29}$$

where B_r, B_θ and B_z are the total radial, angular and axial magnetic field at the surface S, respectively. The closed surface, S, is defined by the areas S_1: $z = -\tau_p$, S_2: $z = \tau_p$ and S_3: $r = R_{ag}$. Since the end effects are neglected, S_1 and S_2 have periodical boundary conditions, and therefore the evaluation of (28) on both surfaces is equal, but since the normal vectors of both surfaces are in opposite direction, their total contribution is zero. Therefore, the integral is only evaluated on surface, S_3, which results in

$$F_z = \frac{2\pi R_{ag} N_p}{\mu_0} \int_{-\tau_p}^{\tau_p} (B_{\mathrm{I}_r} + B_{\mathrm{III}_r})(B_{\mathrm{I}_z} + B_{\mathrm{III}_z}) dz \Big|_{r=R_{ag}}, \tag{30}$$

evaluation of this integral leads to

$$F_z = \pi R_{ag} L_{ax} \sum_{n=1}^{\infty} K_{w_n} C_n \Big[J_A \cos\left(m_n(\Delta_z - \tau_t)\right) + J_B \cos\left(m_n \Delta_z\right) + J_C \cos\left(m_n(\Delta_z + \tau_t)\right) \Big], \tag{31}$$

where $L_{ax} = 2N_p\tau_p$ is the active axial length of the translator and C_n is given in Appendix B.

The force is calculated for a displacement of 360 electrical degrees ($\Delta_z = 0...2\tau_p$) with sinusoidal excitation with a current density of $J_0 = 7.5$ A/mm^2 and verified with the FEM model of the actual actuator and the FEM model where the stator is modelled with surface current sheets. The solutions are shown in Fig. 10.

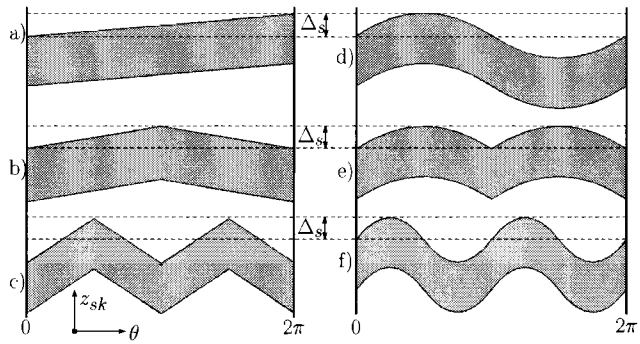

Fig. 11. Possible skewing topologies. The skewing amplitude is indicated by Δ_s.

Comparison of the semi-analytical solution with the FEM model of the surface current sheets gives a very good agreement. However, comparison of the semi-analytical solution with the slotted FEM model introduces an error in the sixth harmonic, which is due to the current sheet modelling error as explained in section B. But in any case, the DC value is calculated within 1 percent.

III. The Semi-Analytical Framework for Skewed Topologies

In this section, the semi-analytical formulas of the previous section will be adapted for skewed topologies. The distinction will be made between stator and translator skewing, since there is a small difference in the force calculation.

A. Skewing transformation

For unskewed topologies the actuator can be described in the (r, z)-plane due to the axisymmetry. If skewing is applied, the axisymmetry is lost and the problem becomes a three-dimensional one. However, skewing is nothing more then a shift of the z-axis dependent on θ. Thus, consider

$$z_{sk} = z + \mathcal{S}(\theta), \tag{32}$$

where $\mathcal{S}(\theta)$ is defined as the skewing transformation. Different skewing topologies are shown in Fig. 11 and the corresponding skewing transformations are

- Linear (a):
  $\mathcal{S}(\theta) = \frac{\Delta_s \theta}{2\pi}$,
- Triangular (b), (c):
  $\mathcal{S}(\theta) = \begin{cases} \frac{p\Delta_s\theta}{\pi} - kp\Delta_s & \frac{k2\pi}{p} < \theta < \frac{(2k+1)\pi}{p} \\ \frac{-p\Delta_s\theta}{\pi} + (k+1)p\Delta_s & \frac{(k+1)\pi}{p} < \theta < \frac{2(k+1)\pi}{p} \end{cases}$
  for $k = 0...(p-1)$,
- Sinusoidal (d), (f):
  $\mathcal{S}(\theta) = \Delta_s \sin(p\theta)$,
- Half Sinusoidal (e):
  $\mathcal{S}(\theta) = \Delta_s |\sin(p\theta)|$,

TABLE I
Coefficients T_{c_n} and T_{s_n} for different skewing topologies.

	T_{c_n}	T_{s_n}
Linear	$\frac{2\pi}{m_n\Delta_s}\sin(m_n\Delta_s)$	$\frac{2\pi}{m_n\Delta_s}\left(1-\cos(m_n\Delta_s)\right)$
Triangular	$\frac{2\pi}{m_n\Delta_s}\sin(m_n\Delta_s)$	0
Sinusoidal	$2\pi\mathcal{B}_{\mathcal{J}0}(m_n\Delta_s)$	0
Half sinusoidal	$2\pi\mathcal{B}_{\mathcal{J}0}(m_n\Delta_s)$	$2\int_0^\pi \sin\left(m_n\Delta_s\sin(\theta)\right)d\theta$

where p is the number of repetitions and Δ_s is the skewing amplitude. Thus, with this transformation, it is possible to use the equations derived for the unskewed actuator, where z is replaced by z_{sk} according to (32).

B. EMF calculation

The EMF waveform of a skewed actuator for stator or translator skewing is the same, therefore no distinction has to be made. Consider again the flux linkage imposed by every phase (26) but now the skewing transformation is applied. Since the axisymmetry is lost, an integration over θ is also necessary

$$\Psi = R_i N N_{sp} \int_0^{2\pi} \int_{-\frac{\tau_t}{2}+D}^{\frac{\tau_t}{2}+D} B_{\mathrm{I}_r}\left(R_i, z' + \mathcal{S}(\theta)\right) dz d\theta. \tag{33}$$

Evaluation of the EMF by (26) gives

$$e = -4\pi R_i v N N_{sp} \sum_{n=1}^{\infty} \left(a_{1n}\mathcal{B}_{\mathcal{I}1}(m_n R_i) + b_{1n}\mathcal{B}_{\mathcal{K}1}(m_n R_i)\right) \sin\left(\frac{n\pi}{3}\right) \left[T_{c_n}\cos\left(m_n(D-\Delta_z)\right) + T_{s_n}\sin\left(m_n(D-\Delta_z)\right)\right], \tag{34}$$

where T_{c_n} and T_{s_n} are defined as

$$T_{c_n} = \int_0^{2\pi} \cos\left(m_n\mathcal{S}(\theta)\right) d\theta, \tag{35}$$

$$T_{s_n} = \int_0^{2\pi} \sin\left(m_n\mathcal{S}(\theta)\right) d\theta, \tag{36}$$

where these integrals are evaluated (if possible) in Table I for the different skewing topologies that are considered.

If, for example, sinusoidal skewing is considered, then the only difference between (27) and (34) is a factor $\mathcal{B}_{\mathcal{J}0}(m_n\Delta_s)$ for every n. Note that the number of periods, p, does not influence the EMF waveform.

C. Force calculation

There is a difference in the force level when translator or stator skewing is considered. To explain this in a clear way, let us consider only the Lorentz force density, $\mathbf{f} = \mathbf{J} \times \mathbf{B}$, where $\mathbf{B}$ consists predominantly of the radial field of the magnets. Therefore, by approximation the Lorentz force density is given

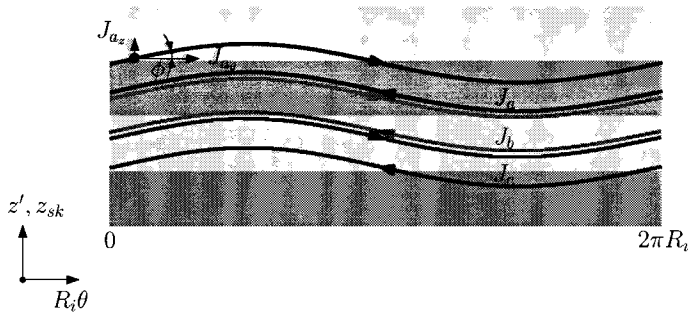

Fig. 12. Illustration of the different current density components for stator skewing.

by $f_z = J_s B_{I_r}$. If translator skewing is considered, then B_{I_r} does not change in direction and the two vectors **J** and **B** are still orthogonal. If, however, stator skewing is considered, the θ-component of the current density vector **J** decreases and an extra component in the z-direction exists, which does not contribute to axial thrust. Therefore, in general, the force level will be slightly lower for stator skewing then for translator skewing depending on the skewing amplitude, Δ_s.

1) Translator skewing: If translator skewing is considered, the magnets are skewed according to the skewing transformation. The magnetic field of the magnets undergoes a transformation, which is dependent on θ. The evaluation of the force by means of the Maxwell Stress Tensor is therefore changed to

$$F_z = \frac{R_{ag} N_p}{\mu_0} \int_0^{2\pi} \int_{-\tau_p}^{\tau_p} (B_{\mathrm{I}_r} + B_{\mathrm{III}_r})(B_{\mathrm{I}_z} + B_{\mathrm{III}_z}) dz d\theta \Big|_{r=R_{ag}}, \tag{37}$$

where the skewing transformation is applied to B_{I_r} and B_{I_z}. Again the force equation becomes similar to (31) but with an extra factor, T_{c_n}, for the cosine terms and additional sine terms with an extra factor, T_{s_n},

$$\begin{aligned} F_z = R_{ag} \frac{L_{ax}}{2} \sum_{n=1}^{\infty} K_{w_n} C_n \Bigg[& T_{c_n} \Big\{ J_A \cos\Big(m_n(\Delta_z - \tau_t)\Big) \\ & + J_B \cos\Big(m_n \Delta_z\Big) + J_C \cos\Big(m_n(\Delta_z + \tau_t)\Big) \Big\} \\ & + T_{s_n} \Big\{ J_A \sin\Big(m_n(\Delta_z - \tau_t)\Big) \\ & + J_B \sin\Big(m_n \Delta_z\Big) + J_C \sin\Big(m_n(\Delta_z + \tau_t)\Big) \Big\} \Bigg]. \end{aligned} \tag{38}$$

2) Stator skewing: The calculation of the field due to the stator currents, B_{III}, is based upon a surface current density distribution in the θ-direction. When stator skewing is applied, the current density distribution also has an axial direction and therefore, for the same amount of current density, the θ-component decreases. This is illustrated in Fig. 12. The surface current density distribution, J_s, used in the formulas of B_{III}, has to be corrected by a factor, $\cos(\phi)$, where ϕ can be derived

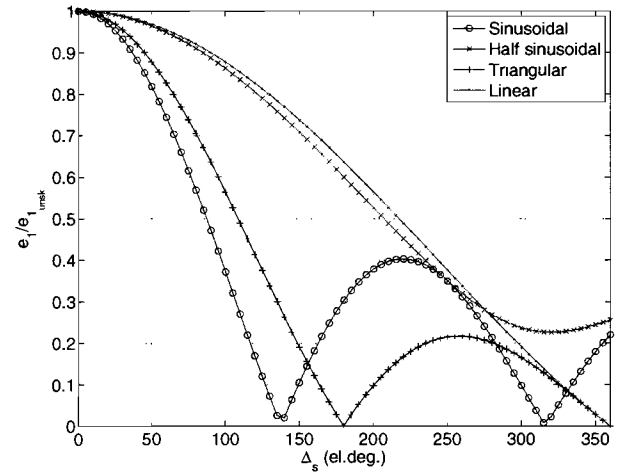

Fig. 13. Normalised first harmonic of the EMF-waveform for different skewing topologies.

from Fig. 12 as

$$\phi = \arctan\left(\frac{1}{R_i}\frac{\partial \mathcal{S}(\theta)}{\partial \theta}\right). \tag{39}$$

If (37) is applied, (38) still holds, but T_{c_n} and T_{s_n} change to

$$\begin{aligned} T_{c_n} &= \int_0^{2\pi} \cos\left(\arctan\left(\frac{1}{R_i}\frac{d\mathcal{S}(\theta)}{d\theta}\right)\right) \cos\big(m_n \mathcal{S}(\theta)\big) d\theta, \\ T_{s_n} &= \int_0^{2\pi} \cos\left(\arctan\left(\frac{1}{R_i}\frac{d\mathcal{S}(\theta)}{d\theta}\right)\right) \sin\big(m_n \mathcal{S}(\theta)\big) d\theta, \end{aligned} \tag{40}$$

which are difficult, if not impossible, to solve analytically, and in this case these integrals are solved numerically.

D. Dependency on the skewing amplitude, Δ_s

The reason to apply skewing is to reduce the cogging effect, the force ripple due to the winding distribution and the harmonics of the magnetic field of the magnets, and the THD of the EMF waveform, $\mathrm{THD_e}$. A disadvantage of skewing is that not only the higher harmonics decrease, but also the fundamental and subharmonics of the magnetic field, which contribute to the mean value of the force, decrease. A compromise has to be made between the amount of harmonic content and the amplitude of the fundamental of the EMF waveform, e_1. In Fig. 13, the amplitude of the fundamental of the EMF waveform, e_1, normalised on the amplitude of the fundamental of the unskewed waveform, $e_{1_{\mathrm{unsk}}}$, is plotted as a function of the skewing amplitude for different skewing topologies.

The result is quite understandable, if, for example, triangular skewing is considered, then it is obvious that for a skewing amplitude of 180 el.deg. (or 360 el.deg.), e_1 drops to zero since every slot of the stator links as much positive flux as negative flux, and the total flux linkage is always zero. For linear skewing this happens at 360 el.deg.

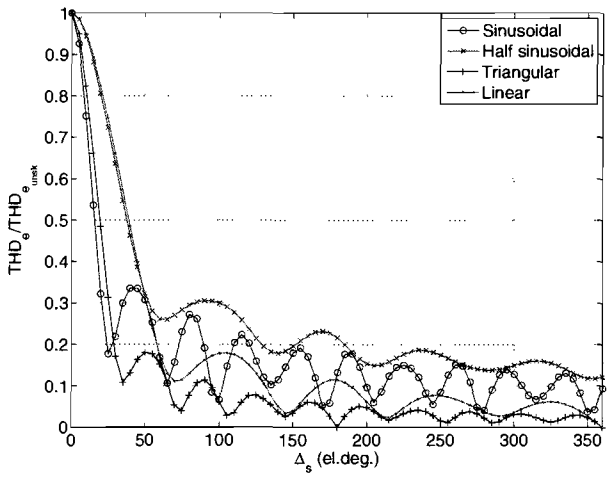

Fig. 14. Normalised THD of the EMF-waveform for different skewing topologies.

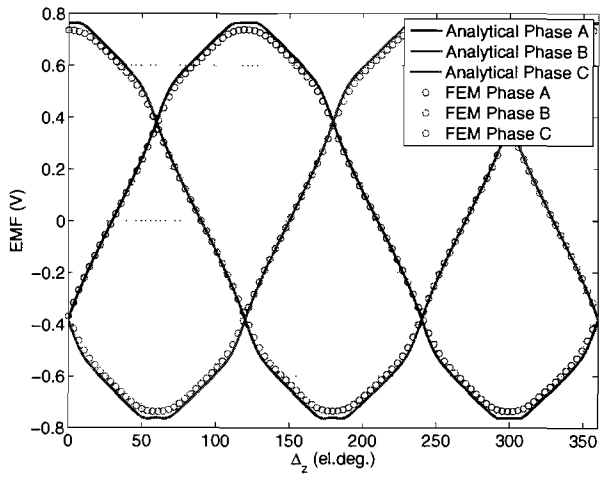

Fig. 15. EMF waveform for sinusoidal skewing with $\Delta_s = 65°$E.

Furthermore, the THD_e normalised on the $\text{THD}_{e_{\text{unsk}}}$ of the unskewed actuator is plotted as function of the skewing amplitude for different skewing topologies in Fig. 14. It can be seen that the THD_e drops much faster then e_1, which means that the THD_e can be decreased drastically without loosing much performance. If, for example, the first suboptimal skewing amplitude of 25 electrical degrees of the sinusoidal skewing is considered, then e_1 is only decreased with 6%, whereas the THD_e is decreased with 82%. In order to verify the semi-analytical framework for skewed topologies, a FEM calculation could be performed for the skewed actuator. In order to avoid a complex three-dimensional FEM model, an overlay and add method is used on the unskewed waveform, which is a MATLAB script that basically applies (41)

$$e_{\text{sk}}(\Delta_z) = \frac{1}{N_\theta}\sum_{n=1}^{N_\theta} e_{\text{unsk}}\left(\Delta_z + \mathcal{S}\left(\frac{n2\pi}{N_\theta}\right)\right). \qquad (41)$$

where N_θ is the number of divisions in the θ-direction and e_{unsk} is the FE solution of the unskewed EMF waveform. This is exactly how the FLUX software, [13], internally calculates linear skewing applied to rotary machines. In Fig. 15, the EMF waveform is plotted for sinusoidal skewing of 65 el.deg. together with the FEM overlay and add solution, in this case e_1 is decreased with 30% and the THD_e is decreased with 90%.

The same thing can be done for the force waveform but similar results are found since the coefficients, T_{c_n} and T_{s_n}, are the same for the force and EMF calculation for a given skewing topology. The only difference is a lower DC level of the force for stator skewing, depending on the skewing amplitude.

IV. Conclusion

Semi-analytical expressions for the magnetic field distribution inside the air gap of a tubular PM actuator are derived. From these expressions the force and EMF waveforms are calculated and verified with FEM. Good agreement has been found but the slotting effect cannot be incorporated in a straightforward way. The semi-analytical framework has been extended for skewed topologies, and it has been shown that the formulas for the unskewed topology still hold and only an extra correction factor is needed to describe the effect of skewing for translator and stator skewing, respectively. With this semi-analytical framework an optimisation can be performed in order to find the optimal skewing topology and skewing amplitude for minimisation of the THD of the EMF waveform depending on the application and to reduce the force ripple which results from the winding distribution and the harmonics of the magnetic field of the magnets.

Appendix A

TABLE II
Dimensions and Parameters of the Tubular Actuator

Dimension	Value	Description
h_{bi}	7.8 mm	Height of the back iron
h_c	22.5 mm	Height of the coils
h_m	5 mm	Height of the magnets
h_t	2 mm	Height of the teeth tips
g	1 mm	Airgap length
N	1	Number of windings
N_p	5	Number of pole-pairs facing the air gap
N_{ph}	3	Number of phases
N_s	15	Number of slots
N_{sp}	5	Number of slots per phase N_s/N_{ph}
R_{ag}	33.8 mm	Mean radius of the air gap
R_b	5 mm	Radius of the aluminium bar
R_i	34.3 mm	Inner radius of the stator
R_m	33.3 mm	Outer radius of the magnets
R_r	28.3 mm	Radius of the iron part of the rotor
R_s	66.6 mm	Outer radius of the stator
τ_m	32.3 mm	Magnet pitch
τ_p	32.3 mm	Pole pitch
τ_t	21.467 mm	Slot pitch
τ_{tt}	15.533 mm	Tooth width
τ_{tp}	19.1 mm	Width of the teeth tips
τ_w	3 mm	Width of the windings
τ_{wp}	64.6 mm	Winding pitch
τ_{ws}	1.1835 mm	Width of the current sheets

TABLE III
MATERIAL PROPERTIES

Property	Value	Description
B_{rem}	1.23 T	Remanent flux density of the magnets
μ_r	1.05	Relative recoil permeability of the magnets
μ_0	$4\pi \cdot 10^{-7}$ Tm/A	Permeability of free air

APPENDIX B

$$c_{1n} = \mathcal{B}_{\mathcal{I}0}(m_n R_i), \qquad c_{2n} = \mathcal{B}_{\mathcal{K}0}(m_n R_i),$$
$$c_{3n} = \mathcal{B}_{\mathcal{I}0}(m_n R_r), \qquad c_{4n} = \mathcal{B}_{\mathcal{K}0}(m_n R_r),$$
$$c_{5n} = \mathcal{B}_{\mathcal{I}0}(m_n R_m), \qquad c_{6n} = \mathcal{B}_{\mathcal{K}0}(m_n R_m),$$
$$c_{7n} = \mathcal{B}_{\mathcal{I}1}(m_n R_m), \qquad c_{8n} = \mathcal{B}_{\mathcal{K}1}(m_n R_m),$$

$$\mathcal{K}_{an}(m_n r) = \mu_0 M_n \int_{m_n R_r}^{m_n r} \frac{\mathcal{B}_{\mathcal{K}1}(x)dx}{\mathcal{B}_{\mathcal{I}1}(x)\mathcal{B}_{\mathcal{K}0}(x) + \mathcal{B}_{\mathcal{K}1}(x)\mathcal{B}_{\mathcal{I}0}(x)},$$
$$\mathcal{K}_{bn}(m_n r) = \mu_0 M_n \int_{m_n R_r}^{m_n r} \frac{\mathcal{B}_{\mathcal{I}1}(x)dx}{\mathcal{B}_{\mathcal{I}1}(x)\mathcal{B}_{\mathcal{K}0}(x) + \mathcal{B}_{\mathcal{K}1}(x)\mathcal{B}_{\mathcal{I}0}(x)},$$

$$a_{1n} = \frac{\left(\frac{c_{5n}}{c_{6n}} + \frac{c_{7n}}{c_{8n}}\right)\left(\frac{c_{3n}}{c_{4n}}\mathcal{K}_{an}(m_n R_m) + \mathcal{K}_{bn}(m_n R_m)\right)}{\left(\frac{c_{3n}}{c_{4n}} - \frac{c_{5n}}{c_{6n}}\right)\left(\frac{c_{1n}}{c_{2n}} + \frac{c_{7n}}{c_{8n}}\right) + \mu_r\left(\frac{c_{3n}}{c_{4n}} + \frac{c_{7n}}{c_{8n}}\right)\left(\frac{c_{5n}}{c_{6n}} - \frac{c_{1n}}{c_{2n}}\right)},$$

$$a_{2n} = \frac{\left(\frac{c_{5n}}{c_{6n}}\mathcal{K}_{an}(m_n R_m) + \mathcal{K}_{bn}(m_n R_m)\right) - \mu_r\left(\frac{c_{5n}}{c_{6n}} - \frac{c_{1n}}{c_{2n}}\right)a_{1n}}{\left(\frac{c_{3n}}{c_{4n}} - \frac{c_{5n}}{c_{6n}}\right)},$$

$$b_{1n} = \frac{c_{1n}}{c_{2n}}a_{1n},$$
$$b_{2n} = \frac{c_{3n}}{c_{4n}}a_{2n},$$
$$C_n = \frac{a_{1n}c_{3n} - b_{1n}c_{4n}}{c_{4n}c_{1n} - c_{2n}c_{3n}}\Big(\mathcal{B}_{\mathcal{I}0}(m_n R_{ag})\mathcal{B}_{\mathcal{K}1}(m_n R_{ag}) + \mathcal{B}_{\mathcal{I}1}(m_n R_{ag})\mathcal{B}_{\mathcal{K}0}(m_n R_{ag})\Big).$$

REFERENCES

[1] V. Ostovic, *Dynamics of saturated electric machines*. New York: Springer-Verlag, 1989.

[2] L. Encica, J. J. H. Paulides, E. Lomonova, and A. J. A. Vandenput, "Electromagnetic and thermal design of a linear actuator using output polynomial mapping," vol. 4, 2006, pp. 1919–1926.

[3] H. Polinder, J. G. Slootweg, M. J. Hoeijmakers, and J. C. Compter, "Modelling of a linear PM machine including magnetic saturation and end effects: maximum force to current ratio," *IEEE Transactions on Industry Applications*, vol. 39, no. 6, pp. 1858–1863, 2003.

[4] T. A. Driscoll and L. N. Trefethen, *Schwarz-Christoffel Mapping*. Cambridge: Cambridge University Press, 2002.

[5] J. Steinbrink, "Analytical determination of the cogging torque in brushless motors excited by permanent magnets," *International Conference on Electrical Machines and Drives*, pp. 172–177, 2-5/5/2007.

[6] T. C. O'Connell and P. T. Krein, "The Schwarz-Christoffel analytical method applied to electric machine slot shape optimization," Turkey, Antalia, 2-5/5/2007, pp. 341–346.

[7] M. Markovic, M. Jufer, and Y. Perriard, "Analyzing an electromechanical actuator by Schwarz-Christoffel mapping," *IEEE Transactions on Magnetics*, vol. 40, no. 4, pp. 1858–1863, July 2004.

[8] J. Wang, D. Howe, and G. Jewell, "Fringing in tubular permanent-magnet machines: Part II. cogging force and its minimization," *IEEE Transactions on Magnetics*, vol. 39, no. 6, pp. 3517–3522, November 2003.

[9] J. L. G. Janssen, J. J. H. Paulides, E. Lomonova, and A. J. A. Vandenput, "Cogging force reduction in tubular permanent magnet actuators," Turkey, Antalia, 2006, pp. 1–6.

[10] J. Wang, G. W. Jewell, and D. Howe, "A general framework for the analysis and design of tubular linear permanent magnet machines," *IEEE Transactions on Magnetics*, vol. 35, no. 3, pp. 1986–2000, May 1999.

[11] J. Wang, D. Howe, and G. W. Jewell, "Analysis and design optimization of an improved axially magnetized tubular permanent-magnet machine," *IEEE Transactions on Energy Conversion*, vol. 19, no. 2, pp. 289–295, June 2004.

[12] S. M. Jang, J. Y. Choi, S. H. Lee, S. K. Cho, and W. B. Jang, "Analysis of the tubular motor with halbach and radial magnet array," *International Conference on Electrical Machines and Systems*, vol. 1, pp. 250–252, 2003.

[13] Cedrat Co., *Flux 9.10 2D and 3D applications. New features*, Meylan, France, 2005.

[14] Z. Q. Zhu and D. Howe, "Instantaneous magnetic field distribution in brushless permanent magnet DC motors, part III: Effect of stator slotting," *IEEE Transactions on Magnetics*, vol. 29, no. 1, pp. 143–151, 1993.

[15] E. Furlani, *Permanent Magnet and Electromechanical devices*. USA: Academic Press, 2001.

[16] Y. Zhilichev, "Calculation of magnetic field of tubular permanent magnet assemblies in cylindrical bipolar coordinates," *IEEE Transactions on Magnetics*, vol. 43, no. 7, pp. 3189–3196, july, 2007.

Analytical and Numerical Techniques for Solving Laplace and Poisson Equations in a Tubular Permanent Magnet Actuator: Part II. Schwarz-Christoffel Mapping

B.L.J. Gysen *Student Member, IEEE*, E.A. Lomonova *Member, IEEE*, J.J.H. Paulides *Member, IEEE* and A.J.A. Vandenput *Senior Member, IEEE*
Electromechanics and Power Electronics Group
Department of Electrical Engineering
Eindhoven University of Technology
P.O. Box 513, 5600MB, Eindhoven, The Netherlands
Email: B.L.J.Gysen@student.tue.nl

***Abstract*—In Part I of the paper, a semi-analytical framework is derived for the magnetic field calculation in the air gap of a tubular permanent magnet (PM) actuator. The extension is made for skewed topologies. However, the slotting effect and its related cogging force cannot be determined in a straightforward way. Therefore, the Schwarz-Christoffel (SC) conformal mapping method will be applied to one pole-pair of the tubular PM actuator. This mapping allows for field calculation in a domain where standard field solutions can be used. In this way slotting effect can be taken into account, however skewing cannot be implemented directly. The SC-conformal mapping method is only valid for two-dimensional Cartesian domains. Therefore, a special transformation from the cylindrical to the Cartesian coordinate system is applied to describe the tubular actuator as a linear actuator.**

I. Introduction

Analytical descriptions of the magnetic field distribution and the related force and EMF waveforms have the advantage of giving physical insight into the design and optimisation problem of finding the optimal geometry for a given set of performance specifications. Although these methods are very elegant and fast, for a geometry with a slotted structure, the slotting effect is difficult to incorporate. This slotting effect and its related cogging force can be eliminated by means of control, [1], however, reducing this effect during the design offers the benefit of reducing the need for control, and thereby increasing the efficiency and stability of the actuator. In [2], it is shown that the cogging force due to the slotting effect can have an amplitude of 120 N, which can be relativly large depending on the application, and therefore it cannot be neglected during the design and optimisation process.

In order to model this effect, the Schwarz-Christoffel (SC) conformal mapping technique is used, [3]. This theory originates form the Riemann mapping theorem (1851) which states that any simply connected region in the complex domain can be mapped onto any other provided that neither is the entire plane. This method was widely described in the literature and mainly adressed to the rotary machines: synchronous and asynchronous ones, [4]–[8]. This paper explains an application of this method for a tubular PM actuator in order to calculate the related cogging force due to the slotting effect, as well as the total force (neglecting end effects). The tubular structure of the machine gives some complications since the SC-mapping technique only applies to two-dimensional Cartesian domains. A mapping based upon 'unrolling' and 'stretching' the tubular machine into a linear machine is used to tackle this problem. Furthermore, the modelling of coils and magnets in the mapping domain is considered and the results are verified with finite element (FE) software of FLUX [9] .

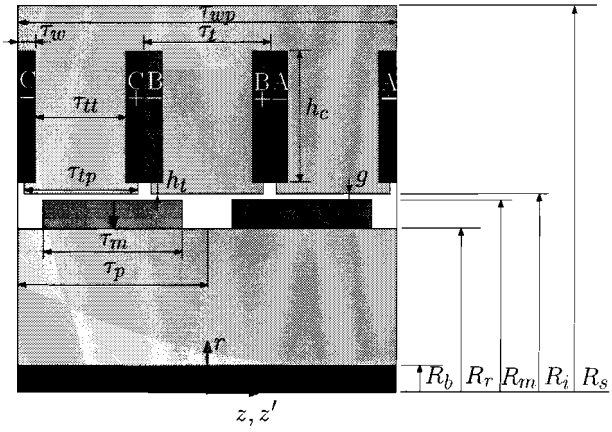

Fig. 1. Cross section of one pole-pair of the tubular PM actuator.

In Fig. 1 a cross section of one pole-pair of the tubular PM actuator is shown together with the relevant dimensions, where the values are given in Table I and the material properties in Table II of Appendix A. Note that in this case full pitch magnets are considered, $\tau_m = \tau_p$, but the technique also applies for other magnet to pole pitch ratios.

II. Schwarz-Christoffel conformal mapping

Conformal mapping is a mathematical transformation of one domain to another. It has the ability to map a complex structure, like a slotted stator, to a relative simple structure (circle, rectangle, bi-infinite strip, upper half plane, etc.) of which the field solutions are given in the literature. The original domain is called as the W-domain, where the actuator consists of vertices, $w_1, ..., w_n$, and interior angles, $a_1\pi, ..., a_n\pi$, in counterclockwise order. The mapping domain is called as the Z-domain with corresponding prevertices, $z_1, ..., z_n$. It is possible to consider the total actuator including end and slotting effects, however one pole-pair, see Fig. 2, has already 28 vertices. Taking into account that the total actuator consists of five pole-pairs, $N_p = 5$, this would result in a polygon of more than 140 points since the extra pole-pairs of the translator, which are situated outside the stator, have to be taken into account in order to model the end effects. The calculation of the mapping function and magnetic field distribution would therefore need a long computation time. However, the end effects can be considered seperately from the total force by firstly, considering only one pole-pair of the total actuator, hereby excluding the end effects, and secondly, considering only end effects by modelling the stator as a full iron block, which decreases the number of vertices drastically. In this paper only one pole-pair of the actuator is considered, but end effects can be modelled by following basically the same strategy.

Due to the physical nature of the electrical machines, the conversion of the electromagnetic energy takes place in the air gap. Thus, the identification of the magnetic field inside the air gap is one of the major steps within the design procedure of electrical machines. The polygon, P_w, should therefore represent the air gap. However, the polygon, P_w, must be closed and since the airgap region for one pole-pair is not a closed structure in a linear machine, periodical boundary conditions are applied, which are represented by two extra lines in the total polygon, (w_1, w_2) and (w_3, w_4), see Fig. 2. The mapping of this polygon onto a rectangle is applied, where it is ensured that the left and right sides of the rectangle correspond to the extra lines, (w_1, w_2) and (w_3, w_4), in the W-domain. Therefore, the same periodical boundary conditions can be applied in the Z-domain, hereby eliminating the need of an extra transformation to enforce periodical boundary conditions. Normally, the rectangle is mapped onto a circle to enforce periodical boundary conditions, [5].

The mapping function from a rectangle polygon, P_z, in the Z-domain to the actuator airgap polygon, P_w, in the W-domain is given by [3]

$$w = f(z) = A + C \int_z \prod_{k=1}^{n} (z - z_k)^{a_k - 1} dz. \qquad (1)$$

where A and C are a complex offset and scaling constant, respectively.

In Fig. 3 the mapping in the Z-domain is shown. Note that the four corners in the W-domain, $(w_1, ..., w_4)$, correspond to the four corners in the Z-domain, $(z_1, ..., z_4)$. This is necessary in order to have the same boundary conditions on each side of the rectangle in the Z-domain. So, the lines, (z_1, z_2) and (z_3, z_4), are periodic boundary conditions and the lines, (z_2, z_3) and (z_4, z_1), represent the boundary conditions at the iron.

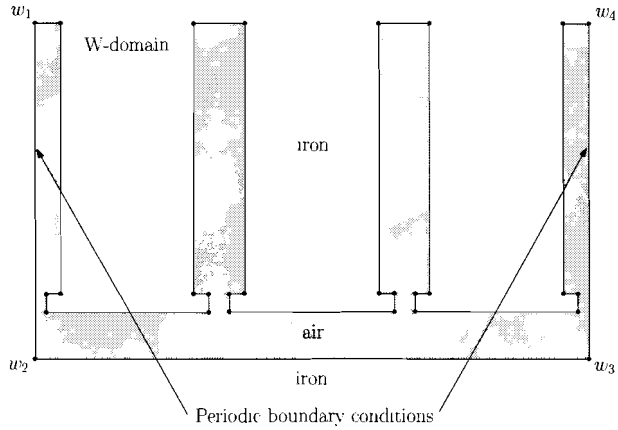

Fig. 2. Polygon P_w of the airgap region of one pole-pair of the tubular PM actuator.

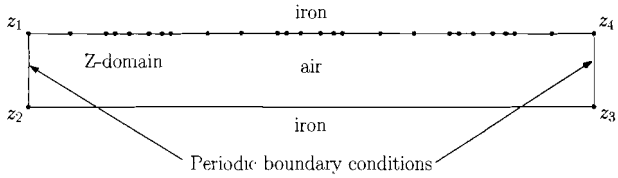

Fig. 3. Mapping of the polygon P_w to the rectangular Z-domain.

The goal is to calculate the field at the center radius of the air gap, $R_{ag} = \frac{R_m + R_i}{2}$, therefore it is necessary to know which points in the Z-domain correspond to the points of the center radius of the air gap in the W-domain. This is done by the inverse transformation, $z = f^{-1}(w)$, which is impossible to solve analytically for polygons which consist of more then four points, and therefore this inverse transformation is calculated numerically. Since this increases the computation time, these points have to be limited according to the application. Once the points in the Z-domain are determined, the field solution can be calculated at these points. The field solution obtained at the points, z_i, can then be plotted as function of the corresponding points in the W-domain, w_i, which is the desired solution. So the strategy can be summerised as:

- Define polygon P_w in the W-domain,
- Calculate mapping function $f(z)$,
- Define grid (z_i) in the Z-domain by $f^{-1}(w_i)$,
- Calculate field in the Z-domain at points z_i,
- Mapping of the field solution to the W-domain,
- Proceed with EMF and force calculation.

III. Application of SC-mapping

A. Coordinate system

The SC-mapping strategy is applied to one pole-pair of the tubular PM actuator. In order to use the SC-mapping method for field calculation in the Z-domain and transform it to the W-domain. Consider the magnetostatic Maxwell equations in

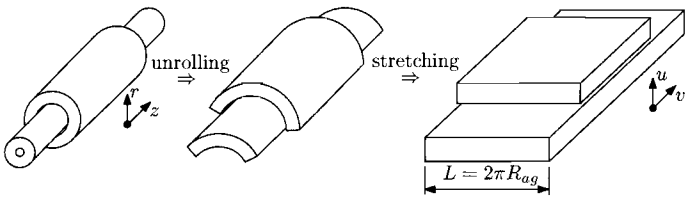

Fig. 4. Unrolling from (r, z) to (u, v).

terms of the magnetic vector potential, $\mathbf{A}$, given by the Poisson equation

$$\nabla^2 \mathbf{A} = -\mu_0(\mathbf{J} + \nabla \times \mathbf{M}), \tag{2}$$

where $-\mu_0(\mathbf{J} + \nabla \times \mathbf{M})$ is a source term depending on spatial parameters and/or time, with $\mathbf{J}$ the current density vector and $\mathbf{M}$ the magnetisation vector of the magnets. Note that, since it is a two-dimensional problem, also the scalar potential could be used. For a source-free region, the Poisson equation reduces to the Laplace equation $\nabla^2 \mathbf{A} = \mathbf{0}$. These equations should be the same in both domains. The Z-domain is always a two-dimensional Cartesian coordinate system, (x, y), but the W-domain is a two-dimensional axisymmetric cylindrical coordinate system, (r, z), which has a different form of Laplace equation. In both domains the magnetic field has only directions in (r, z) and (x, y), respectively, therefore, the magnetic vector potential, $\mathbf{A}$, has only a direction orthogonal to both directions of both domains, which is independent on the orthogonal direction. So, in summary

$$\mathbf{A}_{W-dom} = A(r, z)\mathbf{e}_\perp, \tag{3}$$

$$\mathbf{A}_{Z-dom} = A(x, y)\mathbf{e}_\perp, \tag{4}$$

where $\mathbf{e}_\perp$ is the unit vector in orthogonal direction of both domains, and evaluation of $\nabla^2 \mathbf{A}$ gives

$$\nabla^2 \mathbf{A}_{W-dom} = \frac{\partial^2 A}{\partial r^2} + \frac{1}{r}\frac{\partial A}{\partial r} - \frac{2}{r^2}A + \frac{\partial^2 A}{\partial z^2}, \tag{5}$$

$$\nabla^2 \mathbf{A}_{Z-dom} = \frac{\partial^2 A}{\partial x^2} + \frac{\partial^2 A}{\partial y^2}. \tag{6}$$

This means that a field solution in the Z-domain does not correspond to a field solution in the W-domain. Therefore, the geometry of the actuator is transferred from the axisymmetric cylindrical coordinate system, (r, z), to a Cartesian coordinate system, (u, v), by 'unrolling' and 'stretching' the tubular actuator, see Fig. 4. The mean area of the air gap is kept constant by taking the depth of the two-dimensional Cartesian model, L, equal to the circumference of the air gap, $2\pi R_{ag}$, and the geometry parameters in the direction of movement are also kept the same, $v = z$.

While unrolling the actuator from (r, z) to (u, v), the permeances in the r- and z-directions should be the same as the permeances in u- and v-directions in order to have the same electromechanical behaviour. This means that $\mathcal{P}_u = \mathcal{P}_r$ and $\mathcal{P}_v = \mathcal{P}_z$. However since v is already defined, there is only a freedom of changing u. Solving two independent equations with only one variable is impossible. Therefore, in general, it will be impossible to describe the tubular actuator as a linear actuator with the exactly the same behaviour. If a piece of material is considered in both the tubular and linear actuator,

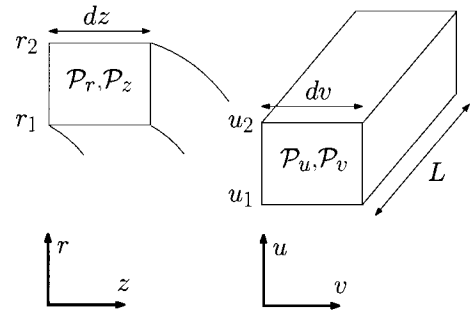

Fig. 5. The permeances in both coordinate systems.

as depicted in Fig. 5, then the permeances in r-, z-, u- and v-directions are given by

$$\mathcal{P}_r = \frac{\mu\pi(r_1 + r_2)dz}{r_2 - r_1}, \tag{7}$$

$$\mathcal{P}_z = \frac{\mu\pi(r_2^2 - r_1^2)}{dz}, \tag{8}$$

$$\mathcal{P}_u = \frac{\mu L dv}{u_2 - u_1}, \tag{9}$$

$$\mathcal{P}_v = \frac{\mu L(u_2 - u_1)}{dv}. \tag{10}$$

It can be observed that the axial permeances depend quadratically on r. Therefore, the transformation from the axisymmetric cylindrical coordinate system to the two-dimensional Cartesian coordinate system is performed by keeping the axial permeances equal, $\mathcal{P}_v = \mathcal{P}_z$. And since $dv = dz$, the final transformation of the coordinate system is given by

$$u = \frac{r^2}{2R_{ag}}, \tag{11}$$

$$v = z. \tag{12}$$

Note that this introduces an error for the radial permeances, however this error is zero in the middle of the air gap, which is the most important position since the force is evaluated on the magnetic field solution in the middle of the air gap.

B. Field calculation

For calculation of the mapping function, the MATLAB® SC Toolbox [10] is used, the current version was released in 2005. This toolbox allows for automatic calculation of the mapping function (1). The polygon, P_w, is defined as in Fig. 2, where the transformation (11)-(12) is applied. If the mapping function is calculated, the grid in the W-domain has to be defined according to the points where the magnetic field has to be calculated. The grid points in the W-domain, $w_i = v_i + ju_i$, are complex numbers where the real part corresponds to the v-direction and the imaginary part corresponds to the u-direction. If a uniform grid is considered, all these points undergo an inverse transformation which is very time-consuming, and it is useful to consider only points inside the polygon, P_w, and eliminate the other ones, since for these points the mapping function (1) does not hold, see Fig. 6.

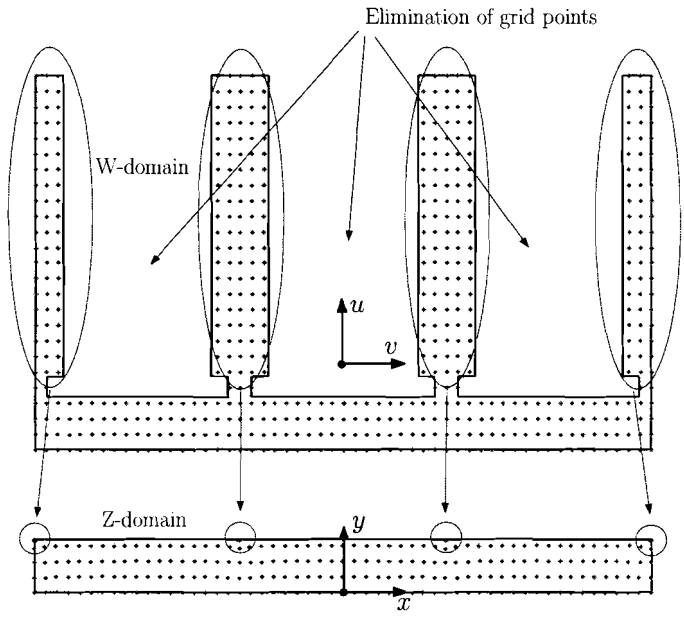

Fig. 6. Grid in the W-domain and Z-domain of one pole-pair of the tubular PM actuator.

These points are then transformed to the Z-domain by the inverse transformation $f^{-1}(w_i)$. The grid in the air gap and the magnets is relatively unchangable due to the SC-transformation, whereas the grid of the coils however, is almost mapped into a point as indicated in Figs. 6 and 8. This phenomenon is called crowding and it is best to avoid it because it influences the accuracy of the solution [11].

The coils are squares in the W-domain but in the Z-domain they are definitely not. In order to use standard field solutions in the Z-domain, the square coil is divided into a finite number of points, w_p, each with a current, $I_c = \frac{NI_{ph}}{N_c}$, where I_{ph} is the phase current, N is the number of windings and N_c is the number of point wires used for mapping the square coil. These point wires, z_p, are also mapped into the Z-domain, where the magnetic field is calculated for each of them. The same holds for the magnets and therefore, they are modelled as two current sheets at the side of the magnets. This equivalency is valid for rare-earth permanent magnets where μ_r is close to unity and when a homogeneous magnetisation is considered. These current sheets consist of a finite number, N_m, of points, which are also mapped to the Z-domain. The value of the current for one wire of the current sheet is defined as

$$I_m = \pm\frac{H_m h_m}{N_m}, \tag{13}$$

$$H_m = \frac{B_m}{\mu_r \mu_0}, \tag{14}$$

where B_{rem} is the remanence flux density, μ_r is the recoil permeability and h_m is the original height of the magnets in the cylindrical coordinate system. The working point of the magnet is approximately given by

$$B_m = \frac{B_{rem}}{1 + \frac{\mu_r g(R_r + R_m)}{2h_m R_{ag}}}. \tag{15}$$

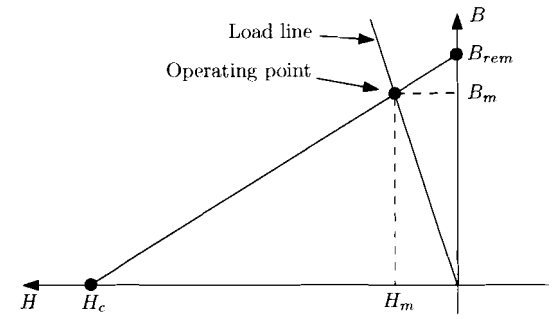

Fig. 7. Demagnetisation curve of the magnets and the load line.

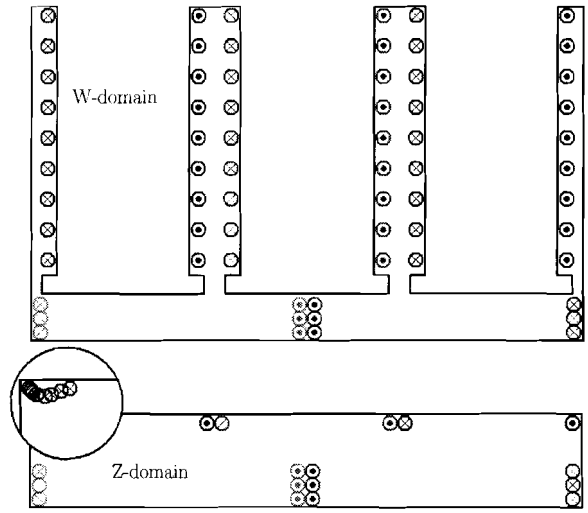

Fig. 8. Point wires in the W-domain and Z-domain of one pole-pair of the tubular PM actuator.

The total mapping of the wires is shown in Fig. 8. The next step is to calculate the field solution in the Z-domain for all these point wires. The flux density has directions in u and v, but due to the transformation the u-direction (or v-direction) in the W-domain does not correspond to the y-direction (or x-direction) in the Z-domain, and therefore if the flux density has to be mapped back to the W-domain, the gradient of the mapping function has to be taken into account

$$\mathbf{B}_{W-dom}(w) = \frac{\mathbf{B}_{Z-dom}(z)}{\nabla f(z)}. \tag{16}$$

Another option is to calculate the magnetic vector potential in the Z-domain, since it has only a component in the θ-direction, which is unchanged due to the transformation. The magnetic vector potential is then easily obtained in the W-domain and the magnetic field in the W-domain can then be calculated by

$$\mathbf{A}_{W-dom}(w) = \mathbf{A}_{Z-dom}(z), \tag{17}$$

$$\mathbf{B}_{W-dom}(w) = \nabla \times \mathbf{A}_{W-dom}(w). \tag{18}$$

However, since (18) requires more points, w_i, to be mapped in order to calculate the curl, it is more efficient to calculate $\mathbf{B}$ in the Z-domain and use (16) to calculate the magnetic field in the W-domain. The total magnetic field solution is obtained by

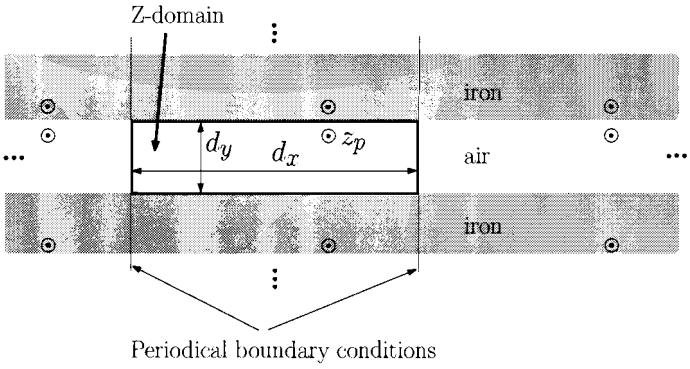

Fig. 9. Imaging and translation of a point wire in the Z-domain of one pole-pair of the tubular PM actuator.

superposition of the individual field solutions of every point wire.

Thus, consider the Z-domain with one-point wire. The top and bottom of the rectangle have an iron boundary, whereas the left and right ones have periodic boundary conditions. The magnetic field solution is obtained by applying the imaging method to the top and bottom boundaries, and translation to the left and right boundaries. Normally, the imaging method requires a summation over the imaged point wires, but an analytical description is given in [12]. The only summation left is for superposition of the magnetic field of the translated point wires in the x-direction, Fig. 9. In practice, only a finite number of translations is considered, N_t.

The magnetic field of a single point wire is given by [12]

$$\mathbf{B}_{Z-dom}(x,y) = B_x(x,y)\mathbf{e}_x + B_y(x,y)\mathbf{e}_y, \qquad (19)$$

with

$$B_x = \frac{I\mu_0}{4d_y}\sum_{k=-\infty}^{\infty}\left[\frac{\sin\left(\frac{\pi(y+y_p)}{d_y}\right)}{\cosh\left(\frac{\pi(x-x_p-kd_x)}{d_y}\right)-\cos\left(\frac{\pi(y+y_p)}{d_y}\right)} + \frac{\sin\left(\frac{\pi(y-y_p)}{d_y}\right)}{\cosh\left(\frac{\pi(x-x_p-kd_x)}{d_y}\right)-\cos\left(\frac{\pi(y-y_p)}{d_y}\right)}\right], \qquad (20)$$

$$B_y = \frac{I\mu_0}{4d_y}\sum_{k=-\infty}^{\infty}\left[\frac{\sinh\left(\frac{\pi(x-x_p-kd_x)}{d_y}\right)}{\cosh\left(\frac{\pi(x-x_p-kd_x)}{d_y}\right)-\cos\left(\frac{\pi(y+y_p)}{d_y}\right)} + \frac{\sin\left(\frac{\pi(x-x_p-kd_x)}{d_y}\right)}{\cosh\left(\frac{\pi(x-x_p-kd_x)}{d_y}\right)-\cos\left(\frac{\pi(y-y_p)}{d_y}\right)}\right], \qquad (21)$$

where $x_p = \mathrm{Re}(z_p)$, $y_p = \mathrm{Im}(z_p)$, d_x- and d_y- the dimensions of the rectangle of the Z-domain and I is the current of the point wire, I_c, in the case of the coils and I_m, in the case of the magnets.

Additionally the magnetic field in the W-domain is calculated by (16) and compared with a FEM calculation for a phase current of $I_{ph} = \frac{J_0}{NA_c}$, for $J_0 = 7.5$ A/mm^2, A_c the area of the coils in the cylindrical domain and the parameters given in Tables I, ?? and III , the solution is plotted in Fig. 10. Very good agreement of the field solution inside the air gap has been found within 2%. Note that the FE calculation is performed on the axisymmetric cylindrical model.

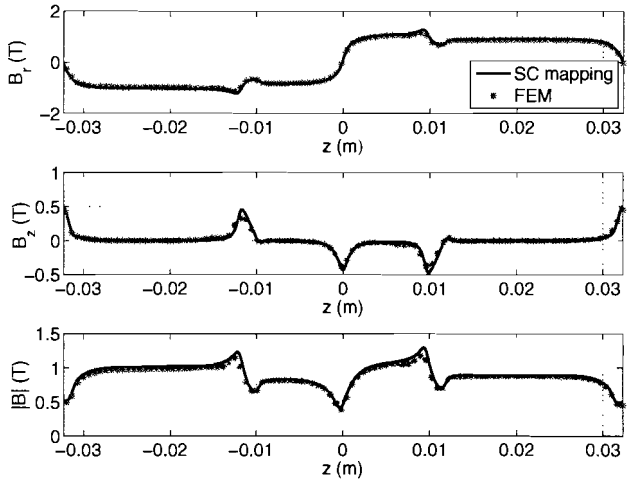

Fig. 10. Magnetic field in the air gap of one pole-pair of the tubular PM actuator.

C. EMF calculation

For the evaluation of the EMF waveform, the flux linkage of each phase must be calculated. The magnetic field is evaluated at the stator bore, R_i, instead of R_{ag} and the flux linkage is approximately the amount of radial flux at the tooth of the phase that is considered

$$\Psi = 2\pi R_i N \int_{-\frac{\tau_t}{2}+D}^{\frac{\tau_t}{2}+D} B_u(u,v)dv\Big|_{u=g(R_i),I_c=0}, \qquad (22)$$

where D is equal to $-\tau_t$, 0 or τ_t for phase A, B or C respectively. This is the flux linkage of one tooth per phase and it has to be multiplied by the number of teeth per phase, N_{sp}, for the total flux linkage per phase. The EMF is then calculated as

$$e = -\frac{\partial\Psi}{\partial t} = -\frac{\partial\Psi}{\partial\Delta_z}\frac{\partial\Delta_z}{\partial t} = -\frac{\partial\Psi}{\partial\Delta_z}v. \qquad (23)$$

These waveforms are calculated for a constant speed of $\frac{\partial\Delta_z}{\partial t} = 0.5$ m/s and shown in Fig. 11 together with the FE calculation, good agreement has been found. The EMF waveforms of the SC-mapping are slightly higher then the FE calculation due to the calculation of the fields at R_i which introduces a small error caused by the transformation from (r,z) to (u,v).

D. Force calculation

When the total field distribution in the air gap is known, the force acting on the translator can be calculated by means of the Maxwell Stress Tensor

$$F = \frac{N_p}{\mu_0}\oint_S \mathbb{T}.\mathbf{n}dS, \qquad (24)$$

where $\mathbf{n}$ is the normal vector on the surface S, N_p is the number of pole-pairs and the tensor is defined as

$$\mathbb{T} = \begin{bmatrix} B_r^2 - \frac{|B|^2}{2} & B_rB_\theta & B_rB_z \\ B_\theta B_r & B_\theta^2 - \frac{|B|^2}{2} & B_\theta B_z \\ B_zB_r & B_zB_\theta & B_z^2 - \frac{|B|^2}{2} \end{bmatrix}, \qquad (25)$$

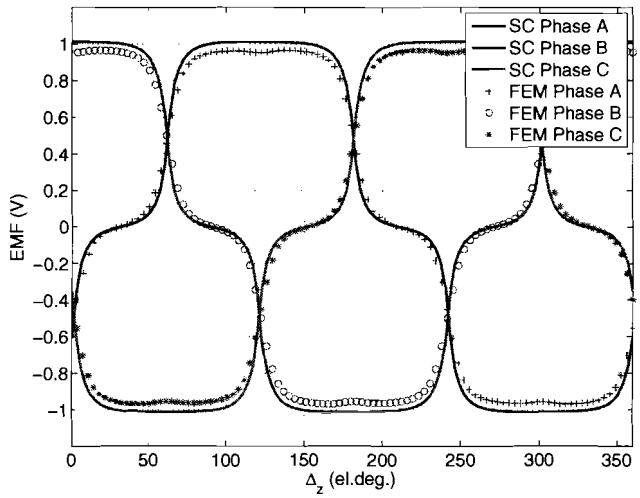

Fig. 11. EMF waveforms of the tubular PM actuator for a constant speed of 0.5 m/s.

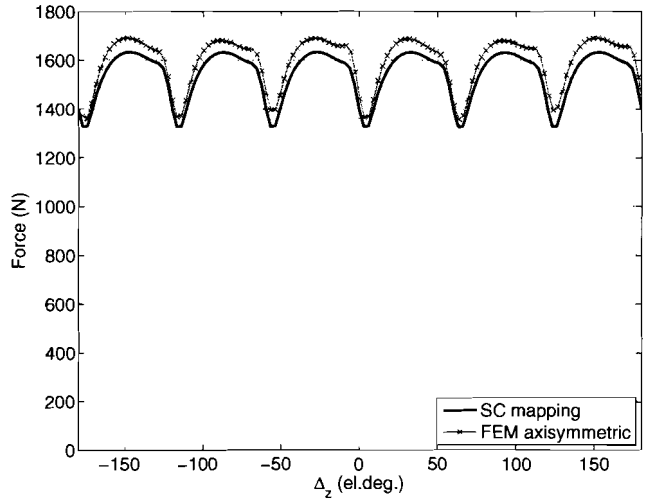

Fig. 12. Thrust force excluding end effects.

where B_r, B_θ and B_z is the total radial, angular and axial magnetic field at the surface S, respectively. In (24), S is the closed surface which consists of the airgap surface, S_1 : $u = g(R_{ag})$, the sides of the W-domain, $S_2 : v = -\tau_p$ and $S_3 : v = \tau_p$, and a surface in the back iron of the translator, $S_4 : u = g(R_b)$. If (24) is evaluated on S, only the surface of the air gap, S_1, is important because the sides of the w-plane, S_2 and S_3, have periodic boundary conditions which cancel each other since their normal vectors are in opposite direction, and the surface in the back iron of the magnets, S_4, has a high permeability which is negligible compared to the permeability of the air gap. This simplifies equation (24) to

$$F_v = \frac{N_p L}{\mu_0} \int_{-\tau_p}^{\tau_p} B_u\big(g(R_{ag}), v\big) B_v\big(g(R_{ag}), v\big) dv. \qquad (26)$$

When movement is involved, only the sheets of the magnets are moved in the v-direction. In this way the mapping function stays fixed during movement, no grid mapping and coil mapping have to be performed which take a lot of computation time. The verification with FEM is shown in Fig. 12 and acceptable agreement has been found within 5% accuracy. This total force does not include end effects, however cogging effect due to the slotted structure is identified. The slotting effect itself is also calculated and verified with FEM, shown in Fig. 13. In every case acceptable results within 5% accuracy are achieved. It is wise to mention that the force calculation by means of the Maxwell Stress Tensor is very sensitive to the density of the grid.

IV. Computation time

Another issue that has to be considered is the computation time. In this geometry, a transformation of a polygon of 28 points has to be mapped which takes about 33 seconds, which is quite long when optimisation is considered. But if the polygon is slightly changed, which will be the case during optimisation, the SC-mapping algorithm can use the previous simulated mapping in order to calculate the mapping of the

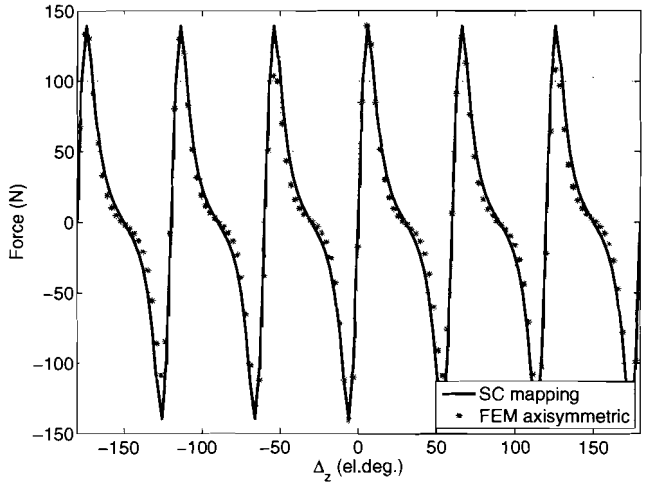

Fig. 13. Cogging effect due to slotting.

changed polygon, which results in a much faster mapping and is therefore still usefull for optimisation. The field and force calculations take less then a second, depending on the number of images and translations in the Z-domain and the resolution of the air gap. The coils consist of a finite number of wires which are mapped in the Z-domain. In Fig. 8 it can be observed that all these wires are almost mapped onto one point in the Z-domain. Thus, if knowledge about the field distribution close to the coils is not necessary (for example, for force calculation) the coils can be modelled by just a single wire which saves a number of field calculations and inverse mappings.

V. Conclusion

The SC-mapping technique for determination of the magnetic field in the air gap and thrust force for a tubular PM actuator is presented. A transformation has to be used in order to apply the SC-mapping technique for a tubular PM actuator. The advantage of this technique is that the slotting

effect can be taken into account and results are generated in a relatively fast way. However, for a tubular actuator, a special transformation has to be applied in order to describe the geometry in a Cartesian coordinate system. The various steps have been described in order to apply the SC-mapping for evaluation of the magnetic field, EMF and force waveforms. Accurate results up to 3.5% have been achieved with a relatively short computational time.

In Part I of the paper, the semi-analytical framework is presented for calculation of the force waveform, neglecting end and slotting effects. In this paper, the slotting effect is identified with the SC-mapping technique. Both tools are implemented in a MATLAB environment which gives the ability to combine both solutions, in order to calculate the total force in a relatively fast way, neglecting end effects. However these end effects can be calculated with the semi-analytical framework, [13], or with the SC-mapping technique using the same strategy as described in this paper. Combining the three solutions gives the total force with the inclusion of all the force ripples. In fact, it is also possible to use only the SC-mapping method, but keep in mind that the mapping from the cylindrical to the Cartesian domain introduces an error, which can become significant for geometries with larger airgap lengths. If the end effects could be described by one of both models, then the total force profile of the tubular PM actuator could be determined in a relatively fast way. A combination of both models can therefore be used as a framework for optimisation technique in order to find the optimal geometry for maximising the mean force and minimising the total force ripple of the tubular PM actuator.

APPENDIX

TABLE I
DIMENSIONS AND PARAMETERS OF THE TUBULAR ACTUATOR

Dimension	Value	Description
h_{bi}	7.8 mm	Height of the back iron
h_c	22.5 mm	Height of the coils
h_m	5 mm	Height of the magnets
h_t	2 mm	Height of the teeth tips
g	1 mm	Airgap length
N	1	Number of windings
N_p	5	Number of pole-pairs facing the air gap
N_{ph}	3	Number of phases
N_s	15	Number of slots
N_{sp}	5	Number of slots per phase N_s/N_{ph}
R_{ag}	33.8 mm	Mean radius of the air gap
R_b	5 mm	Radius of the aluminium bar
R_i	34.3 mm	Inner radius of the stator
R_m	33.3 mm	Outer radius of the magnets
R_r	28.3 mm	Radius of the iron part of the rotor
R_s	66.6 mm	Outer radius of the stator
τ_m	32.3 mm	Magnet pitch
τ_p	32.3 mm	Pole pitch
τ_t	21.467 mm	Slot pitch
τ_{tt}	15.533 mm	Tooth width
τ_{tp}	19.1 mm	Width of the teeth tips
τ_w	3 mm	Width of the windings
τ_{wp}	64.6 mm	Winding pitch
τ_{ws}	1.1835 mm	Width of the current sheets

TABLE II
MATERIAL PROPERTIES

Property	Value	Description
B_{rem}	1.23 T	Remanent flux density of the magnets
μ_r	1.05	Relative recoil permeability of the magnets
μ_0	$4\pi \cdot 10^{-7}$ Tm/A	Permeability of free air

TABLE III
SIMULATION PARAMETERS.

Variable	Value	Description
N_c	5	Number of point wires per coil
N_m	20	Number of point wires per current sheet of the magnets
N_t	5	Number of translations

ACKNOWLEDGEMENT

The authors would like to thank Dr. A. van Deursen for the background information about conformal mapping and the related numerical implementation issues.

REFERENCES

[1] J. W. Jansen, E. A. Lomonova, A. J. A. Vandenput, J. C. Compter, and A. H. Verweij, "Improvement of the dynamic performance of an AC linear permanent magnet machine," Madison, New Jersey, U.S.A., 2003.

[2] J. L. G. Janssen, J. J. H. Paulides, E. A. Lomonova, and A. J. A. Vandenput, "Cogging force reduction in tubular permanent magnet actuators," Turkey, Antalia, 2006, pp. 1–6.

[3] T. A. Driscoll and L. N. Trefethen, *Schwarz-Christoffel Mapping*. Cambridge: Cambridge University Press, 2002.

[4] J. Steinbrink, "Analytical determination of the cogging torque in brushless motors excited by permanent magnets," *International Conference on Electrical Machines and Drives*, pp. 172–177, 2-5/5/2007.

[5] T. C. O'Connell and P. T. Krein, "A preliminary investigation of computer-aided Schwarz-Christoffel transformation for electric machine design and analysis," Troy, NY, 2006, pp. 166–172.

[6] ——, "The Schwarz-Christoffel analytical method applied to electric machine slot shape optimization," Turkey, Antalia, 2-5/5/2007, pp. 341–346.

[7] M. Markovic, M. Jufer, and Y. Perriard, "Reducing the cogging torque in brushless DC motors by using conformal mappings," *IEEE Transactions on Magnetics*, vol. 40, no. 2, pp. 1858–1863, May 2004.

[8] ——, "Analyzing an electromechanical actuator by Schwarz-Christoffel mapping," *IEEE Transactions on Magnetics*, vol. 40, no. 4, pp. 1858–1863, July 2004.

[9] Cedrat Co., *Flux 9.10 2D and 3D applications. New features*, Meylan, France, 2005.

[10] T. Driscoll, "Schwarz-Christoffel toolbox user's guide: Version 2.3," 2005.

[11] T. K. Dellilo, "The accuracy of numerical conformal mapping methods: A survey of examples and results," *Society for Industrial and Applied mathemathics*, vol. 31, no. 3, pp. 788–812, 1994.

[12] B. Hague, *The principles of electromagnetism applied to electrical machines*. New York: Dover Publications Inc., 1962.

[13] J. Wang, D. Howe, and G. Jewell, "Fringing in tubular permanent-magnet machines: Part II. cogging force and its minimization," *IEEE Transactions on Magnetics*, vol. 39, no. 6, pp. 3517–3522, November 2003.

High Temperature Permanent Magnet Actuator for Fail-Safe Applications

Bart GYSEN†, Sarah GIBSON‡, Richard CLARK‡ and Geraint JEWELL‡
† Department of Electromechanics and Power Electronics, Eindhoven University of Technology, Netherlands
‡Department of Electronic and Electrical Engineering, University of Sheffield, UK
Tel: +44(0)114 222 5195– Fax: +44(0)114 2225196 – e-mail: sarah.gibson@sheffield.ac.uk

Topic: 10

Abstract

The paper describes the design and experimental validation of a high temperature, parallel-polarised permanent magnet electromagnetic actuator developed for fail-safe applications. The actuator is designed to operate in an ambient temperature of 230 °C, has a stroke of 2 mm and minimum force requirement, which can be maintained with zero current, of 1kN for the entire stroke. To minimise the mass of the final design thermal modelling has been used to determine the acceptable current rating for the device, features were added to the pole faces to linearise the force characteristic, and high temperature grades of materials were used. A prototype actuator has been constructed and experimentally validated at the rated operating temperature of 230°C.

1. Introduction

There is a trend in many areas such as aerospace, gas turbines, and processing plants to replace mechanical linkages and hydraulic systems by direct electrical actuation. This change results in requirements for electromagnetic actuation in harsher environments specifically in terms of high temperature [1].

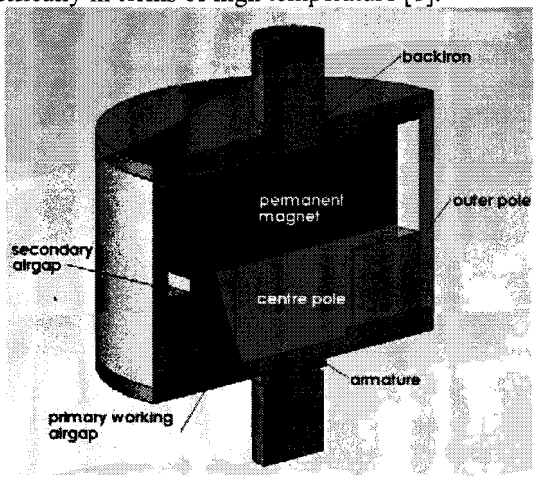

Figure 1: Sectioned schematic of a parallel-polarised permanent magnet latching actuator.

This paper describes the design and experimental testing of a parallel-polarised permanent magnet latching actuator suitable for high temperature applications. A particular feature of this actuator, which is shown in Fig. 1, is its inherent fail-safe behaviour, since the armature retracts to the closed position in the absence of stator current without the requirement for a return spring. The permanent magnet produces a bias flux in the magnetic circuit through the primary working (variable) airgap thus provides an attractive force on the armature see Fig. 2. This bias flux can be modulated by flux due to the stator coil mmf, to either aid or oppose the permanent magnet flux in the working airgap and hence increasing or reducing the force respectively as shown in Fig. 3 [2]. An advantage of this design is that the force modulation does not involve passing demagnetising flux through the magnet (although a small amount may pass through due to leakage) as the coil flux takes a "parallel path" through the secondary airgap as shown in Fig. 2. This makes the device relatively immune to irreversible demagnetisation which is especially important at high temperature and for fail-safe applications. The specific actuator described in this paper was designed to operate in an ambient temperature of 230°C and to produce a permanent closing force in the absence of stator current of at least 1kN at an armature displacement, and hence airgap, of up to 2 mm. The degree to which this force can be modulated is predominantly limited by the thermal constraints of the materials used; this design specification requires a modulation of ± 500 N in order to control the position of the armature against a given load.

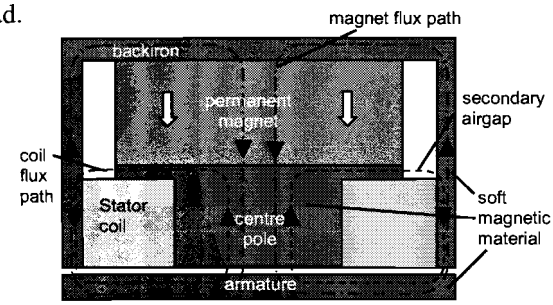

Figure 2: Parallel-polarised, permanent magnet latching actuator with schematic representations of the coil and magnet flux paths.

A major objective in the design process was to minimize the size and weight of the device. This was done through the selection of high performance materials, thermal analysis and design features incorporated into the pole faces to linearise the force characteristic allowing high force capability at large airgaps. Operation in high temperature environments inevitably incurs a mass penalty as the remanence and coercivity of the permanent magnet, the saturation flux density of the stator core and armature and the conductivity of the stator all decrease with increasing temperature, albeit at very different rates with the decrease in coil conductivity having the most pronounced effect on actuator size. Even ambient

temperatures of 230 °C can produce quite a challenging environment for such high force devices.

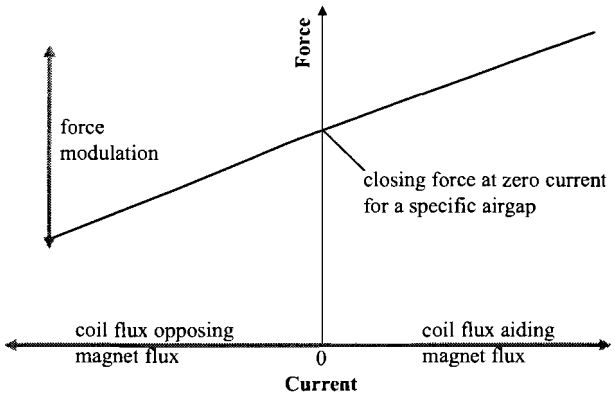

Figure 3: Generalised force versus current characteristics for an actuator of the type shown in Fig. 2.

To minimise the actuator mass for a given force and stroke specification, static and transient thermal analysis were performed to predict the maximum sustainable coil current density. As the particular specification considered involves generating forces at comparatively larger airgaps, a design feature reported in [3] which shapes the pole faces has been incorporated with due modification.

2. Actuator Design and Construction

For operation in an ambient environment of 230 °C with allowance for self-heating, internal temperatures within the coil are likely to exceed 300°C, and hence the limits of conventional polymeric insulation systems. The use of high temperature wires and high temperature grades of permanent magnets is therefore essential. The coil of this device was formed using Fujithermo A wire which has a copper core conductor with nickel plating and a convertible ceramic insulation coating. The wire is manufactured with a polymeric layer to protect the wire during coil forming. The wire has a continuous temperature rating of 400 °C for over 20,000 hours operation before the breakdown voltage becomes reduced by 50 % [4]. The formed coil was then over-wound with a mica tape and potted using a ceramic potting compound. The packing factor (the ratio of copper conductor area to actual winding area) for this type of coil was 43% which is competitive with standard wound coils. The net thermal conductivity of the coil was measured experimentally in a custom test-rig which is based on a standard uni-axial heat flow method [5].

High temperature grades of permanent magnets and soft magnetic materials were used in this device (samarium cobalt Sm_2Co_{17} and VACOFLUX 50 49% cobalt iron respectively) [6]. The permanent magnet material used had a remanence of 1.07 T (0.97 T at 230°C), and coercivity of 800 kA/m. Many soft magnetic materials can be used at 400°C, which is the operating limit of the high temperature wires used, with very limited reduction in magnetic properties. For this design a 49% cobalt iron material (which has a Curie temperature of 950°C) was used, as it has a high value of saturation flux density of 2.35 T, which means the device is smaller and lighter than if more conventional materials were used.

In order to exploit the high temperature properties of the materials used while ensuring that their temperature limits were not exceeded an ANSYS axisymmetric finite element thermal model was employed. This model assumed, natural heat convection and radiation in ideal black body surroundings with the device mounted vertically in air. Analytical equations were used to estimate the values of convection heat transfer coefficient from the surfaces of the actuator as a function of temperature [7] and a relative surface emissivity of 0.2 was assumed [8]. The current and resulting copper loss in the coil were varied iteratively until the limiting temperature was reached in either the magnet or the coil. The model determined the maximum current density in the coil at a 2 mm airgap to be 5 A/mm^2 for steady state operation see Fig. 4. Although the temperature in the device was highest in the coil at 359°C it is the lower operating temperature of the magnet at 350°C which limited the current density level for this design. For transient operations and taking into account the fixtures for a specific application the current density could be greater than this value. To enable operation at higher current densities, future designs might involve filling the secondary airgap, and voids between the magnet side and outer pole with a non-magnetic material of similar thermal expansion but high thermal conductivity.

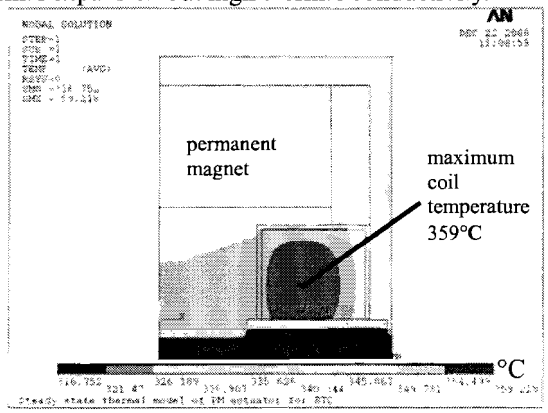

Figure 4: Half a cross-section of the axi-symmetric actuator with a plot of predicted temperature in °C.

Fig. 5 shows the leading design parameters of the actuator, which are defined in Table 1. To prevent shock loads from collisions between the centre pole and the armature being transmitted through the centre pole and damaging the brittle permanent magnetic material the centre pole is reduced in height by a small amount, (named impact clearance in Table 1). The outer dimensions of the actuator were fixed by the space envelope available. The other dimensions were calculated by analysis of dimensional trade-offs to meet the requirements of modulation and closing force. For example, the centre pole and outer pole inner diameters (constrained to achieve equal pole areas) are selected to accommodate a given coil area without significantly increasing the coil slot height, which influences the available height to accommodate the permanent magnet.

To reduce the size of the device (which should produce at least 1kN of closing force at 2 mm or less) slots were added to the pole faces of the stator and a corresponding inverse protrusion to the armature surface. These features

act to reduce the circuit reluctance at large airgaps and produce regions of localised higher flux density in the airgap than would be seen on a flat pole face device as shown in Fig.6, and hence, increase the force within a specific airgap range. Fig. 7 shows the open-circuit axial force produced on the armature against airgap; for a range of slot heights. These values were predicted by finite element analysis, the force being calculated using the virtual work method. From these results it can be seen that a 2 mm high slot significantly improves the force at 2 mm and hence achieves the specification; however the penalty in terms of force can be seen at smaller gaps.

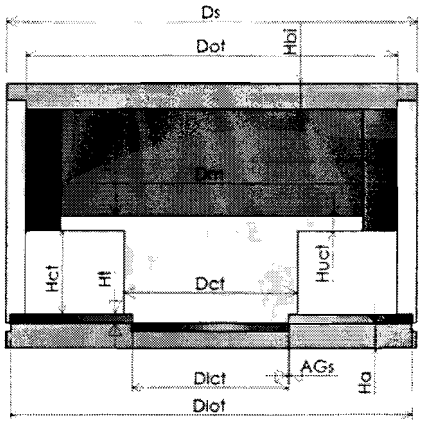

Figure 5: Cross section of the actuator showing leading design parameters

Table 1: Leading design parameters and dimensions of the final actuator design

Name	Description	Dimension
Ds	Diameter of the stator	95 mm
Dm	Diameter of the magnet	70 mm
Dct	Diameter of the centre pole	40 mm
Dlct	Diameter of the lower part of the centre pole	36 mm
Dot	Diameter of the outer pole	86 mm
Dlot	Diameter of the lower part of the outer pole	93 mm
Hbi	Height of the back iron	6 mm
Hm	Height of the magnet	25 mm
Huct	Height of the upper part of the centre pole	3.5 mm
Hct	Height of the centre pole	19.4 mm
Ht	Height of the extended protrusions/slots	2 mm
Ha	Height of the armature	6 mm
AGs	Radial airgap/clearance	0.1 mm
Intake	Impact clearance	0.1 mm
	Mass of actuator	2.84 kg

Figure 6: Open-circuit flux density at an airgap of 2 mm and with material properties for 230 °C

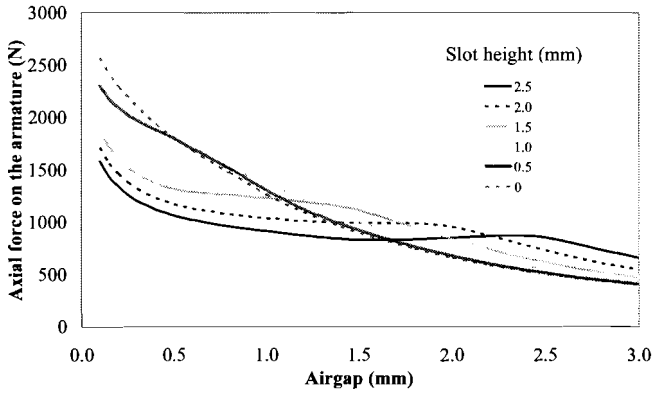

Figure 7: Predicted force against airgap for open-circuit and different pole face slot heights at 230°C.

3. High Temperature Testing

A prototype actuator, the dimensions of which are given in table 1, has been manufactured. Figs. 8 and 9 show an Instron loading frame test facility and the associated oven (maximum rating of 350°C) which was used to measure the static force-displacement-current characteristics of the actuator. The actuator was initially tested at room temperature then heat-soaked at 230°C until a steady state temperature in all the components was achieved it was then re-tested.

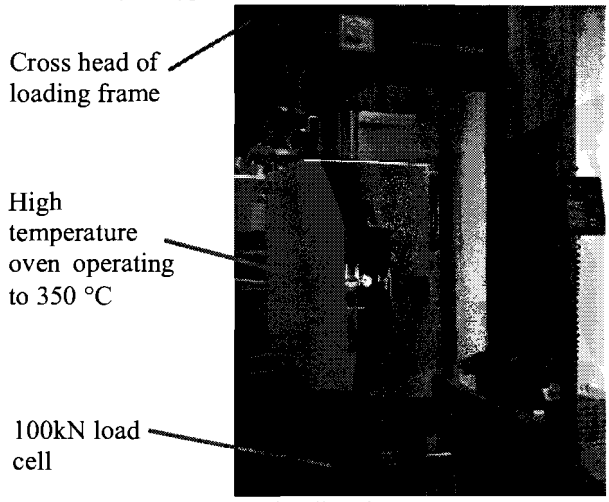

Figure 8: Instron loading frame and oven

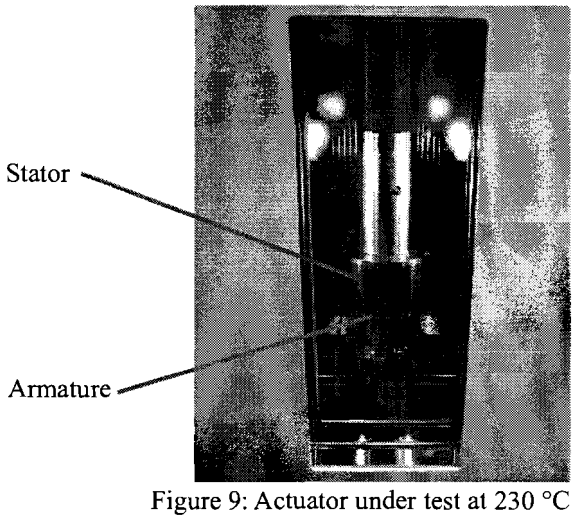

Figure 9: Actuator under test at 230 °C

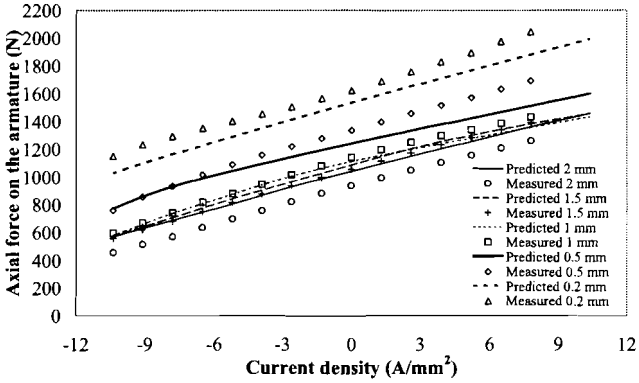

Figure 10: Measured and predicted force against current density for a range of airgaps at an ambient temperature of 24 °C.

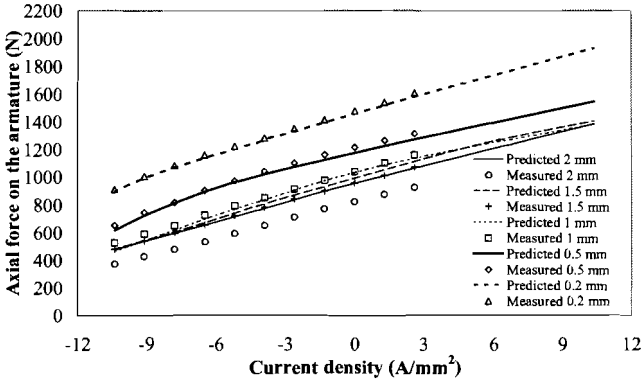

Figure 11: Measured and predicted force against current density for a range of airgaps at an ambient temperature of 230 °C.

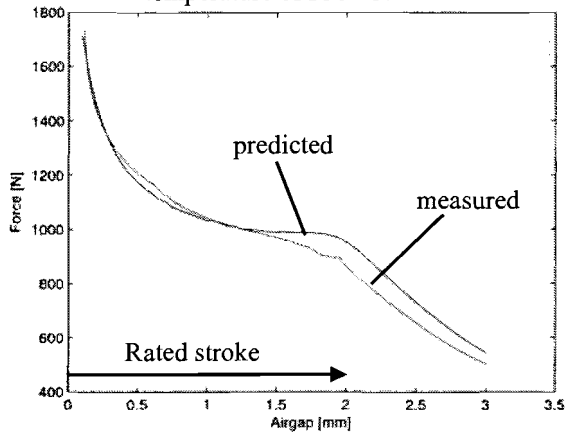

Figure 12: Open-circuit measured and predicted force against airgap at an ambient temperature of 230 °C

The measured force characteristics at room temperature and 230 °C for a range of airgaps and currents are plotted in Figs. 10 and 11 with the characteristics predicted using finite element analysis. The results have a close agreement in terms of the general trend with airgap, modulation of the force with current and to the actual values measured.

There are some discrepancies, which may be attributed to friction caused by interference/contact of the pole protrusions on their corresponding slot. The clearance of 0.1mm may have been insufficient given the difficulty of maintaining concentricity of all the parts within the prototype and thermal expansion of the materials.

The measured force shown in Fig. 12 does not meet the specification of 1kN at the 2 mm airgap; however there is good agreement between measured and predicted characteristics at smaller airgaps.

4. Conclusions

This paper has provided a description of a permanent magnet latching actuator capable of producing 1kN at a 2mm airgap in ambient conditions of 230 °C within a relatively compact volume/low mass. The actuator has been constructed from materials suitable for operation at elevated temperature and has been validated at the operational temperature.

Acknowledgement

The authors would like to thank Vacuumschmelze GmbH for providing and heat treating the cobalt iron material.

References

[1] N. Sidell, and G.W. Jewell, *"The design and construction of a high temperature linear electromagnetic actuator"*, Journal of applied Physics, pp 4901-4903, 85(8), 1999.

[2] J. Rens, R. E. Clark, and G. W. Jewell, *"Static performance of a polarized permanent-magnet reluctance actuator for internal combustion engine valve actuation"*, IEEE Transactions on Magnetics, pp 2063-2070, 42(38), 2006.

[3] R. E. Clark, G. W. Jewell, S. J. Forrest, and J. Rens, *"Design features for enhancing the performance of electromagnetic valve actuation systems"*, IEEE Transactions on Magnetics, pp. 1163-1168, 41(3), 2005.

[4] J. Senoo, T. Usuki, Y. Yamada, S. Amano, and T. Tsuboi, *"Ceramic insulated wire"*, Fujuri technical review, (20), pp. 58-65, 1991.

[5] D.J., Powell, *"Modeling of high power density electrical machines for aerospace"*, thesis University of Sheffield, 2003.

[6] *"Soft magnetic materials and semi-finished products"*, Catalogue, Vacuumschmelze GMBH & Co. KG, edition 2002.

[7] J.P., Holman, *Heat Transfer 7th ed.* New York, McGrawHill, pp 321-331, 2002.

[8] N, Sidell, and G.W., Jewell, *"Short-stroke, bidirectional linear actuator for high temperature applications"*, IEE Proceedings Electrical Power Applications, pp 175-180, Vol. 147(3), 2000.